Thermal Transport in Porous Media with Application to Fuel Cell Diffusion Media and Metal Foams

by

Ehsan Sadeghi
B.Sc., Sharif University of Technology, Iran, 2003
M.Sc., Sharif University of Technology, Iran, 2006

A Dissertation Submitted in Partial Fulfillment of the
Requirements for the Degree of

DOCTOR OF PHILOSOPHY

in the Department of Mechanical Engineering

Thermal Transport in Porous Media with Application to Fuel Cell Diffusion Media and Metal Foams

by

Ehsan Sadeghi
B.Sc., Sharif University of Technology, Iran, 2003
M.Sc., Sharif University of Technology, Iran, 2006

Supervisory Committee

Dr. Nedjib Djilali, Co-Supervisor
(Dept. of Mechanical Engineering, University of Victoria)

Dr. Majid Bahrami, Co-Supervisor
(Dept. of Mechanical Engineering, University of Victoria)

Dr. David Sinton, Departmental Member
(Dept. of Mechanical Engineering, University of Victoria)

Dr. Boualem Khouider, Outside Member
(Dept. of Mathematics and Statistics, University of Victoria)

Supervisory Committee

Dr. Nedjib Djilali, Co-Supervisor
(Dept. of Mechanical Engineering, University of Victoria)

Dr. Majid Bahrami, Co-Supervisor
(Dept. of Mechanical Engineering, University of Victoria)

Dr. David Sinton, Departmental Member
(Dept. of Mechanical Engineering, University of Victoria)

Dr. Boualem Khouider, Outside Member
(Dept. of Mathematics and Statistics, University of Victoria)

ABSTRACT

Transport phenomena in high porosity open-cell fibrous structures have been the focus of many recent industrial and academic investigations. Unique features of these structures such as relatively low cost, ultra-low density, high surface area to volume ratio, and the ability to mix the passing fluid make them excellent candidates for a variety of thermofluid applications including fuel cells, compact heat exchangers and cooling of microelectronics. This thesis contributes to improved understanding of thermal transport phenomena in fuel cell gas diffusion layers (GDLs) and metal foams and describes new experimental techniques and analytic models to characterize and predict effective transport properties.

Heat transfer through the GDL is a key process in the design and operation of a proton exchange membrane (PEM) fuel cell. The analysis of this process requires determination of the effective thermal conductivity as well as the thermal contact resistance (TCR) associated with the interface between the GDL and adjacent surfaces/layers. The effective thermal conductivity significantly differs in through-plane and in-plane directions due to anisotropy of the GDL micro-structure. Also, the high porosity of GDLs makes the contribution of TCR against the heat flow through the medium more pronounced.

A test bed was designed and built to measure the thermal contact resistance and effective thermal conductivity in both through-plane and in-plane directions under vacuum and ambient conditions. The developed experimental program allows the separation of effective thermal conductivity and thermal contact resistance. For GDLs, measurements are performed under a wide range of compressive loads using Toray carbon paper samples. To study the effect of cyclic compression, which may happen during the operation of a fuel cell stack, measurements are performed on the thermal and structural properties of GDL at different loading-unloading cycles.

The static compression measurements are complemented by a compact analytical model that achieves good agreement with experimental data. The outcomes of the cyclic compression measurements show a significant hysteresis in the loading and unloading cycle data for total thermal resistance, TCR, effective thermal conductivity, thickness, and porosity. It is found that after 5 loading/unloading cycles, the geometrical, mechanical, and thermal parameters reach a“steady-state”condition and remain unchanged. A key finding of this study is that the TCR is the dominant component of the GDL total thermal resistance with a significant hysteresis resulting in up to a 34 % difference between the loading and unloading cycle data. Neglecting this phenomenon may result in significant errors in evaluating heat transfer rates and temperature distributions.

In-plane thermal experiments were performed using Toray carbon paper samples with different polytetrafluoroethylene (PTFE) content at the mean temperature of $65-70^{\circ}C$. The measurements are complemented by a compact analytical model that achieves good agreement with experimental data. Results show that the in-plane effective thermal conductivity remains approximately constant, $k \approx 17.5W/mK$, over a wide range of PTFE content, and it is approximately 12 times higher than the through-plane conductivity.

Using the test bed designed for the through-plane thermal conductivity measurement, the effective thermal conductivity and thermal contact resistance of ERG Duocel aluminum foam samples were measured under varying compressive loads for a variety of porosities and pore densities. Also, an experimental program associated with an image analysis technique is developed to find the size and distribution of contact spots at different compressive loads. Results show that the porosity and the effective thermal conductivity remain unchanged with the variation of pressure in the range of 0 to 2 MPa; but TCR decreases significantly with pressure due to an increase in contact area. Moreover, the ratio of contact area to cross-sectional area is 0-0.013, depending upon the compressive force, porosity, and pore density.

This study clarifies the impact of compression on the thermal and structural properties of GDLs and metal foams and provides new insights on the importance of TCR which is a critical interfacial transport phenomenon.

Contents

List of Tables

List of Figures

Nomenclature

f = weighting factor, Eq. (2.1)
k = thermal conductivity, W/mK
k_{eff} = effective thermal conductivity, W/mK
k_{Series} = effective thermal conductivity based on the Series model, W/mK
$k_{Parallel}$ = effective thermal conductivity based on the Parallel model, W/mK
n = coefficient $(3/\psi)$
Q = heat transfer rate, W
R_{sp} = thermal spreading resistance, K/W
R_m = medium thermal resistance, K/W
T = temperature, K

Greek

α = average angle between fibers and heat flow direction, °
β = shape factor, Eq. (2.4)
γ = geometrical function, Eq. (2.6)
ε = porosity, $[-]$
λ = fluid-to-solid thermal conductivity ratio (k_f/k_s), $[-]$
ϕ = volume fraction, $[-]$
ψ = sphericity, $[-]$

Subscripts

f = fluid
m = medium (matrix)
p = dispersed (particulate) phase
s = solid

Acronyms

EMT = effective medium theory
GDL = gas diffusion layer
HC = Hamilton and Crosser
MPL = micro porous layer
PEM = proton exchange membrane

PPI = pores per inch
$PTFE$ = polytetrafluoroethylene
RVC = reticulated vitreous carbon
TCR = thermal contact resistance
TPS = transient plane source

ACKNOWLEDGEMENTS

I would like to thank my supervisors, Dr. Ned Djilali and Dr. Majid Bahrami, for their incredible support and guidance throughout all aspects of my research. It was an excellent privilege for me to work with them and learn from their great knowledge and experience.

I would like to thank the members of the Institute for Integrated Energy Systems (IESVic) at the University of Victoria, and Multiscale Thermofluidics Lab at Simon Fraser University. I appreciate having had the opportunity to work with such a wide range of talented students, staff and researchers. In particular, I would like to specially thank Dr. Erik Kjeang for his helpful comments and Ali Tamayol, Kelsey Wong, Scott Hsieh, Mohsen Akbari, Abhishek Nanjundappa, and Peyman Taheri.

I am very thankful for the financial support of Natural Sciences and Engineering Research Council (NSERC) of Canada, the Canada Research Chairs Program, and the University of Victoria.

I would also like to thank my family in Iran, specially my mother who always believes in me, for being an unending source of encouragement and inspiration throughout my academic adventures. Finally, loving thanks go to my wife, Razieh Nikzad, for her continuous and lovely support, her endless encouragement, and her kindly patience.

Chapter 1

Introduction

The term “porous medium”describes any material consisting of a solid matrix with interconnected voids [1, 2]. The interconnectedness of the voids (the pores) allows the flow of one or more fluids through the material. In natural porous media such as limestone, rye bread, wood, or the human lung, the distribution of pores with respect to shape and size is irregular. Conversely, in man-made porous media, the microstructure can be organized (e.g., cellular metal lattice and fabrics) or random (e.g., carbon papers and metal foams) depending upon the manufacturing process.

Transport phenomena in porous media have been the focus of many industrial and academic investigations. The majority of the studies reported in the literature deal with low porosity media such as granular materials and packed beds. Recently, high porosity open-cell media such as open-cell metal foams and fibrous media have started to receive more attention. Interest in these media stems from their relatively low cost, ultra-low density, high surface area to volume ratio, and most importantly, their ability to mix the passing fluid. This makes them excellent candidates for a variety of unique thermofluid applications and devices [3, 4]. Three such applications are: 1) microelectronics and aerospace, which require high heat removal rates and light-weight solutions, 2) fuel cells, which need to have the capability for simultaneous heat exchange and electrochemical reactions, and 3) compact heat exchangers, which have large capacities at low temperature differentials [4, 5, 6, 7].

The microstructure of high porosity open-cell materials often consists of small ligaments forming a network of inter-connected dodecahedral-like cells such as metal foams as shown in Fig. 1.1 (a). Alternatively, the microstructure can be formed by small ligaments which lay on each other in a random open-cell structure such as fibrous gas diffusion layers (GDLs) as shown in Fig. 1.1 (b). The shape and size of these open cells vary throughout the medium which makes the structure random and anisotropic. Two of the parameters that describe such media are: 1) the porosity (the ratio of the void volume to the total volume) or relative density (the ratio of the density of the material to that of the solid phase) and 2) the pore diameter or pore density (number of pores per unit length) which is typically expressed in the unit of pores per inch (PPI), mostly used for metal foams. These structures can be constructed from a wide variety of materials including metals (aluminum, nickel, copper, iron, and steel alloys), polymers, and carbon. More importantly from a practical application viewpoint, these microstructures can be tailored to meet a wide range of requirements.

Accurate knowledge of the temperature distribution and associated heat transfer mechanisms is required to determine the various transport phenomena such as water and species transport, reaction kinetics, the rate of phase change in fuel cells [8, 7] and the heat transfer performance in metal foam heat exchangers [5]. To solve the energy equation for a porous medium and find the temperature distribution, it is important to know the thermal conductivity of the medium. Large differences in the thermal conductivities of the solid and fluid phases (2-3 orders of magnitude) as well as the high porosity of the medium make it necessary to define an effective thermal conductivity.

In all applications, there is at least one interface between the porous medium and a solid or porous surface. This gives rise to a phenomenon called thermal contact resistance (TCR). The actual area of contact, the total area of all microcontacts, is a small fraction of the nominal contact area [9, 10]. When heat flows in/out of a body through this small area, the heat flux lines are correspondingly constricted/spread apart and the resulting thermal resistance is referred to as constriction/spreading resistance. The constriction/spreading resistance R_{sp} is defined as the difference between the temperature of a heat source/microcontact and the temperature of a heat sink far from it divided by the total heat flow rate through the contact area Q ($R_{sp} = \Delta T/Q$) [11]. The contact resistance is a combination of spreading and constriction resistances and the resistance of the gas which fills the gap between the two contacting bodies, if applicable.

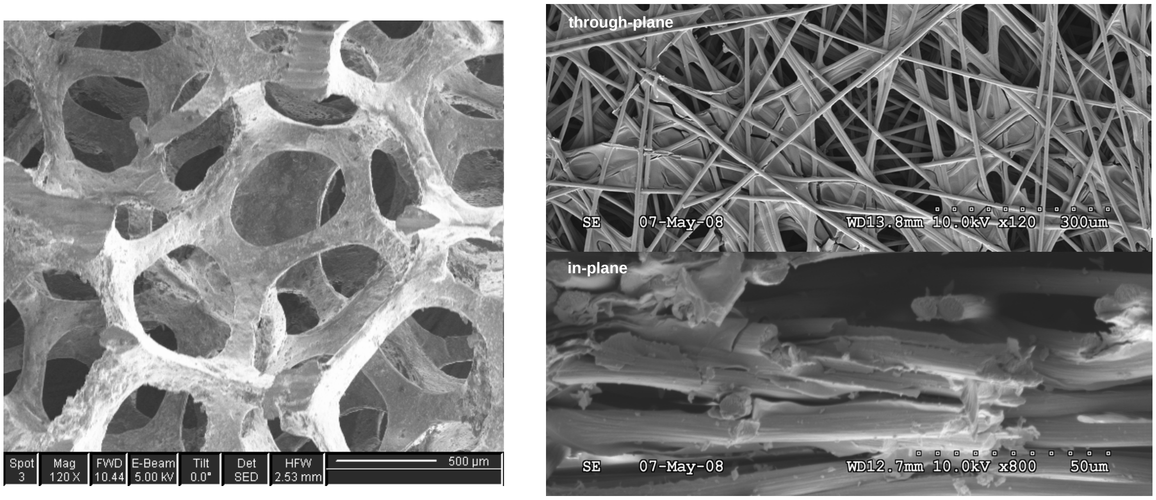

(a) (b)

Figure 1.1: SEM image of (a) ERG Duocel Al foam X 120; (b) Toray carbon paper: through-plane X 120 (top), in-plane X 800 (bottom)

1.1 Goals & Motivation

The geometric complexity and the random orientation of solid ligaments in high porosity materials prevent the development of an exact solution for the transport equations inside the media [3]. Also, these features complicate the estimation of TCR between these materials and other solid surfaces. Predicting transport phenomena in high porosity media plays a key role in the optimization of water and thermal management for a variety of industrial applications such as GDLs in fuel cells and metal foam-based heat exchangers. Evaluating the effective thermal conductivity and TCR for high porosity materials provides a good understanding about the thermal behavior of the medium and the thermal behavior at its interface with solid surfaces.

A review of the literature indicates that in the majority of previous studies, the TCR was bundled up with the effective thermal conductivity and characterized using an aggregate value. One fundamental issue with combining the two is that the TCR is an interfacial phenomenon, whereas the thermal conductivity is a transport coefficient characterizing the bulk medium. The thermal conductivity and TCR should therefore be distinguished. Also, the effect of orientation of ligament/matrix on the thermal conductivity and TCR should be clarified. Furthermore, the effects of compression on the thermal, geometrical and mechanical characteristics of porous media has not been thoroughly investigated.

The motivation for this study is to present a comprehensive investigation for both thermal conductivity and thermal contact resistance and to shed light on these two phenomena. The focus of the present study is on fibrous diffusion media (gas diffusion layers) and metal foams with the capability to study similar fibrous, cellular, and foam structures with minor modifications. A systematic approach is taken to develop analytical models and experimental techniques for determining the effective thermal conductivity and TCR. This approach accounts for the effects of temperature variation and cyclic compression on the microstructural and thermal properties of GDLs. Also, for the first time, a novel method is presented to find the in-plane thermal conductivity of GDLs.

The outcomes of this dissertation can be used to find the optimal operational condition and modify the design of fuel cell systems. It also can improve metal foam and fuel cell models that require specification of the effective thermal conductivity, TCR, thickness, and porosity. A schematic of the scope of the present study is shown in Fig. 1.2.

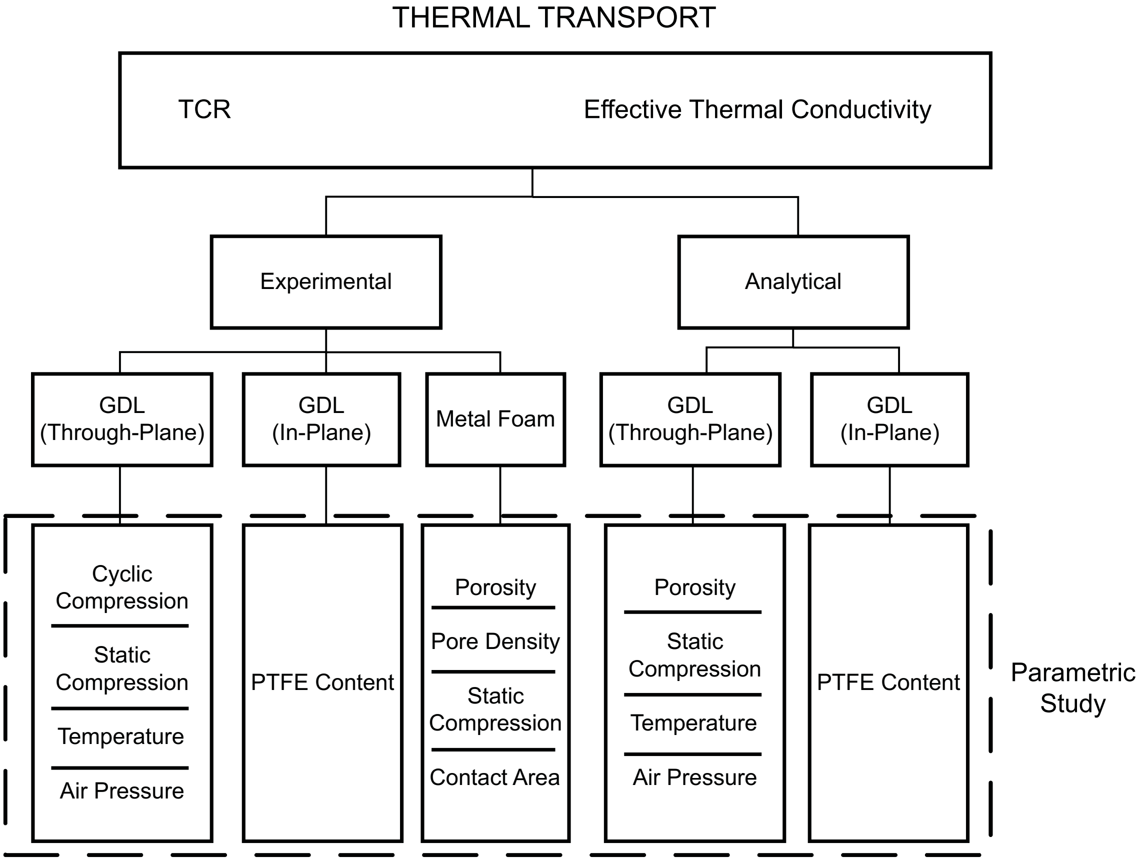

Figure 1.2: Scope of the present study

1.2 Organization

This thesis is organized into four chapters and ten appendices. The background and motivation are presented in Chapter 1. In Chapter 2, a critical review of previous studies on this topic is presented. The literature review covers different approaches that have been used to model the thermal conductivity, contact resistance, and compression in metal foams and gas diffusion layers of PEM fuel cells. Chapter 3 provides a summary of the main contributions of this thesis. These contributions are described in Appendix B-G in more detail. Each of these appendices includes a complete scientific journal publication. These six peer reviewed journal papers are either published or under review. A summary of the assumptions considered in these papers are presented in Appendix A. The conclusions and future avenues of research are presented in Chapter 4. Finally, the contribution of radiation heat transfer, uncertainty analysis, and the experimental data obtained in this study are presented in Appendix H, I, and J, respectively.

Chapter 2

Literature Review

Transport phenomena in high porosity open-cell materials have been the focus of many studies because of their unique thermal and hydraulic features. Several theoretical approaches have been taken to study transport phenomena in these materials which can be classified as: 1) asymptotic solutions (bounds), 2) the unit cell approach, and 3) random microstructure approaches.

Many effective thermal conductivity models found in the literature are based on one or a combination of five basic structural models: the Series, Parallel, Maxwell-Eucken (two forms) [12, 13] and Effective Medium Theory (EMT) models [14, 15]. These models provide asymptotic solutions for a porous medium.

The Series and Parallel models assume fluid and solid phases perpendicular or parallel to the heat flow direction and provide the lowest and highest bounds for the effective thermal conductivity of a porous medium, respectively[16].

Solving Laplace's equation for non-contacting spherical particles (discontinuous phase) in a medium, the Maxwell-Eucken relationship was developed for the effective conductivity of the medium (mixture) [12, 13]. When the dispersed phase contains solid material, the thermal conductivity obtained from the Maxwell-Eucken relation is relatively low and close to the value of the Series model; therefore, the relation is called the lower Maxwell-Eucken model. For a medium with a continuous solid phase, the thermal conductivity based on the Maxwell-Eucken relation is relatively high and close to the Parallel model; therefore, the relation is called the upper Maxwell-Eucken model [13].

The EMT model [14, 15] uses a similar approach to the Maxwell-Eucken models to establish a relationship for the effective thermal conductivity of the medium; however, it assumes a completely random distribution of each phase. Table 2.1 provides the equations for each of these models along with a schematic of their assumed structures.

Parallel model	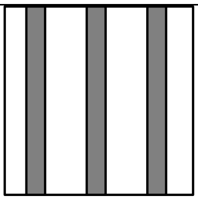	$k_{eff} = \phi_m k_m + \phi_p k_p$
Series model		$k_{eff} = \dfrac{k_m k_p}{\phi_p k_m + \phi_m k_p}$
Maxwell-Eucken models [12, 13]	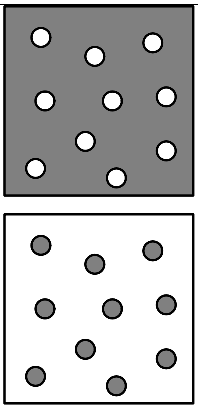	$k_{eff} = k_m \dfrac{(1 + 2\phi_p)\, k_p + 2\phi_m k_m}{\phi_m k_p + (2 + \phi_p)\, k_m}$
EMT model [14, 15]	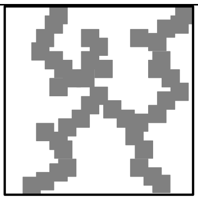	$\phi_m \left(\dfrac{k_m - k_{eff}}{k_m + 2k_{eff}} \right) + \phi_p \left(\dfrac{k_p - k_{eff}}{k_p + 2k_{eff}} \right) = 0$

Table 2.1: Fundamental effective thermal conductivity structural models for porous materials (heat flow in vertical direction)

By combining these five structural models, several new models have been developed [17, 18, 19]. For instance, Krischer [17] proposed a weighted harmonic mean of the Series and Parallel models for the effective thermal conductivity of heterogeneous materials:

$$k_{eff} = \frac{1}{f/k_{Series} + (1-f)/k_{Parallel}}. \tag{2.1}$$

Hamilton and Crosser [20] extended the Maxwell-Eucken models to include nonspherical particles and developed an empirically-based model:

$$k_{eff,\ HC} = k_m \frac{\left[1 + (n-1)\phi_p\right] k_p + (n-1)\phi_m k_m}{\phi_m k_p + \left[(n-1) + \phi_p\right] k_m}, \tag{2.2}$$

where ϕ_p and ϕ_m are the volume fractions of the dispersed (particulate) phase and the medium (matrix), respectively. In this model, n is equal to $3/\psi$ where ψ is the sphericity, defined as the ratio of the surface area of a sphere, with a volume equal to that of the particle, to the surface area of the particle. The parameter n is 3 and 6 for spherical and cylindrical particles, respectively [20].

To examine and assess the aforementioned thermal conductivity models, the predicted conductivities are plotted in Fig. 2.1 and compared to experimental data for GDLs and metal foams. It can be seen that all these fundamental models provide a wide boundary for the effective thermal conductivity. Even though the Krischer model [17] provides a rough estimate for the thermal conductivity, it is sensitive to the weighting parameter f which must be set for each material and porosity range. Among these models, the upper Maxwell-Eucken model shows the most agreement with the metal foam data.

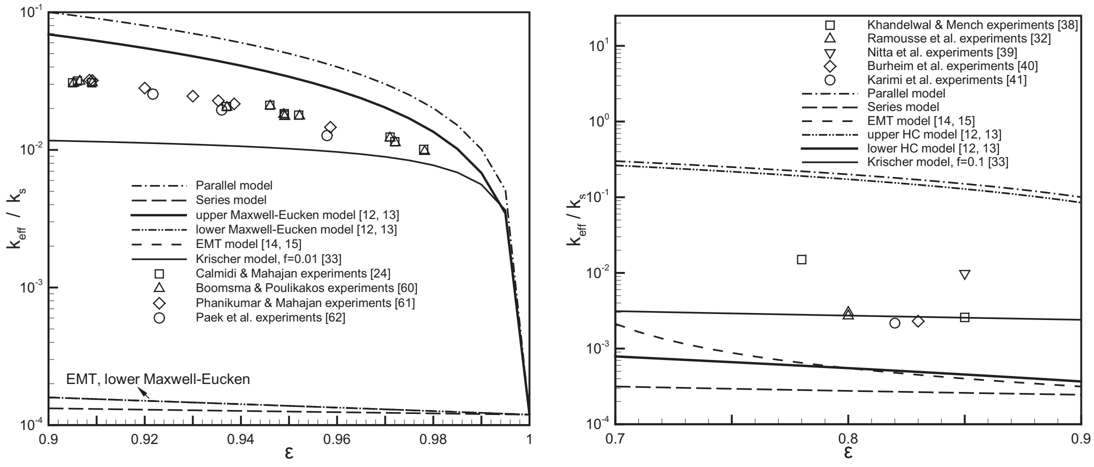

(a)

(b)

Figure 2.1: Experimental thermal conductivity of porous materials compared with the proposed asymptotic solutions; (a) aluminum foam-air ($k_s = 218W/mK$), (b) GDL-air ($k_s = 120W/mK$)

Several studies have focused specifically on thermal transport in metal foams or fibrous media such as GDLs. These studies are reviewed in the two next sections separately.

2.1 Metal Foams

A literature review shows that the thermal contact resistance has not yet been studied for a metal foam surface in contact with or brazed to another solid surface. A review of the studies available on the thermal conductivity of metal foams is presented.

2.1.1 Effective Thermal Conductivity

Generally, a “unit cell”has been taken to represent the metal foam microstructure [4, 5, 21, 22, 23, 24], and it is assumed that this unit cell can be repeated throughout the medium by virtue of periodicity. The unit cell approach breaks the problem into distinct conduction paths in solid and fluid phases; and calculates the conductivity of the medium as a series/parallel combination of the individual resistances for those paths. Applying the energy equation to the suggested unit cell, the effective thermal conductivity can be found analytically or numerically depending on the complexity of the unit cell.

Various two and three dimensional unit cell geometries can be found for metal foams in the literature. The geometry of unit cells, main assumptions, and features of the studies are summarized in Tables 2.2, 2.3.

A group of studies considered a specific geometry and distribution of pores and/or particles, and/or used the analogy between thermal, electrical, and mass transport phenomena. Using the analogy between mass diffusion and heat conduction, Hsu et al. [25] found the following relation for the effective thermal conductivity of sponge-like porous media:

$$\frac{k_{eff}}{k_f} = \left[1 - \sqrt{1-\varepsilon}\right] + \frac{1-\sqrt{\varepsilon}}{\lambda} + \left[\sqrt{\varepsilon} + \sqrt{1-\varepsilon} - 1\right]\left(\frac{\beta(1-\lambda)}{(1-\lambda\beta)^2}\ln\frac{1}{\lambda\beta} - \frac{\beta - 1}{1-\lambda\beta}\right), \tag{2.3}$$

where λ is the fluid-to-solid conductivity ratio and β is a shape factor which is a complex function of the porosity. This shape factor was approximated by:

$$\beta = \left(\frac{1-\varepsilon}{\varepsilon}\right)^{0.9676}. \tag{2.4}$$

Russell [26] developed one of the early model systems using the analogy between thermal and electrical transport. Assuming that the discrete phase is isolated cubes of the same size dispersed in the matrix material, he derived an equation for the

Researcher	Unit Cell	Notes
Calmidi and Mahajan [24]	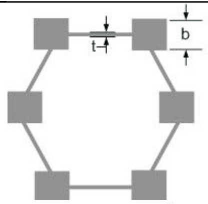	o Compact 2-D analytical model o Unrealistic microstructure (t / b = 0.09) o Tuning parameter (t/b) found through fitting experimental data
Bhattacharya et al. [5]	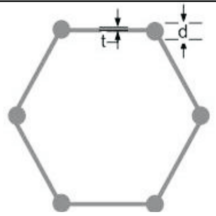	o More realistic than Calmidi and Mahajan's, t / d = 0.19, but more complicated o Tuning parameter (t/d) found through fitting experimental data
Du Plessis and Fourie [22]	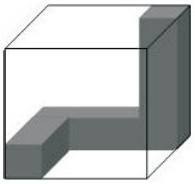	o Simple model o Significant deviations from experimental data
Dul'nev [23]	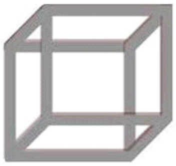	o Compact model o Unrealistic microstructure o Relatively good agreement with experimental data
Boomsma and Poulikakos [60]	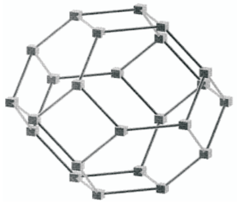	o Terakaidecahedron geometry with cubic nodes at the intersections of ligaments o Relatively compact analytical model with a tuning parameter (cubic size) found through fitting experimental data o Unrealistic microstructure when $\varepsilon < 0.9$
Schmierer and Razani [21]	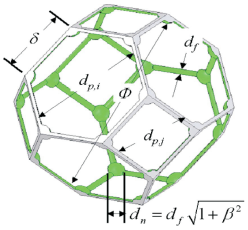	o Terakaidecahedron geometry with spherical nodes at the intersections of ligaments o Realistic microstructure o Image and geometrical analyses of the microstructure to find node size, $1 < \beta < 2$ o Numerical finite element analysis to calculate the effective thermal conductivity
Ozmat et al. [4]	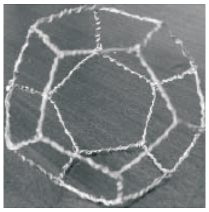	o Dodecahedron geometry having 12 pentagon-shaped facets with triangular cross-section ligaments o Compact analytical model based on the geometrical features of the basic cell and analogy between electrical and thermal conductivities o No lumped materials at the intersections of ligaments o Close agreement with experimental data for low thermal conductivity ratios

Table 2.2: A summary of unit cell approaches on metal foams

Researcher	Unit Cell	Notes
Krishnan et al. [63]	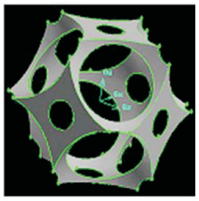	- Body-Centered-Cubic (BCC) structure satisfying minimum surface energies - Numerical model to determine the effective thermal conductivity - In agreement with experimental data only when the porosity is greater than 0.94 because of geometry limitations
Krishnan et al. [63]	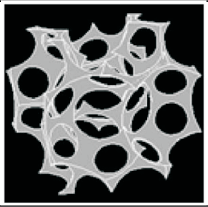	- A15 structure satisfying minimum surface energies - Numerical model to determine the effective thermal conductivity - In agreement with experimental data for a wide range of porosities

Table 2.3: A summary of unit cell approaches on metal foams (continuation of Table 2.2)

thermal conductivity of composite materials, using a series parallel network which can be written for a porous material as:

$$k_{eff} = k_s \frac{\varepsilon^{2/3} + (k_s/k_f)(1-\varepsilon^{2/3})}{\varepsilon^{2/3} - \varepsilon + (k_s/k_f)(1+\varepsilon-\varepsilon^{2/3})}, \tag{2.5}$$

where ε is the porosity of the medium,and k_s and k_f are the thermal conductivity of solid and fluid phases, respectively.

Ozmat et al. [4] found an analytical relationship for the effective thermal conductivity of metal foams which is useful for low conductivity ratios ($\lambda = k_f/k_s \to 0$):

$$k_{eff} = \gamma k_s(1-\varepsilon), \tag{2.6}$$

where γ is a function of geometrical properties of the structure including the lengths of the sides, the specific surface area, the ligament diameter, and the number of edges. Similar relationships were established by Lemlich. The geometrical parameter γ is 0.346 and 0.333 for the Ozmat and Lemlich models, respectively.

Ashby [27] proposed a model for cellular structures by adding two terms to the Lemlich model. This model considers conduction in both the solid and gas phases and is suitable for a medium with a small solid to fluid thermal conductivity ratio (e.g., RVC foam-water):

$$k_{eff} = \frac{1}{3}\left[(1-\varepsilon) + 2(1-\varepsilon)^{3/2}\right] k_s + \varepsilon k_f. \tag{2.7}$$

Wang and Pan [28] used a statistical method to generate a random combination of ligaments representing the metal foam microstructure. Applying a modified Lattice Boltzmann model, they found the effective thermal conductivity numerically for different ligament distributions and porosities.

Generally, an experimental apparatus known as a guarded-hot-plate has been employed to measure the thermal conductivity of open-cell metal foams. In this method, the sample is placed between two columns with known thermal properties. The other sides of these columns are in contact with a hot and a cold plate to provide a steady-state heat flux through the sample. There is another method called the transient plane source (TPS) method which is used to measure the effective thermal conductivity of composite materials [29, 30]. The basic principle of this method relies on a plane element which acts both as a temperature sensor and heat source. The TPS element is located between two samples with similar characteristics where both sensor faces are in contact with the two sample surfaces. The temperature is recorded with respect to time and position when the surrounding temperature suddenly changes. In this method, the information about the heat capacity of the investigated material is required. Solrzano et al. [31] used the TPS method to measure the thermal conductivity of closed-cell AlSi7 foams. They measured the thermal conductivity in different directions and at different positions and concluded that the TPS method is a powerful tool to measure the thermal conductivity of materials which have high in-homogeneities and density gradients. Existing experimental studies on open-cell metal foams are summarized in Table 2.4.

2.1.2 Critical Comparison of Existing Models with Experimental Data

The models discussed earlier are compared with existing literature experimental data for different foams in Fig. 2.2. The following observations can be made:

- The shape of the ligament cross-section is affected by the porosity variations and changes from circular shape ($0.85 < \varepsilon < 0.9$) to triangular and concave triangular shapes ($\varepsilon > 0.94$) [5, 21]. The effect of the variation of the ligament cross-section as well as the pore density have not been included in existing models.

- The Du Plessis and Fourie model [22] highly overestimates the effective thermal conductivity.

- The Dul'nev model [23] in spite of its simplicity provides an acceptable estimation of metal foams in higher porosities.

- The Ozmat model [4] can provide a good estimation of a foam structure when the thermal conductivity ratio is very small (foam-air and foam-vacuum); for higher thermal conductivity ratios, this model underestimates the conductivity, because it does not include heat conduction in the fluid phase.

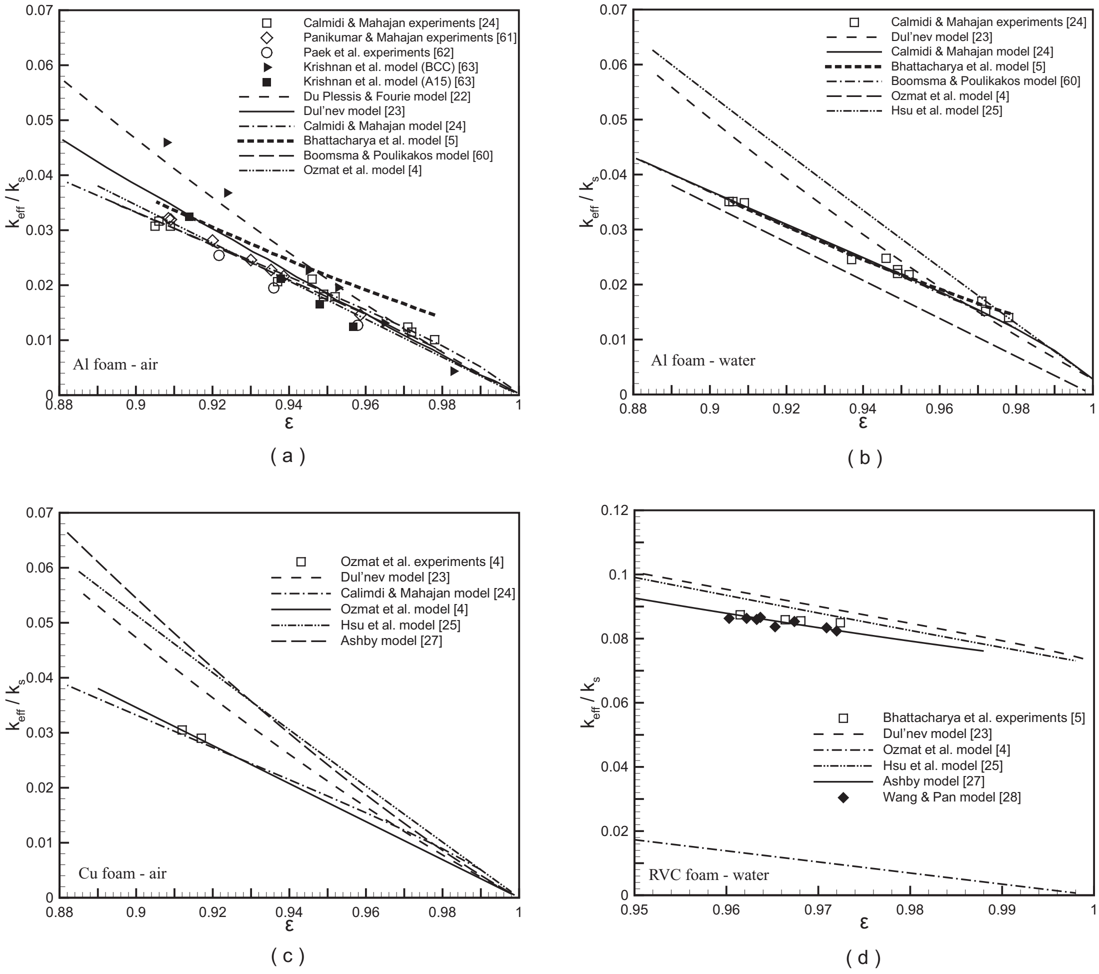

(a) (b) (c) (d)

Figure 2.2: Comparison of existing models with experimental data: (a) Al foam-air; (b) Al foam-water; (c) Cu foam-air; (d) reticulated vitreous carbon (RVC) foam-water

Researcher	Marerial(s)	Porosity	PPI	Dimensions (mm)	Temperature	Notes
Calmidi and Mahajan [24]	Al foam-Air Al foam-Water	0.906-0.978	5, 10, 20, 40	63×63 ×46 (thickness)	room temperature , max temperature diff. of 15°C	○ 2 brazed Al plates at the top of bottom of the sample with thermocouples in each plates ○ electrical heater (top) and cold bath (bottom) ○ maximum heat input 5-8 W
Phanikumar and Mahajan [61]	Ni foam-Water Al foam-Water Al foam-Air RVC foam-Air	0.899-0.9586	5, 10, 20, 40	63.5×63.5 ×50.8 (thickness)	max temperature of 75°C	○ measured natural convection effect ○ electrical heater (bottom) attached to the base of the sample and cold bath (top) ○ heater-sample assembly was insulated from bottom by styrofoam
Bhattacharya et al. [5]	RVC foam-Air RVC foam-Water	0.9615-0.9681	5, 10, 20, 40	75×75 ×43.8 (thickness)	room temperature , max temperature diff. of 15°C	○ similar to Calmidi and Mahajan experiments ○ considered lateral and top heat losses in the analysis
Paek et al. [62]	Al alloy foam-Air	0.89-0.9579	10, 20, 40	90×190 ×9.1 (thickness)	8.4-50°C	○ a stainless steel plate under the foam ○ hot bath (top) and cold bath (bottom) ○ thermocouples were inserted in the top and bottom of the foam and the bottom of the steel plate
Zhao et al. [64]	Steel alloy (FeCrAlY) foam-Air/ Vacuum	0.9, 0.95	30, 60, 90	100 (diameter) 25 (thickness)	320-700K	○ electrical heater (bottom) and cold bath (top) ○ various air pressures (10 E-4 -750 mmHg) ○ considered conduction, convection, and radiation contributions
Sullins and Daryabeigi [65]	Ni foam-N_2	0.968	-	17.46×17.46 ×1.7 (thickness)	100-1000°C	○ radiative hot plate (top) and cold bath (bottom) ○ heat flux gauges located on the cold plate
Schmierer and Razani [21]	Al foam-Vacuum	0.886-0.962	5, 10, 20, 30	31.73 (thickness)	10-60°C	○ stainless steel standard material as the fluxmeter is placed in the top of the foam ○ hot bath (top) and cold bath (bottom) ○ larger temperature gradient wrt. other studies explained by better brazing which results in TCR reduction

Table 2.4: Summary of existing experimental studies on metal foams

- The Wang and Pan model [28] can predict the thermal conductivity of RVC foam-water structures, but it is not obvious that their model can provide a good estimate for other foam structures.
- The Ashby [27] and Hsu et al. [25] models provide good estimates for the effective thermal conductivity when $\lambda \approx O(10^{-1})$ (e.g. RVC foam-water), but highly overestimate the thermal conductivity for $\lambda < 10^{-2}$.
- An empirically determined tuning parameter is involved in the majority of existing models which has been determined by a comparison with the experimental data. These models such as Calmidi and Mahajan model [24] can accurately predict the thermal conductivity for Al foam, but for other foam structures, they overestimate the thermal conductivity. Thus, these models are not appropriate for a general medium.
- The TCR phenomenon has not yet been investigated in any study.

2.2 Fibrous Diffusion Media (GDLs)

A few studies in the literature have focused on the analytical modeling of the thermal conductivity of fibrous media. Ramousse et al. [32] investigated the effective thermal conductivity of non-woven carbon felt GDLs and estimated the conductivity bounds using a model which connected the two phases (solid and gas) in series or parallel. They used the Danes and Bardon correlation [33] to estimate the effective thermal conductivity of the solid phase. The model, as well as the experimental measurements, yielded conductivity values that are lower than most values reported in the literature.

Bauer [34] reported that at the microscopic level in the neighborhood of an individual pore, the longest-range temperature field perturbation induced is that of a "dipole" heat source. Considering a dipole heat source inside each pore and its effect on the others, Bauer [34] found a general relationship for the effective thermal conductivity of porous materials. Applying this general relationship to a fibrous medium with cylindrical fibers (no contact between fibers), he derived the following equation [34].

$$\frac{k_{eff}-k_s}{k_f-k_s}\left\{\frac{k_{eff}+\left[(1-\sin^2\alpha)/(1+\sin^2\alpha)\right]k_s}{k_f+\left[(1-\sin^2\alpha)/(1+\sin^2\alpha)\right]k_s}\right\}^{-\sin^2\alpha/(1+\sin^2\alpha)}=\varepsilon, \tag{2.8}$$

where, α is the average fiber angle with respect to the macroscopic direction of the heat flow. This relationship is highly sensitive to the value of α; for $\alpha = 90$, this measures the through-plane thermal conductivity, and for $\alpha = 0$, this measures the in-plane thermal conductivity.

The complexity of the GDL microstructure and associated challenges in obtaining analytical solutions have led most researchers toward numerical [35, 36, 37] and experimental methods [38, 39, 40, 41, 32]. Hamilton [35] developed a numerical code to determine the effective thermal conductivity of GDLs. He proposed a three-dimensional structure including banks of cylindrical fibers which were perpendicular to neighboring layers. Different distributions of cylindrical fibers were considered to model the anisotropic structure, but the porosity was kept equal for each layer. Using the results of the numerical study, correlations were reported for through-plane and in-plane effective thermal conductivities which generally overestimate the effective thermal conductivities observed in experimental data. Becker et al. [37] used 3D tomography to reconstruct a GDL and a numerically efficient pore morphology method to determine the phase distributions and to deduce the permeability, diffusivity and thermal conductivity as a function of the saturation under different compressive loads. Wang et al. [36] developed a numerical method based on the Lattice Boltzmann technique to predict the effective thermal conductivity of random fibrous media. Assuming a two dimensional stochastic and random microstructure, a generation-growth method was employed to reconstruct the porous medium based on the diameter, length, core position, and alignment of each fiber. Zamel et al. [42] developed a numerical model to estimate the through-plane and in-plane effective thermal conductivity in a dry carbon paper GDL with no Teflon treatment. They studied the effects of porosity, fiber distribution and compression on the effective thermal conductivity and concluded that the effect of fiber distribution is more pronounced in the through-plane direction than the in-plane. Also, they [42] numerically showed that the porosity of GDL is an essential determinant of the effective thermal conductivity but not the compression. Furthermore, Zamel et al. [42] developed correlations for the through-plane and in-plane effective thermal conductivity of a dry GDL with no binder and PTFE content based on their numerical results.

The thermal properties of diffusion media are difficult to investigate by the transient plane source (TPS) method due to the size, material structure and the lack of information about the heat capacities [41]. Therefore, the majority of existing studies have used a guarded-hot-plate apparatus to measure the effective thermal conductivity and TCR. A summary of these studies is presented in Table2.5.

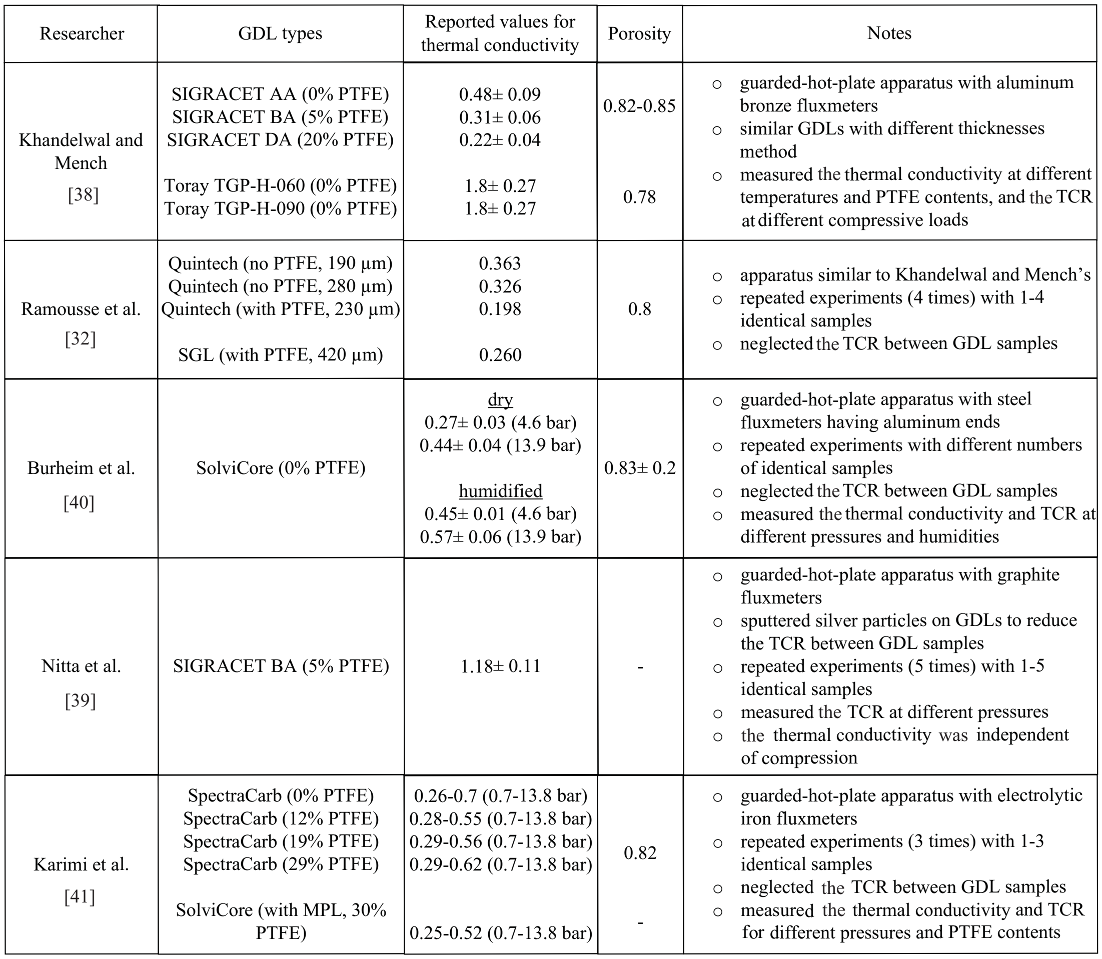

Researcher	GDL types	Reported values for thermal conductivity	Porosity	Notes
Khandelwal and Mench [38]	SIGRACET AA (0% PTFE) SIGRACET BA (5% PTFE) SIGRACET DA (20% PTFE) Toray TGP-H-060 (0% PTFE) Toray TGP-H-090 (0% PTFE)	0.48± 0.09 0.31± 0.06 0.22± 0.04 1.8± 0.27 1.8± 0.27	0.82-0.85 0.78	○ guarded-hot-plate apparatus with aluminum bronze fluxmeters ○ similar GDLs with different thicknesses method ○ measured the thermal conductivity at different temperatures and PTFE contents, and the TCR at different compressive loads
Ramousse et al. [32]	Quintech (no PTFE, 190 μm) Quintech (no PTFE, 280 μm) Quintech (with PTFE, 230 μm) SGL (with PTFE, 420 μm)	0.363 0.326 0.198 0.260	0.8	○ apparatus similar to Khandelwal and Mench's ○ repeated experiments (4 times) with 1-4 identical samples ○ neglected the TCR between GDL samples
Burheim et al. [40]	SolviCore (0% PTFE)	dry 0.27± 0.03 (4.6 bar) 0.44± 0.04 (13.9 bar) humidified 0.45± 0.01 (4.6 bar) 0.57± 0.06 (13.9 bar)	0.83± 0.2	○ guarded-hot-plate apparatus with steel fluxmeters having aluminum ends ○ repeated experiments with different numbers of identical samples ○ neglected the TCR between GDL samples ○ measured the thermal conductivity and TCR at different pressures and humidities
Nitta et al. [39]	SIGRACET BA (5% PTFE)	1.18± 0.11	-	○ guarded-hot-plate apparatus with graphite fluxmeters ○ sputtered silver particles on GDLs to reduce the TCR between GDL samples ○ repeated experiments (5 times) with 1-5 identical samples ○ measured the TCR at different pressures ○ the thermal conductivity was independent of compression
Karimi et al. [41]	SpectraCarb (0% PTFE) SpectraCarb (12% PTFE) SpectraCarb (19% PTFE) SpectraCarb (29% PTFE) SolviCore (with MPL, 30% PTFE)	0.26-0.7 (0.7-13.8 bar) 0.28-0.55 (0.7-13.8 bar) 0.29-0.56 (0.7-13.8 bar) 0.29-0.62 (0.7-13.8 bar) 0.25-0.52 (0.7-13.8 bar)	0.82 -	○ guarded-hot-plate apparatus with electrolytic iron fluxmeters ○ repeated experiments (3 times) with 1-3 identical samples ○ neglected the TCR between GDL samples ○ measured the thermal conductivity and TCR for different pressures and PTFE contents

Table 2.5: Summary of existing experimental studies on the thermal conductivity and contact resistance of GDLs

The available studies in the literature on the thermal contact resistance of GDLs are limited to experimental measurements and there is a lack of analytical investigations in this field. However, several pertinent analytical and experimental approaches have been reported on the electrical contact resistance [43, 44, 45, 46]. These studies have employed fractal based models [43] or the Hertzian elastic theory [44, 45, 46] to find the contact area between the asperity of the GDL and bipolar plate/catalyst layer surfaces and have the potential of being extended to thermal analysis.

2.2.1 Cyclic Compression

To improve the commercialization of fuel cells, the operational lifetime is required to be increased [47]. After a period of operation, some deterioration may occur in fuel cell components leading to a reduction in the overall performance of the stack. Therefore, servicing may be required to increase the lifetime of the fuel cell stack. This servicing involves opening and rebuilding the fuel cell stack over the course of the operational lifetime of the stack which results in cyclic compression of all of the components of the PEM fuel cell stack. In addition, thermal-related phenomena in the gas diffusion layer (GDL) and the catalyst layer can induce hygro-thermal stress and material degradation which compromise performance and lifetime [48, 49]. These phenomena change the compressive load on the fuel cell components during operation. The variation in the compressive load affects all the transport phenomena and consequently the performance of the whole system. Therefore, the effects of cyclic compression on the fuel cell components such as the GDL need to be examined and understood.

Several studies are available on the effects of steady-state compression on fuel cell components and performance; however, the effects of cyclic compression have not yet been studied in-depth. Rama et al. [47] presented a review of the causes and effects of performance degradation and failure in various components of PEM fuel cells. They reported that over-compression and inhomogeneous compression of GDLs induced during stack assembly or during operation reduce the porosity, hydrophobicity, and gas permeability while increasing flooding in GDLs. This leads to an increase in mass transportation losses. Escribano et al. [50] measured the thickness reduction of different types of GDLs including cloth, felt, and paper for the first and second loading over a wide range of compressions. They showed differences in the thickness data; the thickness values for the second loading were smaller and their variations over a range of compressions were smoother. Bazylak et al. [51] used scanning electron microscopy (SEM) to investigate the effect of compression on the morphology of the GDL. They reported that the damage to the GDL is non-uniform under a small compression which was attributed to the surface roughness. However, as the compression pressure increased, the damage became more isotropic over the entire sample [51]. Bazylak et al. [51] experimentally showed that compressing the GDL caused the breakup of fibers and deterioration of the PTFE coating. Khandelwal and Mench [38] investigated the effect of load cycling on the TCR between the GDL and an aluminum bronze material as well as the total resistance of the GDL by compressing the sample to 2MPa and then releasing it for only one cycle. They showed 20% and 38% differences between the loading and unloading data for the total resistance and TCR, respectively.

Although the studies available on the effects of compression-release cycling on GDL properties are limited, numerous investigations have been performed in textile engineering that can be applied to the fibrous structure of GDLs. The first theoretical model in this field was proposed by van Vyk [52, 53] in 1946, which explains the compression behavior of fiber assemblies with random orientations. van Wyk [52, 53] found a linear relationship between the pressure and the cube of the fiber volume fraction. Although van Wyk's relationship is a classical model in textile engineering, it does not include fiber slippage and friction during compression. Also, it does not explain the non-recoverable strain during compression and the mechanical hysteresis during compression-release cycling. Recent studies [54, 55, 56, 57, 58, 59] have focused on accounting for these shortcomings. An approach taken to account for the hysteresis behavior of fibrous media is to model the structure as a combination of series and parallel springs, dashpots, and Coulomb frictional elements [54, 55]. Dunlop [54] found through simulation a hysteresis loop with a shape similar to the experimental data but he did not verify his model. Also, he did not consider the viscoelastic nature of fibers. Applying the force balance, angular momentum balance, and bending equations to the fiber assemblies, the compression hysteresis was theoretically modeled and verified with the experimental data in [56, 57, 58]. The trend in the models and data are similar but the values are different. Also, the hysteresis remains constant with an increase in the number of load cycles, which occurs as a result of neglecting the viscoelastic behavior of fibers. Stankovic [59] measured the strain of different fabrics including hemp, cotton, viscous, and acrylic fabrics under compression-release cycling and observed a hysteresis in the stress-strain curve. He [59] reported that the hysteresis becomes smaller with repeated load cycling and disappears at the fifth cycle.

It can be concluded that the majority of the available studies have focused on the effects of steady-state compression on the structure and properties of GDLs; however, cyclic compression occurs during the operation and servicing of the PEM fuel cell stack. Therefore, it is necessary to study the effects of load cycling on the GDL.

Chapter 3

Summary of Contributions

The main contributions in this dissertation are included in the six journal papers provided in Appendices A-F. This chapter summarizes these contributions and explains how they are connected towards the overall objective of this work.

3.1 Thermal Spreading Resistance of Arbitrary-Shape Heat Sources on a Half-Space: A Unified Approach

Thermal spreading/constriction resistance is an important phenomenon where a heat source/sink is in contact with a body. Thermal spreading resistance associated with heat transfer through the mechanical contact of two bodies occurs in a wide range of applications: microelectronics cooling, spacecraft structures, satellite bolted joints, nuclear engineering, ball bearings, and heat exchangers. The real contact area forms typically a few percent of the nominal contact area. In practice, due to the random nature of the surface roughness of contacting bodies, the actual shape of microcontacts is unknown; therefore, it is valuable to have a model which is applicable to arbitrary-shape heat sources. The complexity of applying boundary conditions associated with random shapes makes it difficult to develop a general analytical solution for spreading resistance. The objective of this contribution was to establish a compact analytical model that allows one to accurately calculate the spreading resistance over a wide variety of heat source shapes under both isoflux and isothermal conditions.

In the majority of applications, especially in porous materials, the dimensions of microcontacts (heat sources) are small enough compared with the distance between them and the dimensions of the body through which the heat spreads to use the half-space hypothesis. In the present study, using the analytical solution of an elliptical heat source on a half-space, a compact general model was developed which is only a function of the heat source geometric parameters (i.e., the square root of the area and aspect ratio). The methodology used in this study to establish and verify the model was a “bottom-up” approach.

To verify the model, analytical solutions were developed for several geometries including a trapezoid, a circular sector, a circular segment, a rectangle with semicircular ends, and a rectangle with round ends. Using the “bottom-up” approach, it was shown that for a wide variety of heat source shapes, the proposed model is in good agreement with the existing and/or developed analytical solutions with maximum differences on the order of 8%.

For further information, the reader is referred to Appendix A.

3.2 Analytic Determination of the Effective Thermal Conductivity of PEM Fuel Cell Gas Diffusion Layers

Accurate information about the temperature field and associated heat transfer rates are particularly important in devising appropriate heat and water management strategies in proton exchange membrane (PEM) fuel cells. The temperature field affects the relative humidity, membrane water content, reaction kinetics, as well as the durability. An important parameter in fuel cell performance analysis is the effective thermal conductivity of the GDL. Estimation of the effective thermal conductivity is complicated due to the random nature of the GDL microstructure.

The objective of this contribution was to develop a compact analytical model for evaluating the effective thermal conductivity of fibrous GDLs. The medium structure was modeled as cylindrical carbon fibers that are equally spaced horizontally and stacked vertically to form mechanical contacts. The methodology to model heat conduction in the medium was a basic (unit) cell approach. In this approach, the basic cell was considered to be representative of the medium. Each cell was made up of a contact region which was composed of a contact area between two portions of fibers, surrounded by a gas (air) layer. Based on this geometry, a compact thermal resistance model was constructed which takes into account the basic conduction processes through the solid fibrous matrix and the gas phase. Other important phenomena including the spreading resistance associated with the contact area between overlapping fibers and gas rarefaction effects in microgaps were also considered in the model. Furthermore, the model accounted for salient geometric and mechanical features such as the fiber orientation and compressive forces due to cell/stack clamping.

Model predictions showed good agreement with existing experimental data over a wide range of porosities. Parametric studies were performed using the proposed model to investigate the effects of the bipolar plate pressure, aspect ratio, fiber diameter, fiber angle, and operating temperature. The developed model can be used to guide the design of improved GDLs, and can be readily implemented into fuel cell models that require one to specify the effective thermal conductivity.

For further information, the reader is referred to Appendix B.

3.3 Effective Thermal Conductivity and Thermal Contact Resistance of Gas Diffusion Layers in PEM Fuel Cells. Part 1: Effects of Compressive Load

Any successful fuel cell thermal analysis requires two key transport coefficients: 1) the effective thermal conductivity of the gas diffusion layer (GDL) as a function of the microstructural geometry of the GDL and the operating conditions (e.g. compressive load and temperature); and 2) the thermal contact resistance (TCR). In the majority of the previous studies related to heat transfer in the GDL, the TCR was 'bundled up' with the effective thermal conductivity and characterized using an aggregate value. Furthermore, the effect of the compressive load on the TCR as well as the thermal conductivity has not been thoroughly investigated. The main objective of this study was to develop an experimental technique that allows the deconvolution of the TCR and the thermal conductivity. To achieve this goal, a custom-made test bed was designed and built that enables one to measure the thermal conductivity and TCR of porous media under vacuum and ambient pressure conditions. Toray carbon papers with a porosity of 78% and different thicknesses were used in the experiments. The effects of the ambient pressure and compression were investigated, including a measurement of the GDL thickness variation using a tensile-compression apparatus. The effective thermal conductivity and TCR were deduced from the total thermal resistance measurements by performing a series of experiments with GDL samples of various thicknesses and similar microstructures. The effect of the operating temperature on both the thermal conductivity and TCR was also investigated. An important finding in this study was the dominant contribution of thermal contact resistance to the total thermal resistance. The ratio of the thermal contact to bulk GDL resistance was shown to be at least 2:1 and remained approximately constant over a wide range of compressions.

Another objective of this contribution was to develop analytical models for the effective thermal conductivity and TCR under compression. Our previous model for the effective thermal conductivity, outlined in Appendix B, was modified to include porosity changes, microstructural deformation, and fiber slippage under a compressive load. Also, using the Greenwood and Williams statistical model, a novel analytical model was developed to evaluate the TCR at the interface of the GDL and a solid surface as a function of the compressive load. These models were compared against experimental data obtained in this study.

This work has helped to clarify the impact of several operational parameters on the thermal properties of GDLs and provided new insights on the importance of a key interfacial phenomenon. For further information, the reader is referred to Appendix C.

3.4 Effective Thermal Conductivity and Thermal Contact Resistance of Gas Diffusion Layers in PEM Fuel Cells. Part 2: Hysteresis Effect under Cyclic Compressive Load

Commercialization of PEM fuel cells requires further progress in improving operational lifetime. A number of degradation mechanisms need to be better understood, including those associated with the deterioration of the gas diffusion layer (GDL) due to mechanical stresses. In practice, the GDL will be subjected to additional hygrothermal stresses that arise due to varying temperature and relative humidity during operation, and that are *cyclic* in nature. These stresses induce material degradation and compromise cell performance and lifetime. The variation in the compressive load affects all the transport phenomena and consequently the performance of the entire system. The objective of this contribution was to investigate the effects of loading-unloading cycles on the thermal, mechanical, and geometrical properties of GDLs.

The effective thermal conductivity and TCR were measured using our custom-made apparatus described in Appendix C. Also, the variations in the GDL thickness over a range of cyclic compressions between 0 and 1.5 MPa was measured using a standard tensile-compression apparatus. Due to fiber breakage, microstructure disorientation, and plastic and viscoelastic deformations, the thermal and structural properties looked different at the same pressure for loading and unloading processes. The experiment was continued successively up to a cycle at which this hysteresis approached zero. Our results showed that this behavior occurred for the fifth compression-release cycle. A maximum hysteresis was observed for the TCR with a difference of 34.5% between the 1st and 5th loading-unloading data. Also, the results showed an increase in the effective thermal conductivity during the unloading because of irreversible deformations which occurred during the loading process.

This work provided new insights on the effects of unsteady/cyclic compression on the thermal and structural properties of GDLs. The outcomes of this study can be used to analyze the fuel cell operation more accurately, and can be provided as inputs to fuel cell models which require the specification of the effective thermal conductivity, TCR, thickness, and porosity. For more information, the reader is referred to Appendix D.

3.5 A Novel Approach to Investigate the In-Plane Thermal Conductivity of Gas Diffusion Layers in Proton Exchange Membrane Fuel Cells

The GDL microstructure consists of carbon fibers randomly oriented in a plane and relatively organized in the normal direction to the plane. The nature of this structure makes the thermal conductivity of the medium anisotropic. Heat transfer in GDLs occurs in both the through-plane and in-plane directions due to the uneven structure of the bipolar plates; therefore, the in-plane thermal conductivity is an important parameter in the thermal modeling of GDLs. The brittle and thin structure of GDLs makes it challenging to measure the in-plane thermal conductivity.

The aim of this contribution was to measure the in-plane thermal conductivity of GDLs. For the first time in the literature, a novel test bed was designed and built that enables the measurements of the thermal conductivity of any thin and delicate material in the in-plane direction. The test set-up consisted of two fluxmeters, two sample holders, and cold and hot plates. GDL samples were inserted in the grooves of the sample holders. The experiments were performed under a vacuum chamber to ensure that the convection heat transfer is negligible. To reduce the contact resistance between the groove walls and the samples, the inside of each groove was covered by a thermal paste. Toray carbon papers with the porosities of 78% and different wet proofing percentages (PTFE contents) were used in the experiments. Temperatures were recorded continuously until a steady-state condition was achieved. This took approximately 7 hours for each set of experiments. To find the in-plane thermal conductivity, two experiments were performed for each carbon paper with different sample lengths. Results showed that the in-plane effective thermal conductivity remains approximately constant, $k \approx 17.5 W/mK$, over a wide range of PTFE content, and it is approximately 12 times higher than the through-plane conductivity. In addition, a compact model was developed for the in-plane thermal conductivity that accounted for the heat conduction through randomly oriented fibers, contact area between fibers, and PTFE covered regions. The model predictions are in good agreement with experimental data over a range of PTFE content. For additional information, the reader is directed to Appendix E.

3.6 Thermal Conductivity and Contact Resistance of Metal Foams

Recently, open-cell metal foams have received a large amount of attention. The ultra-low density, high surface area-to-volume ratio, relatively low cost, and ability to mix the passing fluid give them a great potential to be used in a variety of unique thermal-hydraulic applications (e.g., microelectronics cooling, fuel cells, and compact heat exchangers). In the majority of these applications, there is a contact between the metal foam and other solid surfaces which gives rise to an important phenomenon called thermal contact resistance (TCR) which acts against heat transfer. Due to the high porosity and roughness of the free surface of metal foams, the actual contact area at the interface with a solid surface is very small; this emphasizes the significance of the TCR at metal foam-solid surface interfaces.

The goal of this contribution was to measure the thermal conductivity and contact resistance of metal foams. A systematic experimental approach was taken to find the actual contact area and the thermal contact resistance of metal foams. The thermal test bed described in Appendix C was employed to measure the thermal conductivity and TCR of metal foams at atmospheric pressure. ERG Duocel aluminum foams with various porosities and pore densities were used in the experiments. The effective thermal conductivity and TCR were deduced from the total thermal resistance measurements by performing a series of experiments with Al foam samples of various thicknesses and similar microstructures (porosity and pore density). The effects of compression, porosity, and pore density were studied on the effective thermal conductivity and TCR. Results showed that the porosity and the effective thermal conductivity remained unchanged with the variation of pressure in the range of 0 to 2 MPa; however, the TCR decreases significantly with pressure due to an increase in the contact area.

The second goal of this study was to measure the actual contact area at the metal foam-solid surface interface for different compressive loads. A pressure sensitive carbon paper was placed between the foam and the solid surface to print the contact spots. An image analysis technique implemented in MATLAB software was developed to analyze the produced images and find the contact areas. Results showed that the area ratio of 0-1.3%, which significantly depends on the compression. For further information, the reader is referred to Appendix F.

Chapter 4

Conclusions and Future Work

The main contributions of this dissertation were to develop comprehensive analytical and experimental studies on thermal transport in porous media. The studied transport phenomena included the effective thermal conductivity and thermal contact resistance (TCR). On the analytical side, geometrical, mechanical, and thermal modeling of the microstructure was included in this study with a focus on fuel cell diffusion media (GDLs) and metal foams. Two separate test beds were designed and built to measure the through-plane conductivity, TCR, and in-plane thermal conductivity. Using the novel designed test set-up, for the first time in the literature, the in-plane thermal conductivity of GDLs with a variety of wet proofing contents was measured. The set-up has the capability to be used for thermal conductivity measurements of any thin and brittle material which cannot be done with regular methods. The outcomes of this dissertation provide new insights on thermal transport in highly porous materials and will improve the design of related systems such as fuel cells and compact heat exchangers. The key contributions of this dissertation can be summarized as follows:

1. The model proposed for determining the spreading resistance of an arbitrary-shape heat source on a half-space is a compact analytical model, which is only a function of the heat source geometric parameters (the square root of the area and the aspect ratio). The model was verified against the developed and existing analytical solutions of a wide variety of heat source geometries including a trapezoid, a circular sector, a circular segment, a rectangle with semicircular ends, and a rectangle with round ends, with a maximum difference of 8%. For aspect ratios greater than 0.3, which is the case in the majority of applications,

the difference between the analytical soultions and the model is less than 4%. Also, results showed that the ratio of isothermal to isoflux spreading resistance is approximately 0.931 for a wide range of shapes with different aspect ratios. Since the actual shapes of microcontacts in unknown, the generalized model developed in this dissertation benefits all researchers dealing with contacting bodies such as those found in fuel cells and microelectronic cooling.

2. The model developed for the through-plane effective thermal conductivity of a fibrous GDL accurately predicted the effective thermal conductivity over a wide range of porosities. Results showed that the constriction/spreading resistance at the interface between fibers was the controlling component of the total thermal resistance. Also, an orthogonal arrangement of fibers ($\theta = 0$) yielded better overall agreement with experimental data. The influence of fiber angle θ on the effective thermal conductivity decreased at higher porosities. Reducing the aspect ratio to approximately 0.7 had a negligible impact on the effective thermal conductivity; however, for aspect ratios less than 0.3, this effect became important. The analysis indicated that the best effective thermal conductivity is achieved for the square arrangement of fibers. It was also found that neither changes in the fiber diameter nor operating temperature have any significant impact on the effective thermal conductivity whereas higher bipolar pressures significantly improve the effective thermal conductivity.

3. The modified model for the through-plane effective thermal conductivity of GDLs accounted for the elastic deformation and slippage of fibers as a result of compression. This model was accompanied with an analytical model for the thermal contact resistance at the interface of the GDL and a solid surface. The predictions of both models were in good agreement with the developed experimental data over a wide range of compressive loads from 0.2 to 1.5 MPa. Parametric studies performed to investigate the trends and effects of compression, conduction in air, and the operating temperature showed that the effective thermal conductivity increases with the compressive load and decreases with an increase in the operating temperature; however, it was found to be relatively insensitive to the ambient air pressure. An important finding was the dominant contribution of the thermal contact resistance to the total thermal resistance. The ratio of the thermal contact to bulk GDL resistance remains approximately constant (4.6:1 for TGP-H-060 at atmospheric pressure), over a wide range of

conditions. This work provided valuable information on the thermal and mechanical modeling of fibrous materials such as GDLs and showed the importance of the TCR in the thermal analysis as a key interfacial phenomenon.

4. The hysteresis observed in load cycling experiments for the thermal and structural properties of the Toray carbon paper decreased with an increase in the number of load cycles and became negligible at the fifth cycle. Results showed a significant hysteresis in the total thermal resistance, TCR, effective thermal conductivity and porosity. This hysteresis was more profound for the TCR but it was relatively small for the effective thermal conductivity. The hysteresis for the TCR started with 22.5% at the first cycle, continued to 28.4% at the second cycle and reached to 34.5% at the end (5th cycle). The hysteresis in the thermal conductivity was produced due to hysteresis in the total thermal resistance, TCR, and porosity. The hysteresis in the total thermal resistance and TCR increased the thermal conductivity during unloading whereas the mechanical hysteresis (reduction in the thickness) had the reverse effect; therefore, the effective thermal conductivity hysteresis was smaller compared to that of the TCR. This effect caused a maximum difference of 6.5% betweem the effective conductivity values of the unloaded GDL at the fifth cycle and the loaded GDL at the starting point. In practice, a fuel cell stack passes many loading-unloading cycles; therefore, the steady-state values for properties found in this study can be used in PEM fuel cell modeling.

5. An important finding in the in-plane thermal conductivity study was that the in-plane effective thermal conductivity remains almost unchanged, $k \approx 17.5 W/mK$, over a wide range of PTFE content. However, the thermal contact resistance and the end effects increases with PTFE content due to increased number of PTFE coated fibers. Results indicated a large difference in the effective conductivity values of through-plane and in-plane directions. Neglecting this difference results in large errors in the thermal analysis of the fuel cell system. The experimental study was accompanied with an analytical model, which accounted for the heat conduction through the randomly oriented fibers, the contact area between fibers, and the PTFE covered regions. The model predictions were in good agreement with experimental data over a range of PTFE content. This work has helped to clarify the effect of PTFE content on the effective thermal conductivity and contact resistance of GDLs and provided

input data for fuel cell models which requires thermal properties of GDLs in different directions.

6. A systematic experimental approach was developed to measure the thermal conductivity, the thermal contact resistance, and the actual contact area of metal foams under various compressive loads. The present experimental data for the effective thermal conductivity were in good agreement with the existing data over a range of porosities. Results showed that the effective thermal conductivity increased with an increase in the foam density, but it was relatively insensitive to the compressive load in the range of 0-2 MPa. An important finding was the large contribution of the thermal contact resistance to the total thermal resistance (more than 50%, for relatively low compressive loads). The high values of the TCR are related to very small ratio of contact area to the cross-sectional area; the maximum ratio is 1.25% at the contact pressure of 3 MPa. The TCR was more sensitive to the compressive load rather than the porosity and pore density; however, it slightly decreased with an increase in the foam density and pore density. This work provided new insights on the importance of thermal contact resistance and clarified the impact of this key interfacial phenomenon on the thermal analysis of metal foams.

4.1 Future Work

In the work presented in this thesis, thermal transport in PEM fuel cell gas diffusion layers as well as metal foams was studied experimentally and analytically. With respect to the individual contributions of this dissertation, the following is suggested for future work:

- The existing experimental methodology can be used to study different types of commonly used GDLs including carbon-fiber and carbon-cloth GDLs. Comparing the results, an optimum structure can be found to meet the desired condition. This study can help to find an optimum structure and material for the GDL microstructure and can lead to make an engineering GDL.

- Effects of important parameters such as compression, temperature and porosity on the in-plane heat transfer can be studied. The outcomes of this study will provide new insights on the in-plane thermal conductivity of GDLs. Also, the relative importance of the studied parameters for the in-plane direction can be found in a comparison with the through-plane results found in this thesis. This comparison can help to find an appropriate pressure and temperature range which can lead to a less resistant path for the heat transfer through GDLs.

- In the existing test rig, a uniform pressure was applied on GDLs. To provide a more practical condition, a nonuniform plate as a representation of the bipolar plate can be added to the top and the bottom of the GDL sample between the two fluxmeters. The Temperature at different locations of these plates can be measured using the attached thermocouples. This study will provide new information on the effective thermal conductivity and thermal contact resistance of GDLs under nonuniform compression.

- Investigating the effects of the liquid and vapor water content in the GDL can be added to the present study to make it more practical. Water is produced as a result of electrochemical reactions in fuel cells and passes through the GDL, affecting its thermal and mechanical properties. Since the thermal conductivity of water is higher than that of air, it improves the thermal conductivity of the GDL and reduces the thermal contact resistance on both sides of the GDL at the interface with the bipolar plate and the catalyst layer.

- The existing test rig can be modified to measure the thermal transport in other fuel cell components, specifically the membrane and catalyst layer. New insights on the thermal conductivity of components and the thermal contact resistance at all interfaces which will be found through the experiments will benefit fuel cell design and provide valuable inputs for the thermal modeling of the fuel cell stack.

- A numerical study of the GDL microstructure would be useful to investigate the effect of fiber randomness and orientation on the thermal properties of GDLs. The microstructure could be modeled as cylindrical fibers with the same cross-section. Different distribution functions for length and orientation of fibers can be considered to construct a random microstructure. The contact area between the fibers can be modeled as an overlap of the fibers with an amount based on the stress-strain experimental data. For the thermal analysis, the Lattice Boltzmann method is suggested, which is powerful in applying boundary conditions in microscale and complex geometries.

- The thermal contact resistance model can be modified using an in-depth knowledge of fibers at the interface with a solid surface. This can be acquired through an image analysis of the GDL surface tomography. Based on the image analysis results, a statistical configuration of fibers at and near the contact surface can be found. Mechanical modeling will accompany the geometrical model to evaluate the size and distribution of microcontacts and the thermal analysis can be performed to find the thermal contact resistance.

- A test bed can be designed and built to measure the electrical conductivity and electrical contact resistance for different components of fuel cells. The outcomes of this study would improve the electrical models requiring these properties. It also can be used to improve the design of fuel cell components to reduce electrical losses. Moreover, since the electrical and thermal transport relationships are similar, a general contribution can be made to link the electrical and thermal transport properties.

- The thermal transport in hollow ligament metal foams can be studied analytically and experimentally. Depending on the metal type and the manufacturing process, the metal foam structure can have solid or hollow ligaments. It would be beneficial to perform parametric studies and compare both structures geometrically and thermally. The result can help one to choose a proper material and manufacturing process for each application.

Bibliography

[1] D. A. Nield and A. Bejan, *Convection in Porous Media*, ch. 1. NY, USA: Springer Science+Business Media, Inc., third ed., 2006.

[2] D. B. Ingham and I. Pop, *Transport Phenomena in Porous Media II*, ch. 1. OXford, UK: Pergamon, 2002.

[3] N. Dukhan, R. Picon-Feliciano, and A. R. Alvarez-Hernandez, “Heat transfer analysis in metal foams with low-conductivity fluids,” *Journal of Heat Transfer*, vol. 128, no. 8, pp. 784–792, 2006.

[4] B. Ozmat, B. Leyda, and B. Benson, “Thermal applications of open-cell metal foams,” *Materials and Manufacturing Processes*, vol. 19, no. 5, pp. 839–862, 2004.

[5] A. Bhattacharya, V. V. Calmidi, and R. L. Mahajan, “Thermophysical properties of high porosity metal foams,” *International Journal of Heat and Mass Transfer*, vol. 45, pp. 1017–1031, 2002.

[6] M. L. Hunt and C. L. Tien, “Effects of thermal dispersion on forced convection in fibrous media,” *International Journal of Heat and Mass Transfer*, vol. 31, pp. 301–309, 1988.

[7] N. Djilali and D. Lu, “Influence of heat transfer on gas and water transport in fuel cells,” *International Journal of Thermal Sciences*, vol. 41, no. 1, pp. 29 – 40, 2002.

[8] T. Berning and N. Djilali, “Three-dimensional computational analysis of transport phenomena in a pem fuel cell–a parametric study,” *Journal of Power Sources*, vol. 124, no. 2, pp. 440 – 452, 2003.

[9] J. A. Greenwood and B. P. Williamson, "Contact of nominally flat surfaces," *Proceedings of the Royal Society of London. Series A, Mathematical and Physical Sciences*, vol. 295, pp. 300–319, Dec. 1966.

[10] D. Tabor, *The Hardness of Metals*. London E.C.4, UK: Oxford University Press, 1951.

[11] H. S. Carslaw and J. C. Jaeger, *Conduction of Heat in Solids*. London, UK: Oxford University Press, second ed., 1959.

[12] J. C. Maxwell, *A Treatise on Electricity and Magnetism*, ch. 9. NY, USA: Dover Publications Inc., reprinted 1954.

[13] J. K. Carson, S. J. Lovatt, D. J. Tanner, and A. C. Cleland, "Thermal conductivity bounds for isotropic, porous materials," *International Journal of Heat and Mass Transfer*, vol. 48, pp. 2150–2158, 2005.

[14] R. Landauer, "The electrical resistance of binary metallic mixtures," *Journal of Applied Physics*, vol. 23, pp. 779–784, 1952.

[15] S. Kirkpatrick, "Percolation and conduction," *Rev. Mod. Phys.*, vol. 45, pp. 446–452, 1973.

[16] O. Wiener, "Die theorie des mischkorpers fur das feld der statonaren stromung. i. die mittelwertsatze fur kraft, polarisation und energie," *Abh. Math. Phys. K1 Knigl. Schs. Ges.*, vol. 32, pp. 509–604, 1912.

[17] O. Krischer, *Die wissenschaftlichen Grundlagen der Trocknungstechnik (The Scientific Fundamentals of Drying Technology)*. NY, USA: Springer-Verlag, 1963.

[18] D. R. Chaudhary and R. C. Bhandari, "Heat transfer through a three-phase porous medium," *J. Phys. D (Brit. J. Appl. Phys.)*, vol. 1, pp. 815–817, 1968.

[19] T. Renaud, P. Briery, J. Andrieu, and M. Laurent, "Thermal properties of model foods in the frozen state," *J. Food Eng.*, vol. 15, no. 2, pp. 83–97, 1992.

[20] R. Hamilton and O. K. Crosser, "Thermal conductivity of heterogeneous two-component systems," *IEC Fund.*, vol. 1, no. 3, pp. 187–191, 1962.

[21] E. N. Schmierer and A. Razani, “Self-consistent open-celled metal foam model for thermal applications,” *Journal of Heat Transfer*, vol. 128, no. 11, pp. 1194–1203, 2006.

[22] J. G. Fourie and J. P. D. Plessis, “Effective and coupled thermal conductivities of isotropic open-cellular foams,” *AIChe Journal*, vol. 50, no. 3, pp. 547–556, 2004.

[23] G. N. Dulnev, “Heat transfer through solid disperse systems,” *Journal of Engineering Physics and Thermophysics*, vol. 9, no. 3, pp. 275–279, 1965.

[24] V. V. Calmidi and R. L. Mahajan, “The effective thermal conductivity of high porosity fibrous metal foams,” *Journal of Heat Transfer*, vol. 121, pp. 466–471, May 1999.

[25] C. T. Hsu, P. Cheng, and K. W. Wong, “Modified zehner-schlunder models for stagnant thermal conductivity of porous media,” *International Journal of Heat and Mass Transfer*, vol. 37, no. 17, pp. 2751–2759, 1994.

[26] H. W. Russell, “Principles of heat flow in porous insulators,” *Journal of the American Ceramic Society*, vol. 18, no. 1-12, pp. 1–5, 1935.

[27] M. F. Ashby, “The properties of foams and lattices,” *Phil. Trans. R. Soc. A*, vol. 364, pp. 15–30, 2006.

[28] M. Wang and N. Pan, “Modeling and prediction of the effective thermal conductivity of random open-cell porous foams,” *International Journal of Heat and Mass Transfer*, vol. 51, no. 5-6, pp. 1325 – 1331, 2008.

[29] T. Log and S. E. Gustafsson, “Transient plane source (tps) technique for measuring thermal transport properties of building materials,” *Fire Mater.*, vol. 19, pp. 39–43, 1995.

[30] M. Gustavsson, E. Karawacki, and S. E. Gustafsson, “Thermal conductivity, thermal diffusivity and specific heat of thin samples from transient measurements with hot-disk sensors,” *Rev. Sci. Instrum.*, vol. 65, pp. 3856–3859, 1994.

[31] E. Solrzano, J. Reglero, M. Rodrguez-Prez, D. Lehmhus, M. Wichmann, and J. de Saja, “An experimental study on the thermal conductivity of aluminium

foams by using the transient plane source method," *International Journal of Heat and Mass Transfer*, vol. 51, no. 25-26, pp. 6259–6267, 2008.

[32] J. Ramousse, S. Didierjean, O. Lottin, and D. Maillet, "Estimation of the effective thermal conductivity of carbon felts used as pemfc gas diffusion layers," *International Journal of Thermal Sciences*, vol. 47, no. 1, pp. 1 – 6, 2008.

[33] F. Danes and J. P. Bardon, "Conductivit thermique des feutres de carbone, isolants forte anisotropie : modle de conduction par la phase solide," *Revue Gnrale de Thermique*, vol. 36, pp. 302–311, 1997.

[34] T. H. Bauer, "A general analytical approach toward the thermal conductivity of porous media," *International Journal of Heat and Mass Transfer*, vol. 36, no. 17, pp. 4181–4191, 1994.

[35] D. J. Hamilton, "A numerical method to determine eective transport coefficients in porous media with application to pem fuel cells," m. eng. thesis, Queen's University, Kingston, ON, CA, 2005.

[36] M. Wang, J. He, J. Yu, and N. Pan, "Lattice boltzmann modeling of the effective thermal conductivity for fibrous materials," *International Journal of Thermal Sciences*, vol. 46, no. 9, pp. 848 – 855, 2007.

[37] J. Becker, V. Schulz, and A. Wiegmann, "Numerical determination of two-phase material parameters of a gas diffusion layer using tomography images," *J. Fuel Cell Sci. Technol.*, vol. 5, no. 2, pp. 21006–21015, 2008.

[38] M. Khandelwal and M. Mench, "Direct measurement of through-plane thermal conductivity and contact resistance in fuel cell materials," *Journal of Power Sources*, vol. 161, no. 2, pp. 1106 – 1115, 2006.

[39] I. Nitta, O. Himanen, and M. Mikkola, "Thermal conductivity and contact resistance of compressed gas diffusion layer of pem fuel cell," *Fuel Cells*, vol. 8, no. 2, pp. 111–119, 2008.

[40] O. Burheim, P. Vie, J. Pharoah, and S. Kjelstrup, "Ex situ measurements of through-plane thermal conductivities in a polymer electrolyte fuel cell," *Journal of Power Sources*, vol. 195, no. 1, pp. 249 – 256, 2010.

[41] G. Karimi, X. Li, and P. Teertstra, "Measurement of through-plane effective thermal conductivity and contact resistance in pem fuel cell diffusion media," *Electrochimica Acta*, vol. 55, no. 5, pp. 1619 – 1625, 2010.

[42] N. Zamel, X. Li, J. Shen, J. Becker, and A. Wiegmann, "Estimating effective thermal conductivity in carbon paper diffusion media," *Chemical Engineering Science*, vol. 65, no. 13, pp. 3994 – 4006, 2010.

[43] V. Mishra, F. Yang, and R. Pitchumani, "Measurement and prediction of electrical contact resistance between gas diffusion layers and bipolar plate for applications to pem fuel cells," *J. Fuel Cell Sci. Technol.*, vol. 1, no. 1-2, pp. 2–9, 2004.

[44] Y. Zhou, G. Lin, A. Shih, and S. Hu, "A micro-scale model for predicting contact resistance between bipolar plate and gas diffusion layer in pem fuel cells," *Journal of Power Sources*, vol. 163, no. 2, pp. 777 – 783, 2007.

[45] Z. Wu, S. Wang, L. Zhang, and S. J. Hu, "An analytical model and parametric study of electrical contact resistance in proton exchange membrane fuel cells," *Journal of Power Sources*, vol. 189, no. 2, pp. 1066 – 1073, 2009.

[46] T. Swamy, E. Kumbar, and M. Mench, "Characterization of interfacial structure in pefcs: Water storage and contact resistance model," *Journal of The Electrochemical Society*, vol. 157, no. 1, pp. B77–B85, 2010.

[47] P. Rama, R. Chen, and J. Andrews, "A review of performance degradation and failure modes for hydrogen-fuelled polymer electrolyte fuel cells," *Proceedings of the Institution of Mechanical Engineers, Part A: Journal of Power and Energy*, vol. 222, no. 5, pp. 421–441, 2008.

[48] A. Kusoglu, M. H. S. Y. Tang, A. M. Karlsson, S. Cleghorn, and W. B. Johnson, "Stress-strain behavior of perfluorosulfonic acid membranes at various temperatures and humidities: Experiments and phenomenological modeling," *J. Fuel Cell Sci. Technol.*, vol. 6, no. 1, pp. 011012–011019, 2009.

[49] A. Kusoglu, A. M. Karlsson, M. H. Santare, S. Cleghorn, and W. B. Johnson, "Mechanical response of fuel cell membranes subjected to a hygro-thermal cycle," *Journal of Power Sources*, vol. 161, no. 2, pp. 987 – 996, 2006.

[50] S. Escribano, J.-F. Blachot, J. Ethve, A. Morin, and R. Mosdale, “Characterization of pemfcs gas diffusion layers properties,” *Journal of Power Sources*, vol. 156, no. 1, pp. 8 – 13, 2006. Selected papers from the 2nd France-Deutschland Fuel Cell Conference.

[51] A. Bazylak, D. Sinton, Z.-S. Liu, and N. Djilali, “Effect of compression on liquid water transport and microstructure of pemfc gas diffusion layers,” *Journal of Power Sources*, vol. 163, no. 2, pp. 784 – 792, 2007.

[52] C. van Wyk, “A study of the compressibility of wool, with special reference to south african merino wool,” *Onderstepoort J. Vet. Sci. Anim. Ind.*, vol. 21, pp. 99–107, 1946.

[53] C. van Wyk, “Note on the compressibility of wool,” *J. Textile Inst.*, vol. 37, pp. T285–T305, 1946.

[54] J. I. Dunlop, “On the compression characteristics of fibre masses,” *J. Textile Inst.*, vol. 74, no. 2, pp. 92–97, 1983.

[55] I. Krucinska, I. Jalmuzna, and W. Zurek, “Modified rheological model for analysis of compression of nonwoven fabrics,” *Textile Research Journal*, vol. 74, no. 2, pp. 127–133, 2004.

[56] G. A. Carnaby and N. Pan, “Theory of the compression hysteresis of fibrous assemblies,” *Textile Research Journal*, vol. 59, no. 5, pp. 275–284, 1989.

[57] N. B. Beil and W. W. Roberts, “Modeling and computer simulation of the compressional behavior of fiber assemblies: Part i: Comparison to van wyk’s theory,” *Textile Research Journal*, vol. 72, no. 4, pp. 341–351, 2002.

[58] N. B. Beil and W. W. Roberts, “Modeling and computer simulation of the compressional behavior of fiber assemblies: Part ii: Hysteresis, crimp, and orientation effects,” *Textile Research Journal*, vol. 72, no. 5, pp. 375–382, 2002.

[59] S. B. Stankovic, “Compression hysteresis of fibrous systems,” *Polymer Engineering and Science*, vol. 48, no. 4, pp. 676–682, 2008.

[60] K. Boomsma and D. Poulikakos, “On the effective thermal conductivity of a three-dimensionally structured fluid-saturated metal foam,” *International Journal of Heat and Mass Transfer*, vol. 44, pp. 827–836, 2001.

[61] M. S. Phanikumar and M. L. Mahajan, “Non-darcy natural convection in high porosity metal foams,” *International Journal of Heat and Mass Transfer*, vol. 45, pp. 3781–3793, 2002.

[62] J. W. Paek, B. H. Kang, S. Y. Kim, and J. M. Hym, “Effective thermal conductivity and permeability of aluminum foam materials,” *International Journal of Thermophysics*, vol. 21, no. 2, pp. 453–464, 2000.

[63] S. Krishnan, S. Garimella, and J. Y. Murthy, “Simulation of thermal transport in open-cell metal foams: Effects of periodic unit-cell structure,” *Journal of Heat Transfer*, vol. 130, no. 2, pp. 024503–024507, 2008.

[64] C. Y. Zhao, T. J. Lu, H. P. Hodson, and J. D. Jackson, “The temperature dependence of effective thermal conductivity of open-celled steel alloy foams,” *Materials Science and Engineering A*, vol. 367, pp. 123–131, 2004.

[65] A. D. Sullins and K. Daryabeigi, “Effective thermal conductivity of high porosity open cell nickel foam,” in *Proceedings of the 35th AIAA Thermophysics Conference*, (American Institute of Aeronautics and Astronautics, The Combustion Institute, Pittsburg, PA), pp. 1039–1046, 2001.

[66] V. S. Arpaci and P. S. Larsen, *Convection Heat Transfer*, ch. 4. NJ: Prentice-Hall, Englewood Cliff, 1984.

[67] F. P. Incropera and D. P. DeWitt, *Fundamentals of Heat and Mass Transfer*, ch. 13. New York, USA: John Willey and Sons, fourth ed., 1996.

Appendix A

Assumptions

The following is a summary of assumptions considered in the theoretical and experimental parts of this dissertation.

A.1 Thermal Spreading Resistance of Arbitrary-Shape Heat Sources on a Half-Space: A Unified Approach

The followings were assumed to develop a general solution for thermal spreading resistance of an arbitrary-shape heat source.

- The dimensions of heat sources and/or microcontacts are small compared with the distance separating them and with the dimensions of the body which heat spread through.
- For convenience, the temperature far from the contact area (heat source)is assumed to be zero with no loss of generality.

A.2 Analytic Determination of the Effective Thermal Conductivity of PEM Fuel Cell Gas Diffusion Layers

The followings were assumed to develop the geometrical, mechanical, and thermal models used to determine the through-plane effective thermal conductivity of GDLs.

- 3-D repeating basic cell consisting of uniformly sized equally spaced cylindrical fibers immersed in stagnant air.

- Elastic deformation of contacting fibers under compression.

- Steady state one-dimensional heat transfer.

- Negligible natural convection; justified by the Grashof number for a typical GDL with fiber diameter of $8.5\mu m$ which is in order of 10^{-6} and is significantly lower than 2500, the limit for natural convection [66].

- No radiation heat transfer. PEM fuel cells typically operate between 60 and $90°C$, and the contribution of radiation is small and can be neglected.

A.3 Experimental Study of the Effective Thermal Conductivity and Thermal Contact Resistance

The assumptions considered in the thermal conductivity and TCR measurements of metal foams and GDLs (both through-plane and in-plane), Appendices D-G, are described in the following.

- Equal TCR for the samples with different thicknesses but identical microstructural parameters under the same pressure.

- Negligible natural convection with the surrounding. The test column was insulated with glass wool in the experiments performed in the atmospheric air pressure to vanish the heat convection.

- Negligible natural convection; justified by the Grashof number for a typical GDL with fiber diameter of $8.5\mu m$ which is in order of 10^{-6} and is significantly lower than 2500, the limit for natural convection [66].

- Negligible radiation heat transfer; justified in Appendix H.

- One-dimensional heat conduction.

A.4 Effective Thermal Conductivity and Thermal Contact Resistance of Gas Diffusion Layers in PEM Fuel Cells. Part 1: Effects of Compressive Load

The following assumptions were applied to develop an analytical model for the through-plane thermal conductivity.

- The total thickness reduction under compression is the summation of elastic deformation and thickness variation as a result of fiber slippage.
- 3-D repeating basic cell consisting of uniformly sized equally spaced cylindrical fibers immersed in stagnant air.
- Elastic deformation of contacting fibers under compression.
- Steady state one-dimensional heat transfer.
- Negligible natural convection; justified by the Grashof number for a typical GDL with fiber diameter of $8.5 \mu m$ which is in order of 10^{-6} and is significantly lower than 2500, the limit for natural convection [66].
- No radiation heat transfer. PEM fuel cells typically operate between 60 and $90^{\circ}C$, and the contribution of radiation is small and can be neglected.

To develop an analytical approximation for the thermal contact resistance at the GDL-fluxmeter interface, the followings were assumed.

- fluxmeters have smooth surface; justified by the measured average roughness which is less than $1 \mu m$.
- Individual elastic contacts between the asperities originally higher than the separation of the surfaces.
- No conduction through the gas (air) at the interface corresponding to the vacuum condition.
- The carbon paper surface acts as a rough solid surface with the asperity radius equal to the average fiber radius.

A.5 Analytical Determination of the In-Plane Thermal Conductivity of Gas Diffusion Layers

The following assumptions were applied to model the random micro-structure of GDL and then develop an analytical model for the in-plane thermal conductivity.

- Random micro-structure divided into m equally-sized cells. Each cell consists of n fibers with an average radius of r, randomly oriented in the $x - y$ plane with an angle to the in plane heat flow direction and stacked vertically in z direction.

- The primary path for the heat conduction inside each cell is through the individual fibers. Heat transfer between the fibers in a cell is negligible due to large contact resistances.

- Heat flow is transferred from cell to cell through the junctions.

- Each fiber of two neighboring cells is in contact with two fibers from the top and bottom and carries heat from them.

- Considering the effect of binder and based on the in-plane SEM image showing contacts between fibers, the radius ratio of contact area to the fiber was assumed to be 0.1.

Appendix B

Thermal Spreading Resistance of Arbitrary-Shape Heat Sources on a Half-Space: A Unified Approach

Reproduced by permission of IEEE

Thermal Spreading Resistance of Arbitrary-Shape Heat Sources on a Half-Space: A Unified Approach

Ehsan Sadeghi, Majid Bahrami, and Ned Djilali

***Abstract*—Thermal spreading/constriction resistance is an important phenomenon where a heat source/sink is in contact with a body. Thermal spreading resistance associated with heat transfer through the mechanical contact of two bodies occurs in a wide range of applications. The real contact area forms typically a few percent of the nominal contact area. In practice, due to random nature of contacting surfaces, the actual shape of microcontacts is unknown; therefore, it is advantageous to have a model applicable to any arbitrary-shape heat source. Starting from a half-space representation of the heat transfer problem, a compact model is proposed based on the generalization of the analytical solution of the spreading resistance of an elliptical source on a half-space. Using a "bottom-up" approach, unified relations are found that allow accurate calculation of spreading resistance over a wide variety of heat source shapes under both isoflux and isothermal conditions.**

***Index Terms*—Elliptical heat source, half-space, spreading resistance, square root of area, superposition.**

NOMENCLATURE

A	Area (m^2).
a	Major semi-axis (m).
$B(\cdot,\cdot)$	Beta function.
b	Minor semi-axis (m).
$K(\cdot)$	Complete elliptic integral of the first kind (7).
k	Thermal conductivity (W/m $\cdot$ K).
$\mathcal{L}$	Characteristic length scale (m).
N	Number of sides of a regular polygon.
n	Geometric parameter for hyperellipse.
Q	Heat flow rate (W).
q	Heat flux (W/m^2).
R	Thermal spreading resistance (K/W).
$\overline{R}$	Average temperature based thermal spreading resistance (K/W).
R_0	Centroidal temperature based thermal spreading resistance (K/W).
R^*	Nondimensional spreading resistance.
R_T	Thermal spreading resistance, isothermal source (K/W).
r	Radius (m).
$\overline{T}$	Average temperature (K).
T_0	Centroidal temperature (K).

Greek Letters

α	Angle (rad).
β	Length ratio, b/a.
$\Gamma(\cdot)$	Gamma function.
ϵ	Aspect ratio.
η	Length, x_c/r.
ρ	Distance in polar coordinate (m).
ω	Angle (rad).

Subscript

c	Geometrical center of area.

I. INTRODUCTION

SPREADING resistance, also sometimes referred to as constriction resistance, is commonly encountered in thermal engineering whenever a concentrated heat source is in contact with a larger heat conducting surface. This phenomenon extends also to electric current and mass transfer problems. In this paper, we focus on thermal spreading resistance which often appears as a bottleneck in heat management, and is of relevance in applications such as integrated circuits and laser heating. In contacting bodies, real interaction between two surfaces occur only over microscopic contacts [1], [2]. The actual area of contact, i.e., the total area of all microcontacts, is typically less than 2% of the nominal contact area [1], [2]. Thus, heat flow is constricted and then spreads to pass from the contact area to contacting bodies. Thermal spreading resistance plays a vital role in the design of numerous thermal, electrical, and electronic devices and systems. Electronic equipment, aircraft structural joints, surface thermocouples, boundary lubrication, nuclear reactors, biomedical industries, and cryogenic liquid storage devices are only a few examples of such systems [3]–[7].

Assuming dimensions of microcontacts and/or heat sources are small compared with the distance separating them and with the dimensions of the body which heat spreads through, the heat source on a half-space hypothesis can be used [8]. As the microcontacts or heat sources increase in number and grow in size, a flux tube problem should be considered to account

Manuscript received March 13, 2008; revised November 7, 2008 and September 24, 2009. Date of current version June 9, 2010. This work was financially supported by the Natural Sciences and Engineering Research Council (NSERC) of Canada, discovery grant. Recommended for publication by Associate Editor K. Ramakrishna upon evaluation of reviewers' comments.

E. Sadeghi and N. Djilali are with the Department of Mechanical Engineering, University of Victoria, Victoria, BC V8W 2Y2, Canada (e-mail: ehsans@uvic.ca; ndjilali@me.uvic.ca).

M. Bahrami is with the School of Engineering, Simon Fraser University, Burnaby, BC V5A 1S6, Canada (e-mail: mbahrami@sfu.ca).

Digital Object Identifier 10.1109/TCAPT.2010.2043843

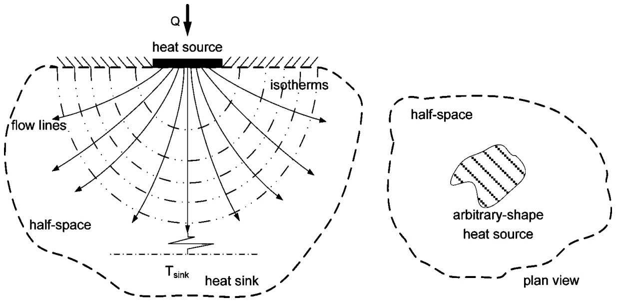

Fig. 1. Arbitrary-shape heat source on a half-space.

for the interference between neighboring microcontacts/heat sources. For an in-depth review of flux tube solutions for spreading resistance see [4], [9]–[11].

Several researchers including Kennedy [6], Ellison [12], Karmalkar *et al.* [13], and Pawlik [14] focused on analyzing thermal spreading resistance in electronic devices.

Yovanovich and his coworkers [15]–[18] investigated a range of steady-state and transient thermal spreading resistance. They proposed thermomechanical models for contact, gap, and joint resistances of joints formed by conforming rough surfaces, nonconforming smooth surfaces, and nonconforming rough surfaces [7]. Applying superposition techniques, Yovanovich developed a method to evaluate spreading resistance of different shapes on a half-space and derived found relationships for geometries including singly and doubly connected heat sources such as: hyperellipse, semicircle, triangle, polygon, and annulus. They also introduced the use of the square root of the source area $\sqrt{A}$ to nondimensionalize spreading resistance.

Analytical, experimental, and numerical models have been developed to predict thermal spreading resistance since the 1930s. Several hundred papers on thermal spreading resistance have been published which illustrates the importance of this topic.

In practice, due to the random nature of contacting surfaces, the actual shape of microcontacts is unknown; therefore, it would be beneficial to have a model applicable to any arbitrary-shape heat source. In spite of the rich body of literature on spreading resistance, there is yet no general model which can accurately estimate the spreading resistance of an arbitrary-shape heat source on a half-space due to the challenge of dealing with complex irregular geometries.

In this paper, a compact model is proposed based on the analytical solution of the spreading resistance of an elliptical source on a half-space. Using a "bottom-up" approach, it is shown that for a broad variety of heat source shapes, the proposed model is in agreement with the existing and/or developed analytical solutions.

II. PROBLEM STATEMENT

Consider steady-state heat transfer from an arbitrary-shape planar singly connected heat source on a half-space, Fig. 1. The temperature field within the half-space must satisfy Laplace's equation, $\nabla^2 T = 0$.

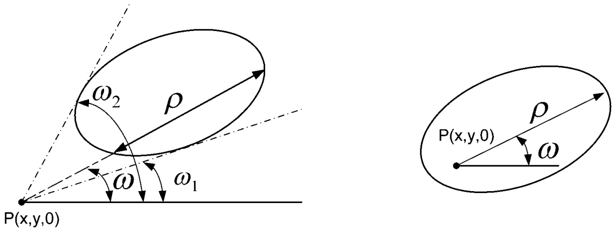

(a) (b)

Fig. 2. (a) Point outside the heat source. (b) Point inside the heat source.

Thermal spreading resistance R is defined as the difference between the temperature of heat source and the temperature of a heat sink far from it divided by the total heat flow rate through the contact area Q; i.e., $R = \Delta T/Q$ [19]. For convenience, the temperature far from the contact area may be assumed to be zero with no loss of generality, that is

$$R = \frac{T}{Q}. \tag{1}$$

To evaluate the spreading resistance, the temperature distribution of the heat source is required. Yovanovich [15] developed a relationship for the temperature distribution at each point of an isoflux heat source plane by using the integral and superposition techniques

$$T(x, y, 0) = \frac{q}{2\pi k} \int_0^{\omega} \rho(\omega) d\omega \tag{2}$$

where ρ and ω are shown in Fig. 2 for points outside and inside of the heat source area.

The reference temperature of heat sources is usually considered as the centroid or the average temperature. Substituting geometric center coordinates into (2), the centroid temperature can be found. For the average temperature, the temperature distribution is integrated over the heat source area

$$\overline{T} = \frac{1}{A} \int\int_A T(x, y, 0)\, dA. \tag{3}$$

For complicated shapes, the geometry is subdivided into simpler shapes; $T(x, y, 0)$ is then computed from (2) for each subdivided shape and the values are added up. Once the temperature is determined, the spreading resistance is obtained through (1).

To investigate the trend of different shapes and aspect ratios, it is more convenient to nondimensionalize spreading resistance in the form of $R^* = k\ \mathcal{L}\ R$, where k, $\mathcal{L}$, and R are the thermal conductivity of half-space, a characteristic length scale, and the spreading resistance, respectively [16]. Parameters required to define spreading resistance are: reference temperature, characteristic length scale, and boundary condition, (see Fig. 3). The reference temperature can be the centroid or average temperature of the source. According to Yovanovich [16], spreading resistance values for hyperelliptical sources vary over narrower bond when based on the centroidal temperature rather than when based on the average temperature. As shown later, there is a relationship

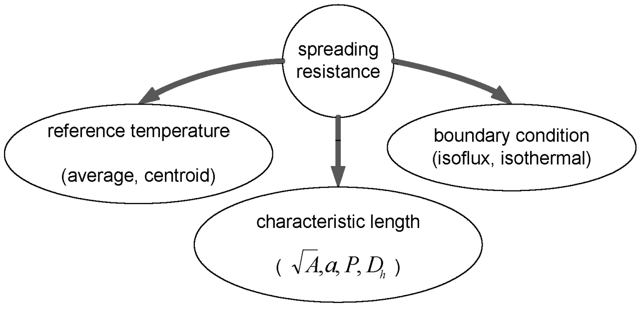

Fig. 3. Parameters involved in spreading resistance solution.

between the average and the centroid based resistances; for convenience, the average temperature is used as the reference temperature. After examining several possible length scales, we concluded that the square root of the square area $\sqrt{A}$ is the best choice of characteristic length scale, as Yovanovich proposed [16]. The next parameter is boundary condition; two boundary conditions are considered: 1) isothermal and 2) isoflux. The isoflux boundary condition is easier to apply and solve for. Furthermore, a relationship between these boundary conditions can be established.

III. CHARACTERISTIC LENGTH SCALE

To nondimensionalize the spreading resistance, a characteristic length scale is required. Different characteristic length scales are examined in this section. These include perimeter P, hydraulic diameter ($D_h = 4A/P$), an arbitrarily chosen dimension a, and the square root of the source area $\sqrt{A}$.

An analytical solution exists for hyperellipse shapes in the literature [16]. To compare different characteristic length scales, a hyperellipse source covering a wide variety of geometries is selected. A hyperellipse, in the first quadrant, is described by

$$y = b\left[1 - \left(\frac{x}{a}\right)^n\right]^{1/n} \tag{4}$$

where a and b are characteristic dimensions along the x and y axes, respectively, see Fig. 4. The effect of parameter n on the shape of the hyperellipse source is also shown in Fig. 4. When $n = 1$, the hyperellipse yields a rhombic source ($a > b$), or a square ($a = b$); for $n = 2$, the source is elliptical ($a > b$), or circular ($a = b$); $n > 3$, yields a rectangle ($a > b$) or a square ($a = b$) source with rounded corners; and for $n \to \infty$, the shape approaches a full rectangle/square source [16].

Yovanovich [16] calculated the spreading resistance for hyperelliptical sources. For instance, the nondimensional spreading resistance with $\sqrt{A}$ as the characteristic length scale is [16]

$$k\sqrt{A}R_0 = \frac{1}{\pi}\sqrt{\frac{\epsilon n}{B\left(\frac{n+1}{n}, \frac{1}{n}\right)}}\int_0^{\pi/2}\frac{d\omega}{[\sin^n \omega + \epsilon^n \cos^n \omega]^{1/n}} \tag{5}$$

where $B(\cdot)$ is the beta function.

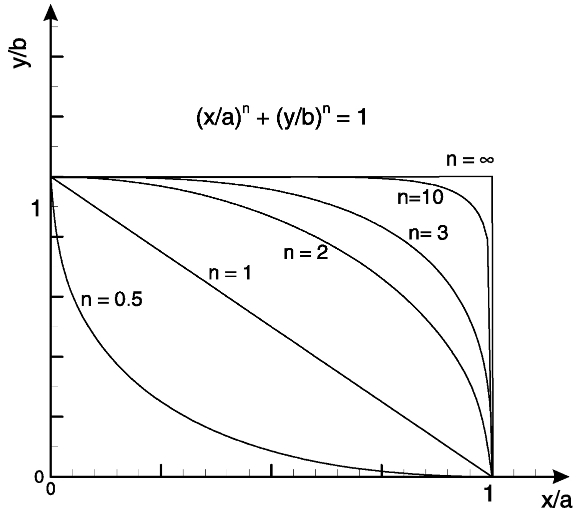

Fig. 4. Hyperellipse heat source in the first quadrant.

The analytic nondimensional spreading resistances R^* obtained using four different characteristic length scales are compared in Fig. 5(a)–(d) for both rectangular and elliptical sources. Comparing the trends for the different characteristic length scales, it can be concluded that the square root of area $\sqrt{A}$ is the superior choice for characteristic length scale. With this choice, the maximum difference between the analytical solutions of elliptical and rectangular sources is less than 6.8%; and in fact for $\epsilon > 0.4$, the difference is less than 1.5%. Since elliptical and rectangular sources, corresponding to (4) with $n = 2$ and $n \to \infty$, cover a wide range of shapes, it can be concluded that using $\sqrt{A}$ as a characteristic length scale, nondimensional spreading resistance of a hyperellipse with any value of $2 < n < \infty$ differ less than 6.8% with respect to an elliptical source. This implies that the effect of corners on the spreading resistance is not significant for hyperelliptical shapes with identical areas and aspect ratios. Since a hyperellipse covers a wide variety of shapes, the square root of area $\sqrt{A}$ is the most appropriate characteristic length scale for any arbitrary-shape heat source on a half-space, as Yovanovich suggested [16].

IV. PROPOSED MODEL

As shown previously, nondimensional spreading resistances of hyperelliptical sources with equal areas and aspect ratios are close for any value of $2 \leq n \leq \infty$. Thus, if we select one of these shapes in the model, the spreading resistance of the others can be predicted with good accuracy. The premise of the present model is that the solution for hyperelliptical source can be applied to estimate the spreading resistance of any shape of heat sources when the area and aspect ratio are the same as those of the hyperelliptical source. Since, the analytical solution of the elliptical source is more convenient, it is chosen as the basis of the model. Note that the isoflux rectangle could also be used as the basic model, but subsequent analysis has shown that the isoflux ellipse provides better overall agreement. According to the present model, an arbitrary-shape heat source is transformed to an elliptical shape where area and aspect ratio are maintained constant, (see Fig. 6). The

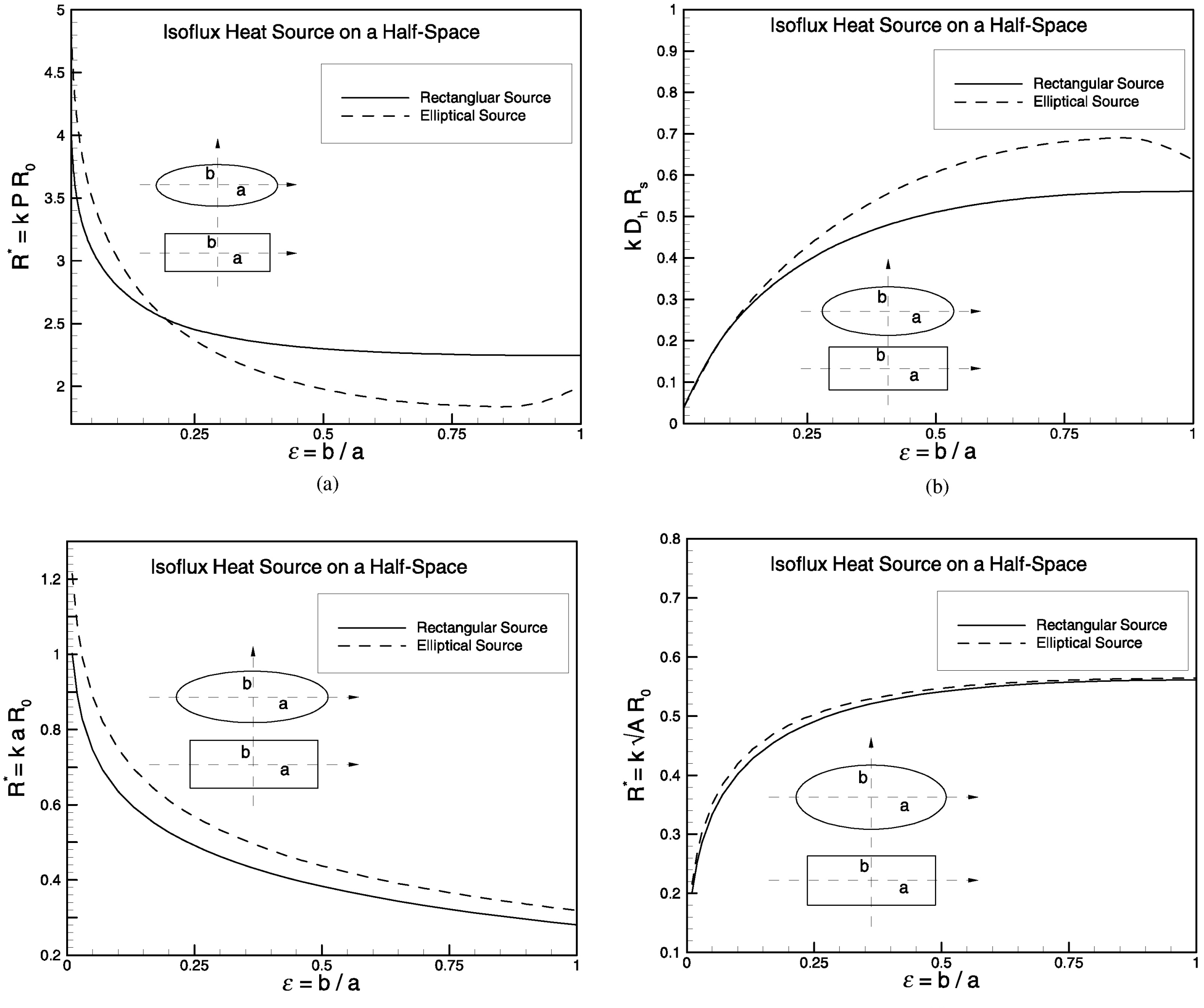

(a) (b)

(c) (d)

Fig. 5. Nondimensional spreading resistance of rectangular and elliptical sources with the characteristic lengths. (a) Perimeter P. (b) Hydraulic diameter D_h; (c) Major semi-axes a. (d) Square root of area $\sqrt{A}$.

analytical solution for the spreading resistance of an isoflux elliptical source on a half-space can be expressed using the general solution proposed by Yovanovich for a hyperellipse [15]

$$k\sqrt{A}R_0 = \frac{2}{\pi\sqrt{\pi}}\frac{K(1-\frac{1}{\epsilon^2})}{\sqrt{\epsilon}} \tag{6}$$

where $K(\cdot)$ is the complete elliptic integral of the first kind defined as

$$K\left(1-\frac{1}{\epsilon^2}\right) = \int_0^{\pi/2} \frac{dt}{\sqrt{\left[1-\left(1-\frac{1}{\epsilon^2}\right)\sin^2 t\right]}}. \tag{7}$$

There are a number of possible ways of defining the aspect ratio for arbitrary shapes, and in this paper the following is adopted

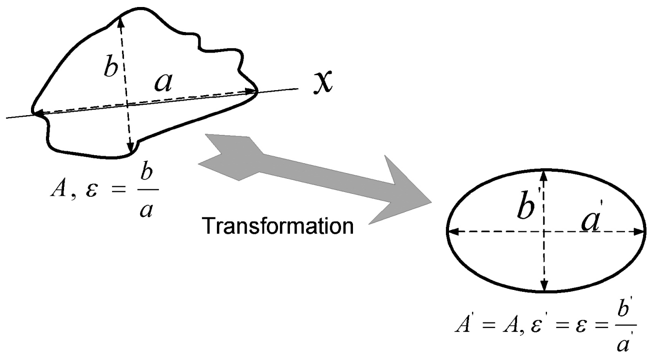

Fig. 6. Geometrical transformation of any arbitrary-shape heat source to elliptical source.

$$\epsilon = \frac{b}{a} \tag{8}$$

where a is the maximum length of the shape in arbitrary direction of x and b is the maximum length in the perpendicular

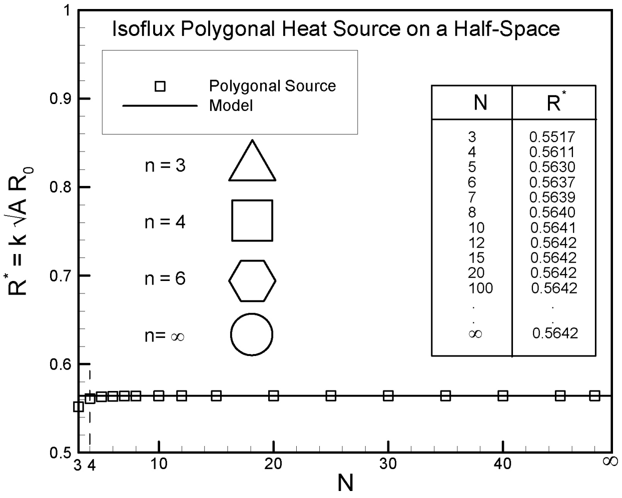

Fig. 7. Comparison of polygonal heat source with the model.

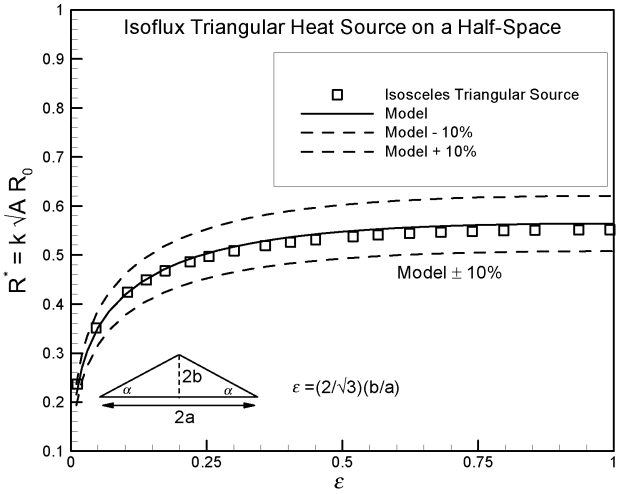

Fig. 8. Comparison of isosceles triangular heat source with the model.

direction to x as shown in Fig. 6. This definition, though not necessarily general, is appropriate for most of the shapes considered in this paper.

V. COMPARISON WITH ANALYTICAL SOLUTIONS

Using the superposition and integral methods proposed by Yovanovich [15], we find analytical solutions for spreading resistance of trapezoidal, rhombic, circular sector, circular segment, and rectangular source with semicircular or round ends as reported in the proceeding sections. In this section, the proposed model is compared with available and developed analytical solutions for a wide variety of isoflux heat sources on a half-space.

A. Polygonal Source

The analytical solution for a regular polygonal source with N sides can be written as [15]

$$k\sqrt{A}R_0 = \frac{1}{\pi}\sqrt{\frac{N}{\tan(\pi/N)}}\ln\frac{1+\sin(\pi/N)}{\cos(\pi/N)}. \tag{9}$$

Fig. 7 shows the effect of number of sides N on the nondimensional spreading resistance. There is not much difference between the different polygons, and for $N \geq 6$ the results are essentially the same. Also, the results are compared with the model for $\epsilon = 1$; the maximum difference between the analytical solution of polygonal sources and the model is less than 2.2%.

B. Triangular Source

The analytical solution for an isosceles triangular isoflux source developed by Yovanovich [15] is given by

$$k\sqrt{A}R_0 = \frac{\sqrt{2\beta}}{3\pi}\left[\ln\left[\tan\left(\frac{\pi}{4}+\frac{\omega_1}{2}\right)\right] + 2\sin(\cot^{-1}2\beta)\times \ln\left[\tan\left(\frac{\pi}{4}+\frac{\omega_2}{2}\right)\tan\left(\frac{\pi}{4}+\frac{\omega_3}{2}\right)\right]\right] \tag{10}$$

where $\omega_1 = \tan^{-1}(3/2\beta)$, $\omega_2 = \pi/2 - \cot^{-1}(2\beta)$, $\omega_3 = \pi - \omega_1 - \omega_2$, and $\beta = b/a$.

Choosing a proper aspect ratio is important. The aspect ratio for an equilateral triangle is unity; hence, the aspect ratio that also satisfies the equilateral case is $\epsilon = \beta(2/\sqrt{3})$. The spreading resistance for isosceles triangular source is compared with the model in Fig. 8. Results show good agreement with the model and maximum error is less than 2.2% when $\epsilon > 0.1$.

C. Rhombic Source

A rhombus is a special case of hyperellipse with $n = 1$. The spreading resistance for this shape can be evaluated from (5). A simpler method to calculate it, would be using the superposition technique. The nondimensional spreading resistance for a rhombic source can be written as

$$k\sqrt{A}R_0 = \frac{\sqrt{2}\sin(\omega_1)}{\pi\sqrt{\epsilon}}\ln[\tan(\frac{\pi}{4}+\frac{\omega_1}{2})\tan(\frac{\pi}{4}+\frac{\omega_2}{2})] \tag{11}$$

where $\omega_1 = \tan^{-1}\epsilon$, $\omega_2 = \pi/2 - \omega_1$, $A = 2ab$, and $\epsilon = b/a$.

Fig. 9 compares the rhombic heat source solution and the model, (6); except for small value of aspect ratio, $0 < \epsilon < 0.25$, the results agree with the model within 1.7%. The agreement for the lower aspect ratios is within 10%.

D. Trapezoidal Source

The trapezoidal cross-section is an important geometry which in the limit when the top side length goes to zero, yields an isosceles triangle. At the other limit when top and bottom sides are equal, it becomes a rectangle/square.

The spreading resistance for a trapezoidal source is found using superposition technique. The relationship for a trapezoidal source is unwieldy, and is therefore given in the appendix. The comparison of the results with the model for various trapezoidal sources is shown in Fig. 10; again there is good overall agreement with the model and the difference is less than 4% when $\epsilon > 0.1$.

E. Rectangular Source With Round Ends

Rectangular heat source with round ends is a combination of triangular and circular sector sources. Using superposition

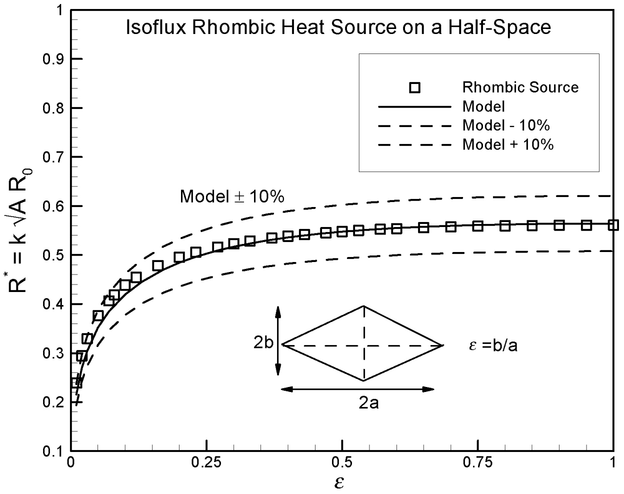

Fig. 9. Comparison of rhombic heat source with the model.

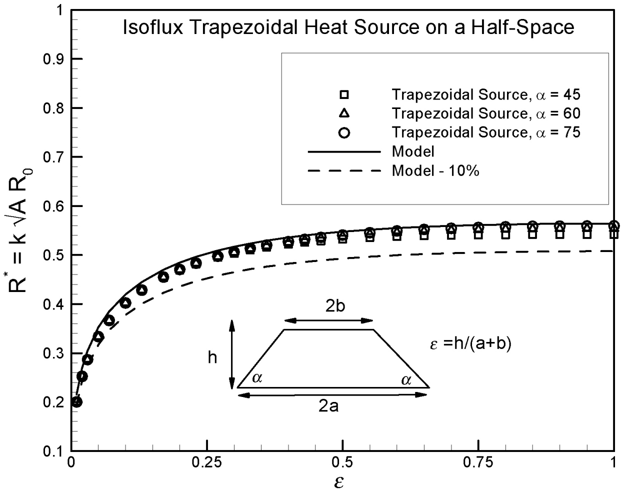

Fig. 10. Comparison of different trapezoidal heat sources with the model.

technique, the exact solution for this source is

$$k\sqrt{A}R_0=\frac{\sqrt{2}}{\pi}\,\frac{\beta\ln\left[\tan\left(\frac{\pi}{4}+\frac{\omega_1}{2}\right)\right]+\sqrt{1+\beta^2}\tan^{-1}\beta}{\sqrt{(1+\beta^2)\tan^{-1}\beta+\beta}} \tag{12}$$

where $\omega_1 = (\pi/2) - \tan^{-1}\beta$, $A = 2a^2[(1+\beta^2)\tan^{-1}\beta + \beta]$, $\beta = b/a$, and $\epsilon = \beta/\sqrt{1+\beta^2}$.

Fig. 11 shows the analytical solution compared with the model. It can be seen that the model can estimate the spreading resistance of this shapes with the maximum error of 2% where $\epsilon > 0.2$.

F. Rectangular Source With Semicircular Ends

Rectangular heat source with semicircular ends is a combination of triangular and circular segment sources. Using superposition technique, the exact solution for this source is

$$k\sqrt{A}R_0 = \frac{2}{\pi\sqrt{4\beta+\pi\beta^2}} \times \left[\beta\ln\left[\frac{\pi}{4}+\frac{\omega_1}{2}\right] + \int_0^{\alpha}\left(\cos\omega + \sqrt{\beta^2-\sin^2\omega}\right)d\omega\right] \tag{13}$$

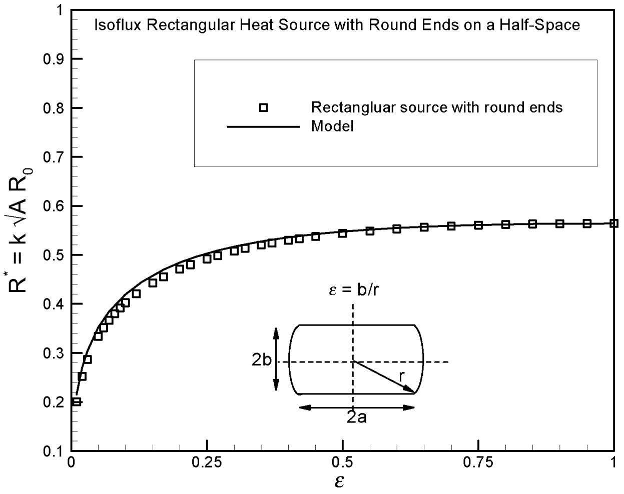

Fig. 11. Comparison of "rectangular heat source with round ends" with the model.

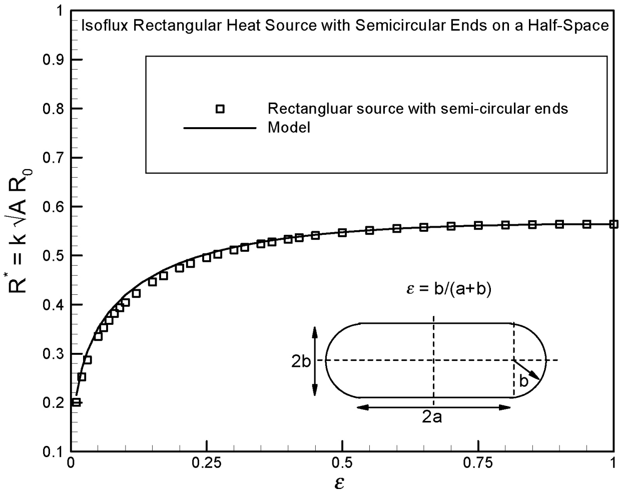

Fig. 12. Comparison of "rectangular heat source with semicircular ends" with the model.

where $\alpha = \tan^{-1}\beta$, $\omega_1 = (\pi/2) - \alpha$, $\beta = b/a$, $A = a^2[4\beta + \pi\beta^2]$, and $\epsilon = \beta/(1+\beta)$. Fig. 12 shows that the model can predict the spreading resistance for this shape with the maximum error of 2% where $\epsilon > 0.27$.

G. Circular Sector Source

Circular sector is composed of triangular and noncircular sector sources with the common vertex at the centroid. Using superposition, the exact solution can be written as

$$k\sqrt{A}R_0 = \frac{1}{\pi\sqrt{\alpha}}\left[\eta\sin\alpha\ln\left[\tan\left(\frac{\pi}{4}+\frac{\omega_1}{2}\right)\tan\left(\frac{\pi}{4}+\frac{\omega_2}{2}\right)\right] + \int_0^{\omega_3}\left(\sqrt{1-\eta^2\sin^2\omega} - \eta\cos\omega\right)d\omega\right] \tag{14}$$

where $\eta = x_c/r = 2\sin\alpha/3\alpha$, $\omega_1 = \pi/2 - \alpha$, $\omega_2 = \tan^{-1}\left[(1-\eta\cos\alpha)/(\eta\sin\alpha)\right]$, $\omega_3 = \pi - \omega_1 - \omega_2$. The aspect ratio is defined as the ratio of maximum lengths in y and x directions, i.e., $\epsilon = 2r\sin\alpha/r = 2\sin\alpha$.

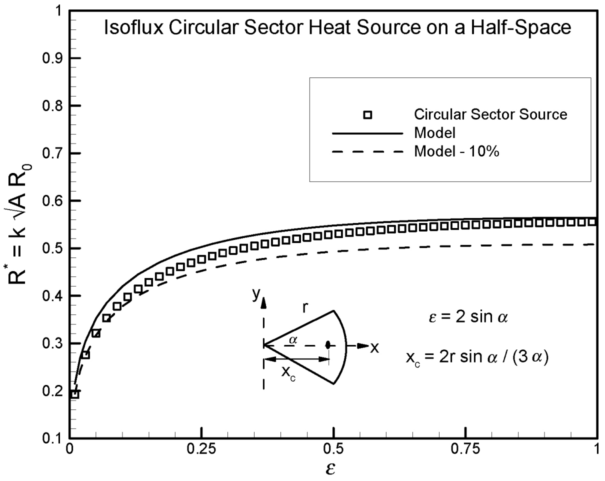

Fig. 13. Comparison of circular sector heat source with the model.

The relationship developed for the circular sector source is compared with the model in Fig. 13. Note that since η and ω_1 are functions of α only, and since $\alpha = \sin^{-1}(\epsilon/2)$, (14) can be plotted as a function of ϵ only. It can be observed that for small values of aspect ratios, the error is more than 5%, but for $\epsilon > 0.27$ the error becomes less than 5%.

H. Circular Segment Source

A circular segment can be presented as a combination of right angle triangles and noncircular sector sources with the common vertex at the geometric center. Applying (2) and using superposition technique, the exact solution for the spreading resistance can be found

$$k\sqrt{A}R_0 = \frac{1}{\pi\sqrt{\alpha - \frac{\sin 2\alpha}{2}}}\left[(\eta - \cos\alpha)\ln\left[\tan\left(\frac{\pi}{4} + \frac{\omega_1}{2}\right)\right] + \int_0^{\omega_2}\left(\sqrt{1 - \eta^2\sin^2\omega} - \eta\cos\omega\right)d\omega\right] \quad (15)$$

where $x_c = \frac{(r/3)(2\sin\alpha - \cos\alpha\sin 2\alpha}{\alpha - \sin(2\alpha)/2}$, $\eta = x_c/r$, $\omega_1 = \tan^{-1}\left[\sin\alpha/(\eta - \cos\alpha)\right]$, and $\omega_2 = \pi - \omega_1$. The aspect ratio is defined as the ratio of maximum lengths in y and x directions. For different value of α, the aspect ratio becomes

$$\epsilon = \begin{cases} \dfrac{1 - \cos\alpha}{2\sin\alpha}, & \alpha \le \dfrac{\pi}{2} \\ \dfrac{1 - \cos\alpha}{2}, & \dfrac{\pi}{2} \le \alpha \le \pi. \end{cases} \quad (16)$$

The exact solution of the circular segment source is compared with the model in Fig. 14. The results show good agreements with the model over the entire range of aspect ratio.

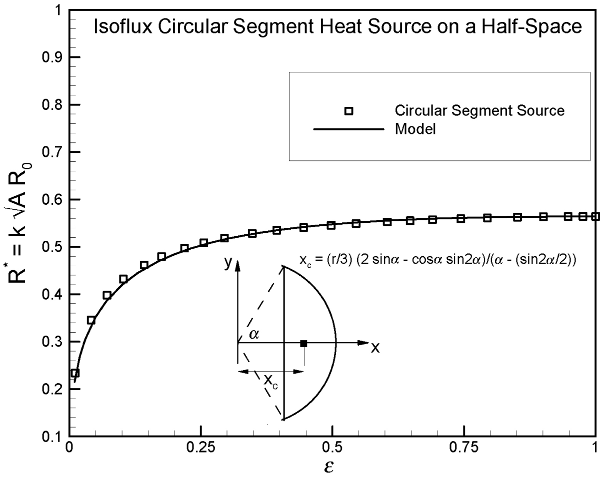

Fig. 14. Comparison of circular segment heat source with the model.

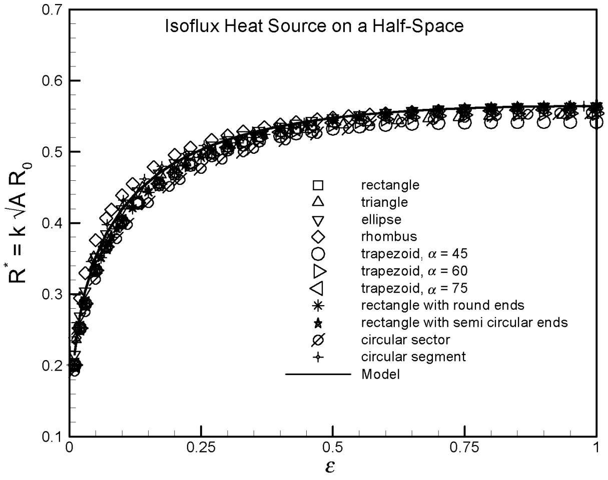

Fig. 15. Comparison of arbitrary-shape heat sources with the model.

The examined geometries of a heat source on a half-space are compared with the model in Table I and Fig. 15. The definition of aspect ratio, proper criteria to use the model, and the maximum relative error with respect to the model is reported in Table I. The maximum error occurs in small values of aspect ratio, $\epsilon \le 0.01$; if aspect ratio is greater than 0.1 the error decreases sharply. As seen in Table I and Fig. 15, the model shows good agreement with the analytical solutions for wide variety of shapes, especially when $\epsilon > 0.1$.

VI. REFERENCE TEMPERATURE

Having established the accuracy of the proposed model provides for the centroidal temperature based spreading resistance of any arbitrary-shape isoflux heat source on a half-space, we turn our attention to developing a relationship between the centroid temperature and average temperature based spreading resistances. The latter is a commonly used reference and can also be applied to doubly-connected regions.

There is no analytical solution for the isothermal elliptical source in the literature, therefore, this problem was solved numerically in this paper. The results show that the ratio of nondimensional spreading resistances based on the average and centroid temperatures for elliptical source varies only

TABLE I

COMPARISON AND ACCURACY OF PROPOSED SPREADING RESISTANCE MODEL FOR VARIOUS GEOMETRIES

cross-section	ϵ	notes	max error
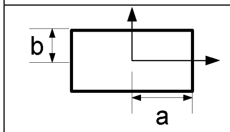	$\frac{b}{a}$	maximum difference of 2% for $\epsilon > 0.3$	6.8%
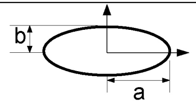	$\frac{b}{a}$	base model	–
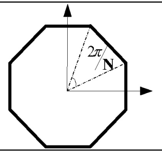	1	very close agreement with the model specially for $N > 6$	2.2%
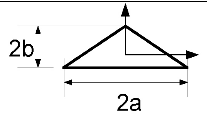	$\frac{2\beta^{[1]}}{\sqrt{3}}$	maximum difference of 2.2% for $\epsilon > 0.1$	4.8%
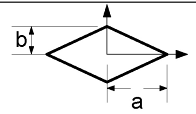	$\frac{b}{a}$	maximum difference of 1.7% for $\epsilon > 0.25$	11%
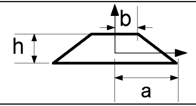	$\frac{h}{a+b}$	2.6% < difference < 4% for $\epsilon > 0.1$	6.8%
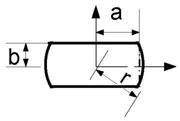	$\frac{\beta}{\sqrt{1+\beta^2}}$	maximum difference of 2% for $\epsilon > 0.2$	6.8%
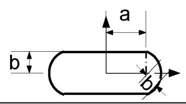	$\frac{\beta}{1+\beta}$	maximum difference of 2% for $\epsilon > 0.27$	6.8%
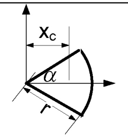	$2\sin\alpha$	maximum difference of 5% $\epsilon > 0.27$	10.8%
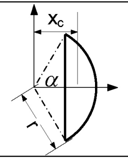	$\frac{1-\cos\alpha}{2\sin\alpha} \; :\alpha \le \frac{\pi}{2}$ $\frac{1-\cos\alpha}{2} \; :\frac{\pi}{2} \le \alpha$	maximum difference of 2% for $\epsilon > 0.13$	4.6%

[1] $\beta = b/a$

between 0.8485 and 0.8491; therefore; it remains approximately constant with an average value of 0.849

$$\frac{k\sqrt{A}\bar{R}}{k\sqrt{A}R_0} = \frac{\bar{R}}{R_0} \cong 0.849. \tag{17}$$

Yovanovich *et al.* [16], [17] already established this result for some specific shapes; the analysis presented here shows that in fact this is generally valid for a wide range of geometries. The nondimensional spreading resistance based on the average temperature for elliptical and rectangular sources is shown in Fig. 16. The predicted resistances are indeed very close. Since the ellipse and rectangle are the lower and the upper bounds for the hyperellipse within $2 \le n \le \infty$, it can be concluded that the elliptical source result for nondimensional spreading resistance based on the average temperature can be used for hyperelliptical source within $2 \le n \le \infty$. Also, (17) provides an excellent estimate of the ratio $\bar{R}/R_0$.

Since the model provides a good estimate for centroidal temperature based spreading resistance, and (17) is approximately valid for hyperelliptical shapes covering a wide variety of geometries, (17) can be used with confidence to predict the ratio of spreading resistance based on the average and centroid temperatures for a broad variety of heat source shapes. Thus, combining (6) and (17), the model for the average temperature

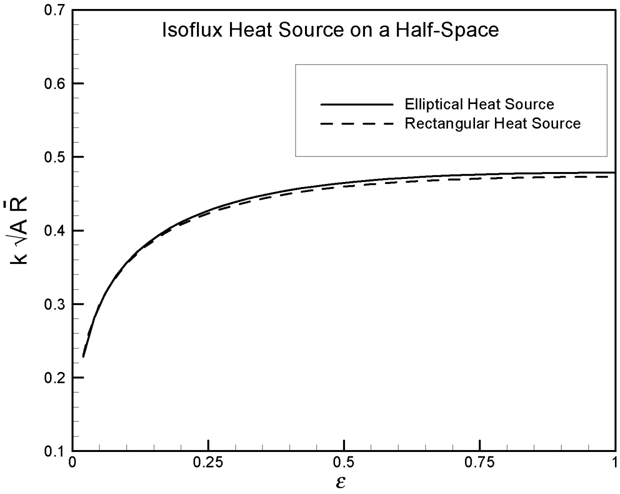

Fig. 16. Comparison of average temperature based spreading resistances for elliptical and rectangular heat sources.

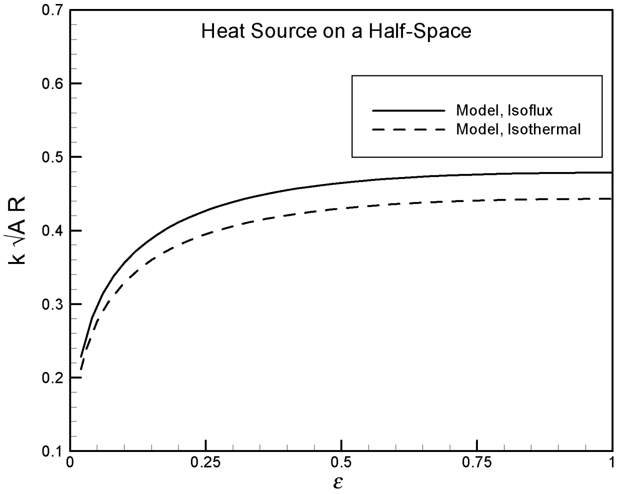

Fig. 17. Proposed model for isothermal and isoflux boundary conditions.

based spreading resistance reads

$$k\sqrt{A}\bar{R} = \frac{1.6974}{\pi\sqrt{\pi}} \frac{K(1-\frac{1}{\epsilon^2})}{\sqrt{\epsilon}}. \tag{18}$$

VII. BOUNDARY CONDITION

We have so far considered spreading resistance for any isoflux arbitrary-shape heat source on a half-space. Yovanovich [18] developed an analytical solution for an isothermal elliptical source

$$k\sqrt{A}R_T = \frac{\sqrt{\epsilon}}{2\sqrt{\pi}} K(1-\epsilon^2). \tag{19}$$

Schneider [20] numerically solved Laplace's equation for the rectangular source and reported a correlation if the form of

$$k\sqrt{A}R_T = \frac{1}{\sqrt{\epsilon}}\left[0.06588 - \frac{0.00232}{\epsilon} + \frac{0.6786}{(1/\epsilon)+0.8145}\right]$$
$$: 0.25 \le \epsilon \le 1. \tag{20}$$

A comparison between the solutions of isothermal rectangular and elliptical sources indicates a maximum difference of 1.27% which occurs at $\epsilon = 1$, while the solutions are essentially identical for an aspect ratio ϵ less than 0.4. Since the isoflux elliptical source which is proposed as the model predicts accurately spreading resistance of any isoflux arbitrary-shape heat source, this suggests that the solution for isothermal elliptical source can be used for a wide variety of isothermal heat sources. Thus, the general form of the model for any arbitrary-shape heat source on a half-space can be expressed as

$$k\sqrt{A}R = \begin{cases} \dfrac{1.6974}{\pi\sqrt{\pi}} \dfrac{K(1-\frac{1}{\epsilon^2})}{\sqrt{\epsilon}}, & \text{isoflux (average temp.)} \\ \frac{\sqrt{\epsilon}}{2\sqrt{\pi}} K(1-\epsilon^2), & \text{isothermal.} \end{cases} \tag{21}$$

Fig. 17 presents the spreading resistance for isothermal and isoflux boundary conditions calculated using (21). The ratio of isothermal to isoflux spreading resistance does not change much and remains approximately constant at 0.925 with $R_{\text{isothermal}}/R_{\text{isoflux}} \approxeq 0.925 \pm 0.0005$. In practice, the boundary condition is a combination of isoflux and isothermal conditions and these provide two bounds for actual thermal spreading resistances.

VIII. SUMMARY AND CONCLUSION

Thermal spreading resistance is an important major phenomenon in thermal engineering problems, whenever temperature and cross-sectional area variations exist. In this paper, a model based on the generalization of the analytical solution of isoflux elliptical source has been proposed, and analytic solutions were obtained for a variety of complex shapes. The generalized model presented here provides a unified approach for calculating the spreading resistance for a large variety of geometries, and under both isoflux and isothermal conditions. The highlights of the model and results are as follows.

1) The most appropriate characteristic length scale for nondimensional spreading resistance is square root of area $\sqrt{A}$.
2) The spreading resistance for arbitrarily singly connected shapes agrees with the proposed model.
3) The ratio of isothermal to isoflux spreading resistance is approximately 0.931 for a wide range of shapes for different aspect ratios.

APPENDIX

ISOSCELES TRAPEZOIDAL SOURCE

The spreading resistance for an isosceles trapezoidal source is found using superposition technique. Considering the parameters shown in Fig. 18, the nondimensional spreading resistance based on the centroidal temperature is found as

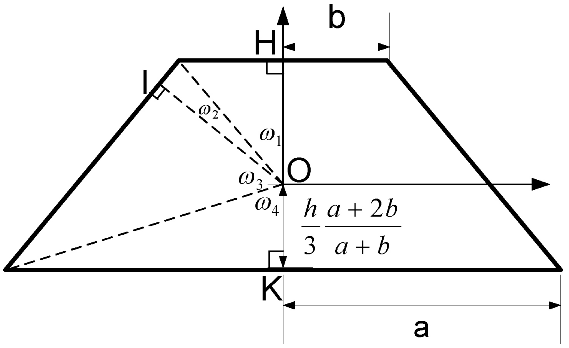

Fig. 18. Cross-section of an isosceles trapezoidal heat source.

$$k\sqrt{A}R_0 = \frac{1}{\pi}\frac{\overline{OI}\,(\Omega_2+\Omega_3)+\overline{OH}\Omega_1+\overline{OK}\Omega_4}{\sqrt{A}} \tag{22}$$

where $\Omega_i = \ln[\tan((\pi/4)+(\omega_i/2))]$. For $\theta > 90$, Ω_2 and ω_2 must be replaced by $-\Omega_2$ and $-\omega_2$, respectively.

REFERENCES

[1] J. A. Greenwood and B. P. Williamson, "Contact of nominally flat surfaces," *Proc. R. Soc. Lond. Ser. A, Math. Phys. Sci.*, vol. 295, pp. 300–319, Dec. 1966.

[2] D. Tabor, *The Hardness of Metals*. London, U.K.: Oxford Univ. Press, 1951, ch. 1.

[3] A. K. Das and S. S. Sadhal, "Thermal constriction resistance between two solids for random distribution of contacts," *Heat Mass Transfer*, vol. 35, no. 2, pp. 101–111, Jul. 1999.

[4] A. A. Rostami, A. Y. Hassan, and P. C. Lim, "Parametric study of thermal constriction resistance," *Heat Mass Transfer*, vol. 37, no. 1, pp. 5–10, Jan. 2001.

[5] Y. Muzychka, M. Yovanovich, and J. Culham, "Application of thermal spreading resistance in compound and orthotropic systems," in *Proc. Am. Inst. Aeronaut. Astronaut. (AIAA) 39th Aerospace Sci. Meeting Exhibit*, Reno, NV, Jan. 2001, p. 0366.

[6] D. P. Kennedy, "Spreading resistance in cylindrical semiconductor devices," *J. Appl. Phys.*, vol. 31, pp. 1490–1497, Aug. 1960.

[7] M. M. Yovanovich, "Four decades of research on thermal contact, gap, and joint resistance in microelectronics," *IEEE Trans. Compon. Packag. Technol.*, vol. 28, no. 2, pp. 182–206, Jun. 2005.

[8] A. M. Clausing and B. T. Chao, "Thermal contact resistance in a vacuum environment," *J. Heat Transfer Trans. ASME*, vol. 87, no. 2, pp. 243–251, 1965.

[9] B. B. Mikic, "Thermal contact conductance; Theoretical considerations," *Int. J. Heat Mass Transfer*, vol. 17, no. 2, pp. 205–214, 1974.

[10] M. G. Cooper, B. B. Mikic, and M. M. Yovanovich, "Thermal contact conductance," *Int. J. Heat Mass Transfer*, vol. 12, pp. 279–300, Jan. 1969.

[11] Y. S. Muzychka, M. M. Yovanovich, and J. R. Culham, "Thermal spreading resistance of eccentric heat sources on rectangular flux channels," *ASME J. Electron. Packag.*, vol. 125, no. 2, pp. 178–185, 2003.

[12] G. N. Ellison, "Maximum thermal spreading resistance for rectangular sources and plates with nonunity aspect ratios," *IEEE Trans. Compon. Packag. Technol.*, vol. 26, no. 2, pp. 439–454, Jun. 2003.

[13] S. Karmalkar, P. V. Mohan, H. P. Nair, and R. Yeluri, "Compact models of spreading resistances for electrical/thermal design of devices and ICs," *IEEE Trans. Electr. Devices*, vol. 54, no. 7, pp. 1734–1743, Jul. 2007.

[14] M. Pawlik, "Spreading resistance: A quantitative tool for process control and development," *Vacuum Sci. Technol. B: Microelectr. Nanometer Struct.*, vol. 10, pp. 388–396, Jan. 1992.

[15] M. M. Yovanovich, "Thermal constriction resistance of contacts on a half-space: Integral formulation," *Progress Astronaut. Aeronaut.: Radiative Transfer Thermal Control*, vol. 49, pp. 397–418, 1976.

[16] M. M. Yovanovich, S. S. Burde, and J. C. Thompson, "Thermal constriction resistance of arbitrary planar contacts with constant flux," *Progress Astronaut. Aeronaut.: Thermophys. Spacecraft Outer Planet Entry Probes*, vol. 56, pp. 127–139, 1976.

[17] M. M. Yovanovich and S. S. Burde, "Centroidal and area average resistances of nonsymmetric, singly connected contacts," *AIAA J.*, vol. 15, pp. 1523–1525, Oct. 1977.

[18] M. M. Yovanovich, "Thermal constriction resistance between contacting metallic paraboloids: Application to instrument bearings," *Progress Astronaut. Aeronaut.: Fundam. Spacecraft Thermal Design*, vol. 24, pp. 337–358, 1971.

[19] H. S. Carslaw and J. C. Jaeger, *Conduction of Heat in Solids*, 2nd ed. London, U.K.: Oxford Univ. Press, 1959, ch. 3.

[20] G. E. Schneider, "Thermal resistance due to arbitrary dirichlet contacts on a half-space," *Prog. Astronaut. Aeronaut. Thermophys. Therm. Control*, vol. 65, pp. 103–119, 1978.

Ehsan Sadeghi received the B.A.Sc. and M.A.Sc. degrees in mechanical engineering from Sharif University of Technology, Tehran, Iran. He is currently working toward the Ph.D. degree from the Department of Mechanical Engineering, University of Victoria, Victoria, BC, Canada. For the Ph.D. degree, he has been working on the analytical and experimental investigations of transport phenomena in high porosity materials including metal foams, and gas diffusion layers used in fuel cells.

His other research interests include contact mechanics, renewable energy, microscale heat transfer, microfluidics, and microelectronics cooling.

Mr. Sadeghi is a Member of the Institute for Integrated Energy Systems and the Multiscale Thermofluidic Laboratory for Sustainable Energy Research.

Majid Bahrami received the B.A.Sc. degree in mechanical engineering from Sharif University of Technology, Tehran, Iran, in 1992, the M.A.Sc. degree in gas-solid flow in circulating fluidized beds from Amir Kabir University of Technology (Tehran Polytechnic), Tehran, Iran, in 1995, and the Ph.D. degree in thermal joint resistance of contacting rough surfaces from the Department of Mechanical Engineering, University of Waterloo, Ontario, Canada, in 2004.

From 1995 to 2000, he practiced in heating, ventilating, air conditioning, and refrigeration industry as a Thermal Engineer and Consultant. From 2004 to 2006, he was a Post-Doctoral Fellow and an Instructor with the Microelectronics Heat Transfer Laboratory, Waterloo, Ontario, Canada, where he made major contributions in the field of heat transfer, microfluidics, and microelectronics cooling. From 2006 to 2008, he was an Assistant Professor with the Department of Mechanical Engineering, University of Victoria, Victoria, BC, Canada. Since 2008, he has been an Assistant Professor with the School of Engineering, Simon Fraser University, BC, Canada. He has numerous publications in refereed journals and conferences. His current research interests include modeling and characterization of transport phenomena in micro/nano-structured materials and porous media, heat transfer in microchannels and microfluidics, conversion and storage of sustainable energy, contact mechanics and thermal interfaces, and microelectronics cooling.

He is a Member of the American Society of Mechanical Engineers, the American Institute of Aeronautics and Astronautics, and the Canadian Society for Mechanical Engineering.

Ned Djilali received a B.S. (Hons.) in aeronautical engineering from the University of Hertfordshire, Herts, U.K., the M.S. degree in aeronautics and fluid mechanics from Imperial College, London, U.K., and the Ph.D. degree in mechanical engineering from the University of British Columbia, Vancouver, BC, Canada.

He is the Canada Research Chair in Energy Systems Design and Computational Modeling and a Professor of Mechanical Engineering with the Department of Mechanical Engineering, University of Victoria, Victoria, BC, Canada. He has served as the Director of the Institute for Integrated Energy Systems from 2001 to 2007, promoting interdisciplinary research across science and technology, economics and policy. Prior to joining the University of Victoria in 1991, he was an Aerodynamicist with the

Canadair Aerospace Division, Bombardier, Inc., Montreal, from 1989 to 1991. He has published over 100 peer reviewed journal papers, and holds several patents and research awards. His current research and teaching interests include transport phenomena and sustainable energy systems, with a focus on fuel cell technology, hydrogen systems safety, and integration of renewable energy. Much of his research is in collaboration with leading fuel cell companies in North America and Japan.

Dr. Djilali is a Fellow of the Canadian Academy of Engineering.

Appendix C

Analytic Determination of the Effective Thermal Conductivity of PEM Fuel Cell Gas Diffusion Layers

Reproduced by permission of Elsevier

Available online at www.sciencedirect.com

ScienceDirect

Journal of Power Sources 179 (2008) 200–208

JOURNAL OF POWER SOURCES

www.elsevier.com/locate/jpowsour

Analytic determination of the effective thermal conductivity of PEM fuel cell gas diffusion layers

E. Sadeghi *, M. Bahrami, N. Djilali

Department of Mechanical Engineering and the Institute for Integrated Energy Systems,
University of Victoria, Victoria, BC V8W 3P6, Canada

Received 10 October 2007; received in revised form 14 December 2007; accepted 18 December 2007
Available online 26 December 2007

Abstract

Accurate information on the temperature field and associated heat transfer rates are particularly important in devising appropriate heat and water management strategies in proton exchange membrane (PEM) fuel cells. An important parameter in fuel cell performance analysis is the effective thermal conductivity of the gas diffusion layer (GDL). Estimation of the effective thermal conductivity is complicated because of the random nature of the GDL micro structure. In the present study, a compact analytical model for evaluating the effective thermal conductivity of fibrous GDLs is developed. The model accounts for conduction in both the solid fibrous matrix and in the gas phase; the spreading resistance associated with the contact area between overlapping fibers; gas rarefaction effects in microgaps; and salient geometric and mechanical features including fiber orientation and compressive forces due to cell/stack clamping. The model predictions are in good agreement with existing experimental data over a wide range of porosities. Parametric studies are performed using the proposed model to investigate the effect of bipolar plate pressure, aspect ratio, fiber diameter, fiber angle, and operating temperature.

Keywords: Porous media; Gas diffusion layer; PEM fuel cell; Spreading resistance; Effective thermal conductivity

1. Introduction

Electrochemical energy conversion in hydrogen fuel cells is an exothermic process that results in significant temperature variations [1,2]. Accurate information on the temperature field and associated heat transfer rates are particularly important in devising appropriate heat and water management strategies in proton exchange membrane (PEM) fuel cells, as the temperature field affects relative humidity, membrane water content, and reaction kinetics, as well as durability. One of the main fuel cell components in this respect is the porous gas transport layer, commonly referred to as the gas diffusion layer (GDL). GDLs employed in PEM fuel cells typically consist of a fibrous structure in the form of a thin “paper” or “woven cloth”, see Fig. 1. The GDL provides five key functions for a PEM fuel cell: (1) mechanical support, (2) electronic conductivity, (3) heat removal, (4) reactant access to catalyst layers, and (5) product removal [3].

The porous nature of GDL micro structure, makes it necessary to define an effective thermal conductivity, a transport parameter that plays an important role in fuel cell performance analysis [4] and that is required in computational models [5]. In addition to being porous, GDLs are anisotropic, which adds to the complexity of characterizing the effective thermal conductivity.

Ramousse et al. [4] recently investigated the effective thermal conductivity of non-woven carbon felt GDLs and estimated the conductivity bounds using a model connecting the two phases (solid and gas) in series or parallel. The model as well as their experimental measurements yielded conductivity values that are at least one order of magnitude lower than most values reported in the literature. Ramousse et al. [4] also noted that due to contact and constriction resistances between carbon fibers, the effective thermal conductivity of carbon felts are much lower than pure

---

* Correspondingauthor. Tel.: +1 250 813 3125; fax: +1 250 721 6051.
E-mail addresses: ehsans@uvic.ca (E. Sadeghi), mbahrami@uvic.ca (M. Bahrami), ndjilali@uvic.ca (N. Djilali).

0378-7753/$ – see front matter © 2007 Elsevier B.V. All rights reserved.
doi:10.1016/j.jpowsour.2007.12.058

Nomenclature

A	area (m^2)
a, b	major and minor semi axes of elliptical contact area (m)
d	fiber diameter (m)
E	Young's modulus (Pa)
E'	effective elastic modulus (Pa)
F	contact load (N)
F_1	integral function of $(\rho' \rho''^{-1})$, Eq. (8)
GDL	gas diffusion layer
$K(\cdot)$	complete elliptic integral of the first kind
k	thermal conductivity (Wm^{-1} K^{-1})
k_{eff}	effective thermal conductivity (Wm^{-1} K^{-1})
k_{eff_0}	effective thermal conductivity of the reference basic cell (Wm^{-1} K^{-1})
k^*	non-dimensional effective thermal conductivity, $k_{\text{eff}}\, k_{\text{eff}_0}^{-1}$
l	distance between two adjacent fibers in x-direction (Fig. 3) (m)
P_{BP}	bipolar pressure (Pa)
P_{g}	gas pressure (Pa)
P_{GDL}	GDL pressure (Pa)
Pr	Prandtl number (–)
Q_{gc}	heat transfer rate through gas filled gap (W)
R	thermal resistance (KW^{-1})
R_{co}	constriction resistance (KW^{-1})
R_{sp}	spreading resistance (KW^{-1})
T	temperature (K)
V_{s}	fiber (solid) volume of basic cell (m^3)
V_{tot}	total volume of basic cell (m^3)
w	distance between two adjacent fibers in the y-direction (Fig. 3) (m)

Greek

α	thermal accommodation parameter
β	fluid property parameter, Eq. (17)
$\delta(x)$	local gap thickness (m)
ε	porosity (–)
η	modulus of elliptic integral (–)
γ	heat capacity ratio (–)
Λ	mean free path of gas molecules (m)
λ	ratio of relative radii of curvature $(\rho' \rho''^{-1})$
μ	ratio of molecular weights of the gas and the solid, $M_{\text{g}}\, M_{\text{s}}^{-1}$
θ	angle between two fibers (rad)
ρ', ρ''	major and minor relative radii of curvature (m)
ρ'_1, ρ'_2	principal radii of curvature (m)
ρ_{e}	equivalent radius of curvature of the contacting surfaces (m)
υ	Poisson's ratio (–)
ξ	aspect ratio (wl^{-1})

Subscripts

0	reference state
1	bottom block of the basic cell
2	top block of the basic cell
∞	standard condition state
c	contact plane
g	gas
gc	gas filled gap
max	maximum value
s	solid (carbon fiber)
t	upper boundary of the top block
tot	total value

carbon, and used Danes and Bardon [6] correlation to estimate the effective thermal conductivity of the solid phase.

Khandelwal and Mench [7] measured the through-plane thermal conductivity of GDLs. They examined two different types of commercial GDLs with a variety of thickness and porosity. They studied the effect of temperature and polytetrafluoro ethylene (PTFE) content on the effective thermal conductivity, and obtained values in close agreement with the manufacturer data sheet. The experimental data reported in the literature for effective thermal conductivity spans a wide range of values, 0.1–1.6 Wm^{-1} K^{-1}, and there is clearly need to better understand of the possible sources of inconsistency [1,4].

Our literature review indicates the need for a general model that can accurately predict the effective thermal conductivity of GDL, and its trends as parameters varied, since no reliable correlations are available and there is lack of data and understanding on the effect of geometric parameters such as tortuosity, radius of contact area between fibers, and angle between fibers. The objectives of the present work are:

- Develop and verify a comprehensive analytical model that can predict the effective thermal conductivity of GDLs and that captures accurately the trends observed in experimental data.
- Investigate the effect of relevant geometrical, thermal, and mechanical parameters involved and identify the controlling parameters.

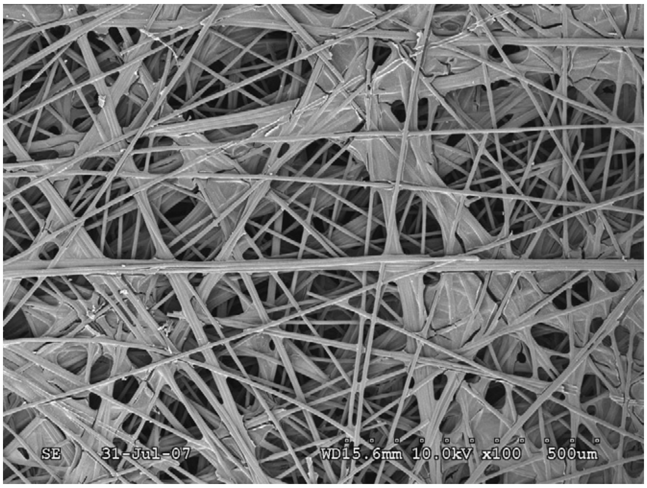

Fig. 1. SEM image of a Toray GDL.

Following the approach used successfully in several applications such as spherical packed beds by Bahrami et al. [8], a “basic cell” is taken to represent the fibrous media, i.e. the structure is assumed to be repeated throughout the GDL. Each cell is made up of contact regions. A contact region is composed of a contact area between two portions of fibers, surrounded by a gas (air) layer. A thermal resistance model is then constructed taking into account the basic conduction processes through both the solid fibrous matrix and the gas phase as well as important phenomena including spreading resistance associated with the contact area between overlapping fibers and gas rarefaction effects in microgaps.

The basic cell approach breaks the problem into distinct conduction paths, the contact between two fibers, the gas layer between fibers; and calculates the conductivity of the medium as a series/parallel combination of the individual resistances for those paths. The advantage of this approach is that it readily allows evaluation of the relative contributions of each conduction path as a function of the medium properties [8].

The scheme of the present approach to evaluate the effective thermal conductivity is shown in Fig. 2. The first step in estimating the effective thermal conductivity is the reconstruction of the GDL geometrical structure. The GDL is represented as cylindrical carbon fibers that are equally spaced horizontally and stacked vertically to form mechanical contacts, Fig. 3. The next step is mechanical modeling of the contacting fibers. The Hertzian theory [9] is used to evaluate the contact area between fibers, and a thermal resistance network is constructed to account for the effective thermal conductivity, allowing analytic determination of the effective thermal conductivity. The results of the model are compared to experimental data. Moreover, parametric study is then performed to investigate the effect of key parameters on the effective thermal conductivity of GDLs.

2. Model development

Both electrical and thermal conductivity of carbon paper GDLs are orthotropic [4,10], with in-plane conductivity that are an order of magnitude higher than the through plane value. The thermal field and heat transfer rates depend on a variety of factors including, geometry, material properties of the various components and operating conditions, the heat transfer in the GDL is however generally limited by the through plane conductivity value on which we focus our analysis. The model considers the GDL to consist of a periodic fibrous micro structure and assumes:

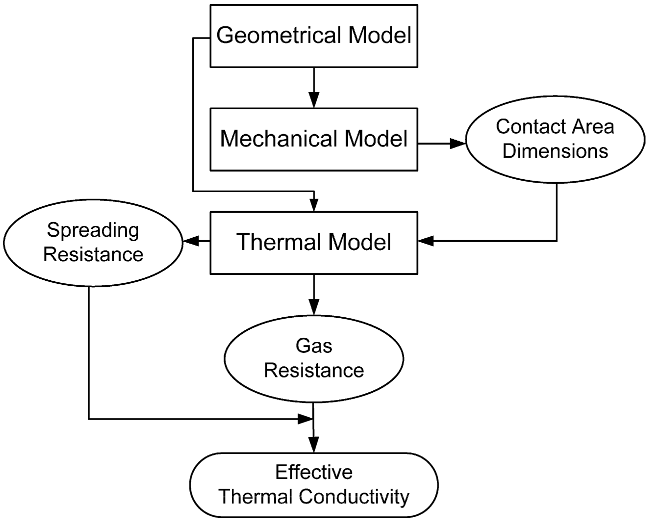

Fig. 2. Model development.

(1) 3-D repeating basic cell, Fig. 3.
(2) Steady state one-dimensional heat transfer.
(3) Negligible natural convection; justified by the Grashof number for a typical GDL with fiber diameter of 8.5 μm which is in order of 10^{-6} and is significantly lower than 2500, the limit for natural convection [11].
(4) No radiation heat transfer. PEM fuel cells typically operate between 60 and 90 °C, and the contribution of radiation is small and can be neglected.

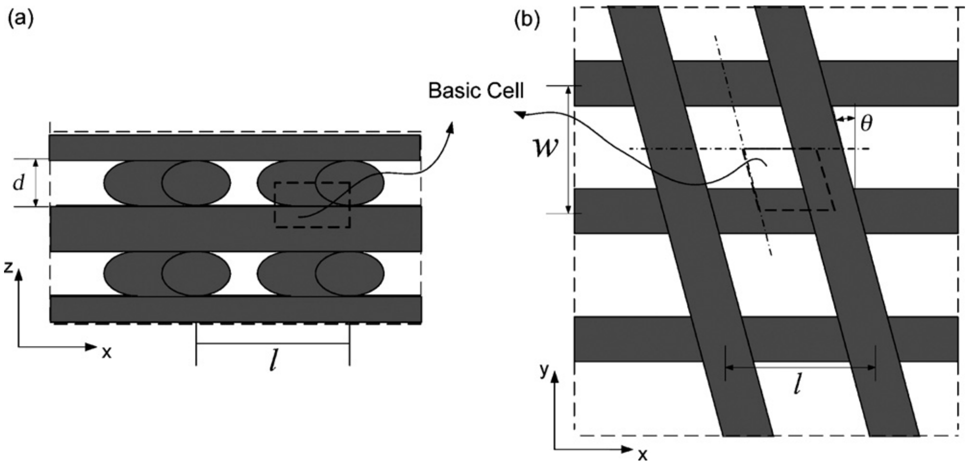

Fig. 3. (a) Front view and (b) top view of the geometrical model of GDL.

(5) Regular fiber surfaces (no roughness or out-of-flatness for contacting fibers).

Based on these assumptions, we propose a resistance network model for conduction through the solid and gas phases which accounts for geometric structure, effect of compression, gas rarefaction effect (in microgaps between fibers), and spreading resistance.

2.1. Geometrical model

Fig. 1 shows SEM image of a Toray GDL that clearly illustrates the random and anisotropic structure. The proposed geometrical model is an idealization shown in Fig. 3 and consists of uniformly sized equally spaced cylindrical fibers immersed in stagnant air. The fibers angle, θ, is variable in this model.

The porosity is defined as:

$$\varepsilon = 1 - \frac{V_s}{V_{tot}} \qquad (1)$$

where V_s and V_{tot} are the volume of fibers and the basic cell, respectively. Calculating these volumes based on the basic cell geometry in Fig. 3 yields:

$$\varepsilon = 1 - \frac{\pi d}{8}\left[\frac{l + (w/\cos\theta)}{lw}\right] \qquad (2)$$

2.2. Mechanical model

Thermal energy transfers from one fiber to another through the contact interface, and resistance to heat conduction depends on the contact area dimensions. In order to determine the contact area dimensions, the Hertzian theory [9] is used in the present study.

The general shape of the contact area is elliptical; when $\theta = 0$, the contact area becomes circular. Applying the Hertzian theory [9], the semi-axes of the contact area are given by:

$$b = \left(\frac{\rho''}{\rho'}\frac{3F\rho_e}{4E'}\right)^{1/3} F_1 \qquad (3)$$

$$a = b\left(\frac{\rho'}{\rho''}\right)^{2/3} \qquad (4)$$

where a and b are the major and minor semi-axes of the elliptical contact area, respectively; ρ_e is the equivalent radius of curvature, $\rho_e = \sqrt{\rho'\rho''}$ [9]; and E' is a modulus incorporating the fibers Young's modulus and Poisson's ratio.

$$E' = \left(\frac{1-\nu_1^2}{E_1} + \frac{1-\nu_2^2}{E_2}\right)^{-1} \qquad (5)$$

ρ' and ρ'' are the major and minor relative radii of curvature at the contact point expressed as [9]:

$$\rho'' = \frac{d}{\sqrt{2(1-\cos 2\theta)} + 2} \qquad (6)$$

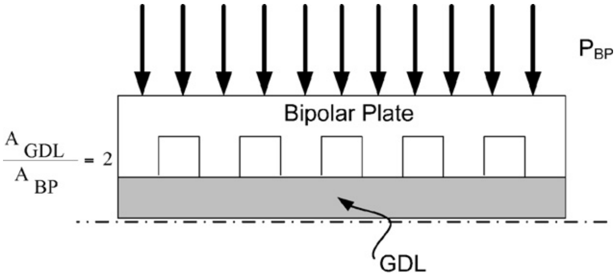

Fig. 4. Pressure distribution on the bipolar plate and GDL.

$$\rho' = \frac{1}{(4/d) - (1/\rho'')} \qquad (7)$$

F_1, the parameter used in Eq. (3), is a complex integral function of $(\lambda = \rho'/\rho'')$ [9]. We correlate this integral and propose the following relationship:

$$F_1 = \frac{19.1\sqrt{\lambda}}{1 + 16.76\sqrt{\lambda} + 1.34\lambda} \qquad (8)$$

The accuracy of the relationship is within 0.08%.

In order to determine the contact area dimensions, the magnitude of the contact force is required. This force F can be evaluated from the clamping pressure applied via the fuel cell bipolar plates. The land/flow channel area ratio used in PEM fuel cells is optimized to balance electrical conduction and mass transport and is typically of order 1 as shown in Fig. 4. Thus the maximum pressure to which the GDL is subjected is twice that of the bipolar plate, i.e. $P_{GDL} = 2P_{BP}$. As shown in Fig. 3, a cell with the cross-sectional area of lw consists of four contact points; therefore, the corresponding maximum force on each contact is:

$$F_{max} = \frac{P_{GDL}\, lw}{4} \qquad (9)$$

2.3. Thermal model

Based on the assumptions discussed in Section 2, a thermal resistance network corresponding to the basic cell is constructed as shown in Fig. 5 by considering the top and bottom blocks of the basic cell structure. The thermal resistances in the network represent the heat transfer paths through the gas and carbon fibers, see Fig. 6. The solid bulk resistance is small compared with the gap resistance and its effect on the total resistance is negligible and not accounted.

2.3.1. Thermal constriction/spreading resistance

Thermal constriction/spreading resistance is defined as the difference between the average temperature of the contact area and the average temperature of the heat source/sink, which is located far from the contact area, divided by the total heat flow rate Q [12].

$$R_{co} = R_{sp} = \frac{\Delta T}{Q} \qquad (10)$$

If the contact areas are small compared with the distance separating them, the heat source on a half-space solution can

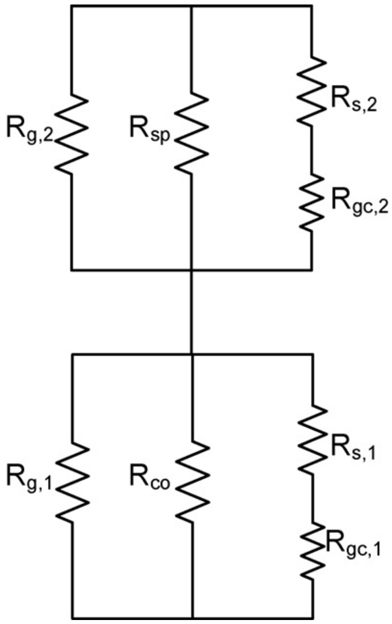

Fig. 5. Thermal resistance network for the top and bottom blocks of the basic cell.

be used [13]. Fig. 7 illustrates the geometry of a circular heat source on a half-space.

The spreading resistance for an isothermal elliptical contact area can be determined analytically [14]:

$$R_{\mathrm{sp}} = \frac{1}{2\pi k a} K(\eta) \tag{11}$$

where $\eta = \sqrt{1-(b/a)^2}$ and $K(\eta)$ is the complete elliptic integral of the first kind of modulus η.

$$K(\eta) = \int_0^{\pi/2} \frac{\mathrm{d}t}{\sqrt{[1-\eta^2 \sin^2 t]}} \tag{12}$$

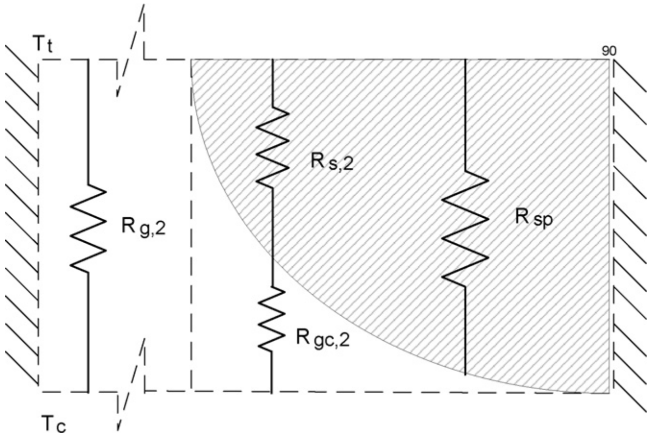

Fig. 6. Thermal resistances for the top block of the basic cell.

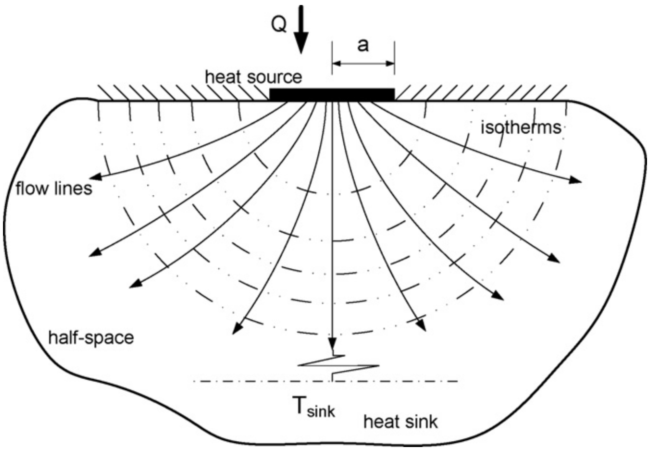

Fig. 7. Circular heat source on a half-space.

2.3.2. Gas resistance

Gas resistance can be decomposed into two parallel resistances for each block, see Fig. 6. Kennard [15] modeled the gas conduction between two parallel plates for temperature jump as $Q_{\mathrm{gc}} = k_{\mathrm{g}} A \Delta T/(\delta + M)$. Yovanovich [16] showed that this expression can be used for all possible regimes. We assume that heat conduction at each differential element, dx, is similar to that between parallel plates; therefore, using Kennard's expression for each differential element, we find:

$$\mathrm{d}Q_{\mathrm{gc}} = k_{\mathrm{g}} \left(\frac{w}{2}\right) \frac{\Delta T(x)}{\delta(x) + M} \mathrm{d}x \tag{13}$$

The gas parameter M is defined as:

$$M = \alpha \beta \Lambda \tag{14}$$

The mean free path Λ of the gas molecules can be expressed in terms of $\Lambda_{\mathrm{g},\infty}$, the mean free path of gas molecules at the reference state.

$$\Lambda = \Lambda_{\mathrm{g},\infty} \left(\frac{T_{\mathrm{g}}}{T_{\mathrm{g},\infty}}\right) \left(\frac{P_{\mathrm{g},\infty}}{P_{\mathrm{g}}}\right) \tag{15}$$

with $T_{\mathrm{g},\infty} = 25^\circ$ C and $P_{\mathrm{g},\infty} = 1$ atm. The thermal accommodation parameter α and the fluid property parameter β are defined by:

$$\alpha = \left(\frac{2-\alpha_1}{\alpha_1}\right) + \left(\frac{2-\alpha_2}{\alpha_2}\right) \tag{16}$$

$$\beta = \frac{2\gamma}{Pr(\gamma+1)} \tag{17}$$

where γ is the ratio of specific heats, Pr is the Prandtl number, and α_1, α_2 are thermal accommodation coefficients of the top and bottom surfaces. Here, the top surface corresponds to carbon fiber and the bottom to the gas, i.e. $\alpha_1 = \alpha_{\mathrm{s}}$ and $\alpha_2 = 1$,

$$\alpha = \left(\frac{2-\alpha_{\mathrm{s}}}{\alpha_{\mathrm{s}}}\right) + 1 \tag{18}$$

Song and Yovanovich [17] experimentally correlated the thermal accommodation coefficient.

$$\alpha_{\mathrm{s}} = \exp\left[-0.57\left(\frac{T_{\mathrm{s}}-273}{273}\right)\right]\left(\frac{1.4M_{\mathrm{g}}}{6.8+1.4M_{\mathrm{g}}}\right) + \frac{2.4\mu}{(1+\mu)^2} \times \left\{1 - \exp\left[-0.57\left(\frac{T_{\mathrm{s}}-273}{273}\right)\right]\right\} \tag{19}$$

where $\mu = M_g/M_s$; M_g and M_s are molecular weights of the gas and the solid.

The total heat flow through the gas-filled gap, gas filled between the quarter cylindrical fiber and the separating plane, is given by the integral

$$Q_{gc} = k_g \left(\frac{w}{2}\right) \int_0^{d/2\cos\theta} \frac{\Delta T(x)}{\delta(x)+M} \mathrm{d}x \tag{20}$$

The thermal resistance of the gas-filled gap, $R_{gc,2}$, is defined in terms of the temperature difference between two bounding surfaces, ΔT_c.

$$\frac{1}{R_{gc,2}} = \frac{Q_{gc}}{\Delta T_c} = k_g \frac{w}{2\Delta T_c} \int_0^{d/2\cos\theta} \frac{\Delta T(x)}{\delta(x)+M} \mathrm{d}x \tag{21}$$

The local gap thickness can be defined based on the geometry of the contact interface.

$$\delta(x) = \frac{d}{2} - \sqrt{\frac{d^2}{4} - (x\cos\theta)^2} \tag{22}$$

Considering isothermal bounding surfaces , $\Delta T(x) = \Delta T_c$, the thermal resistance, Eq. (21) reduces to:

$$\frac{1}{R_{gc,2}} = k_g \left(\frac{w}{2}\right) \int_0^{d/2\cos\theta} \frac{\mathrm{d}x}{\delta(x)+M} \tag{23}$$

The thermal resistance $R_{gc,2}$ can then be calculated by substituting Eqs. (14) and (22) into Eq. (23). This equation can also be used for $R_{g,2}$ by setting $\delta(x) = d/2$ and $\alpha = 2$ (both surfaces are gas):

$$\frac{1}{R_{g,2}} = k_g \left(\frac{w}{2}\right) \frac{((l-(d/\cos\theta))/2)}{(d/2)+\alpha\beta\Lambda} \tag{24}$$

The thermal resistances for the bottom block can be obtained following the same procedure.

$$\frac{1}{R_{gc,1}} = k_g \left(\frac{l\cos\theta}{2}\right) \int_0^{d/2\cos\theta} \frac{\mathrm{d}x}{\delta(x)+M} \tag{25}$$

$$\frac{1}{R_{g,1}} = k_g \left(\frac{l\cos\theta}{2}\right) \frac{((w-d)/2\cos\theta)}{(d/2)+\alpha\beta\Lambda} \tag{26}$$

2.3.3. Effective thermal conductivity

Once the individual resistances are determined, the thermal resistance network shown in Fig.5 is used to evaluate the total resistance of the basic cell:

$$R_{tot} = \left[\frac{1}{R_{sp}} + \frac{1}{R_{gc,2}} + \frac{1}{R_{g,2}}\right]^{-1} + \left[\frac{1}{R_{co}} + \frac{1}{R_{gc,1}} + \frac{1}{R_{g,1}}\right]^{-1} \tag{27}$$

The effective thermal conductivity of the GDL is given by:

$$k_{eff} = \frac{d}{R_{tot}A} = \frac{4d}{lwR_{tot}} \tag{28}$$

3. Results and discussion

The model was implemented into a Mathematica script [18] to allow convenient parametric studies and analysis. The thermophysical properties of the gas and carbon fibers used in the program are given in Tables 1 and 2. The gas phase is taken as air to correspond to available experiments used for validation.

Table 1
Properties of air

$\Lambda_{g,\infty}$ (μm)	$k_{g,\infty}$ (W/mK)	T_g (K)	P_g (kPa)	Pr	γ
0.07 [20]	0.03 [4]	350 [21]	101.3 [4]	0.7164	1.398

Table 2
Carbon fiber properties

d (μm)	k_s (W/mK)	ν	E (GPa)	P_{BP} (kPa)
8.5	120 [4]	0.3 [22]	210 [23]	482

3.1. Model validation

Fig. 8 compares the model to experimental data from a variety of sources obtained over a range of porosities. As shown in Fig. 8, there is good agreement between the model and experimental data with an average difference of approximately 7.5% when $\theta = 0$. The model results for three arbitrarily chosen angles are also shown in Fig. 8. The case $\theta = 0$ yields better overall agreement with experimental data and for small fiber angles, the effect of angle is negligible. In an actual GDL, the fiber angle distribution is random and it is expected that the average value would correspond to the orthogonal arrangement, $\theta = 0$, as the present model suggests. This is corroborated by the recent results of Van Doormal [19] who performed Lattice Boltzmann simulation in reconstructed GDLs and observed that the orthogonal arrangement yields permeability values that are indistinguishable from those computed using a random fiber arrangement. The case $\theta = 0$ is therefore selected as the reference case for the parametric studies.

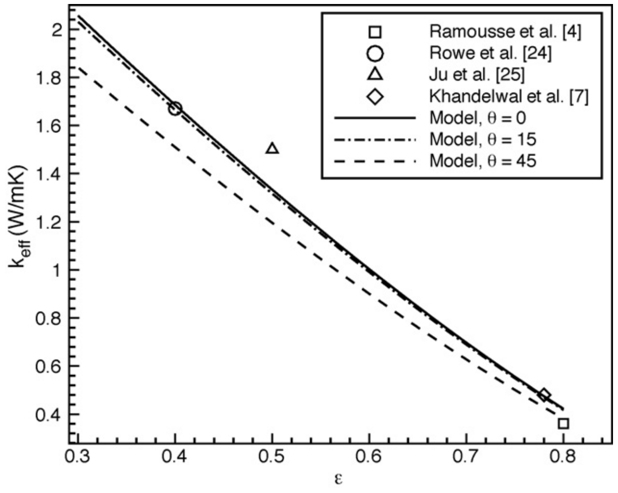

Fig. 8. Comparison of predicted and measured effective conductivities over a range of GDL porosities. (See Refs. [4,7,24,25]).

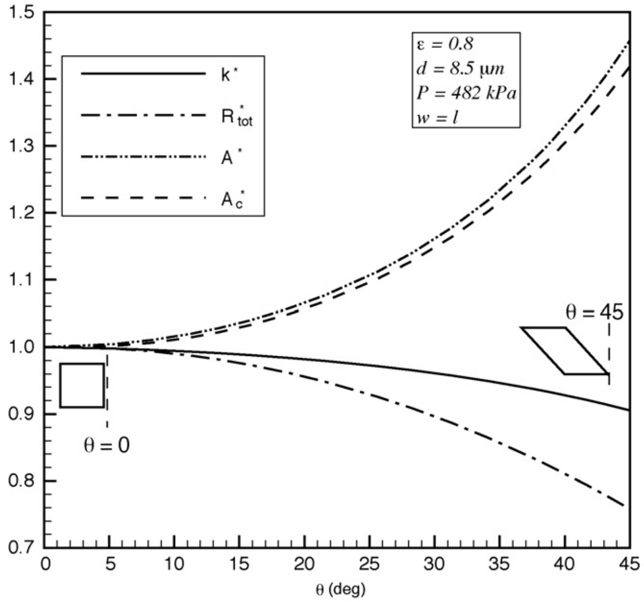

Fig. 9. Effect of fibers angle (θ) on effective thermal conductivity.

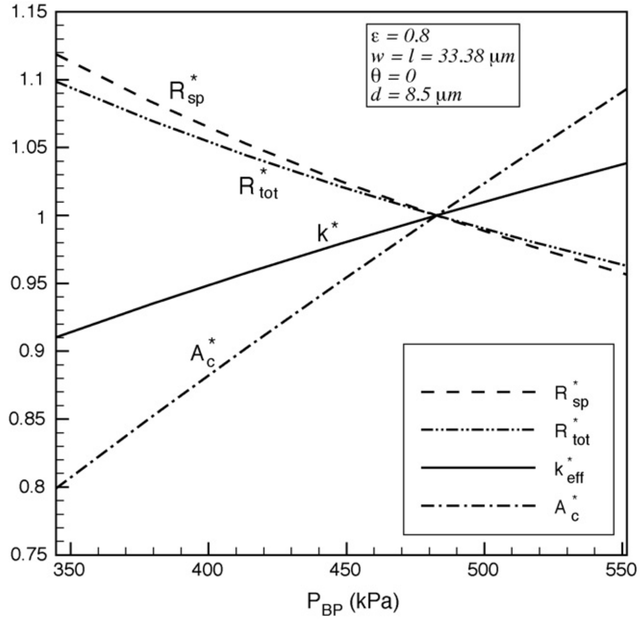

Fig. 10. Effect of bipolar plate pressure on effective thermal conductivity.

3.2. Parametric study

The proposed model can be conveniently used to systematically investigate the influence of key GDL parameters/properties on its effective thermal conductivity. Parametric studies were conducted by varying fibers angle, bipolar pressure, aspect ratio, fiber diameter, and operation temperature. When a parameter is studied, the rest of mentioned parameters are kept constant.

3.2.1. Fibers angle

The preferred conduction path corresponds to smallest resistance which is through the contact between fibers. This path includes spreading resistance; and is hence expected to have a significant influence on the effective thermal conductivity. The effect of fibers angle on the non-dimensional properties of the basic cell is shown in Fig. 9. The properties are non-dimensionalized with respect to the reference case, see Table 3. As shown in Fig. 9, the contact area increases with increasing θ in turn results in a reduction in spreading and consequently, total resistances. However this is counterbalanced by an increase in the basic cell area, and because the latter dominates over the resistance in this case, the net effect is a reduction of the effective thermal conductivity. This effect becomes more pronounced for higher fiber angles.

3.2.2. Bipolar pressure

The effect of bipolar pressure on the thermal conductivity of GDL is shown in Fig. 10. Higher bipolar plate pressures result in higher thermal conductivities. A higher pressure leads to an increase in the contact area that in turn leads to a decrease in the spreading resistance, and thus higher effective thermal conductivity. It should be noted that as a result of increasing pressure, the height of the basic cell is expected to decreases due to elastic compression. However, this effect is small, i.e. a reduction of less than 1% in fiber diameter, thus is neglected in this study. In an operating fuel cell, the compressive force to which the GDL is subjected is expected to vary from a maximum under the land area of the bipolar plate to a minimum under the centre of the flow channel. The sensitivity to pressure shown by the model suggests that the effective conductivity is non-homogeneous and this should be accounted for in comprehensive fuel cell models.

Table 3
The reference case parameters

θ	$w = l$ (μm)	d_0 (μm)	ε	P_{BP} (kPa)	T_g (K)
0	33.38	8.5	0.8	482	350

3.2.3. Aspect ratio

Fig. 11 shows the effect of aspect ratio $\xi = w/l$ for a GDL with a porosity $\varepsilon = 0.8$. As shown, the lower the aspect ratio, the lower the effective thermal conductivity. When the aspect ratio is reduced, in order to maintain the same porosity, l has to be increased while w is decreased, see Eq. (2). This leads to a larger basic cell area, and since the bipolar pressure is kept constant results in larger contact force and hence a lower spreading resistance. Thus the total resistance decreases when the porosity is constant, but this is counteracted by a proportionally larger increase in the basic cell area, and thus a lower effective thermal conductivity.

3.2.4. Fiber diameter

The effect of carbon fiber diameter on the effective thermal conductivity at a constant porosity is shown in Fig. 12. The total resistance decreases with an increase in the fiber diameter. To keep the porosity constant, however, the length and width of the basic cell have to be increased as the diameter increases. Consequently, the area of the basic cell becomes larger and the total thermal resistance decreases. However, a larger diameter leads

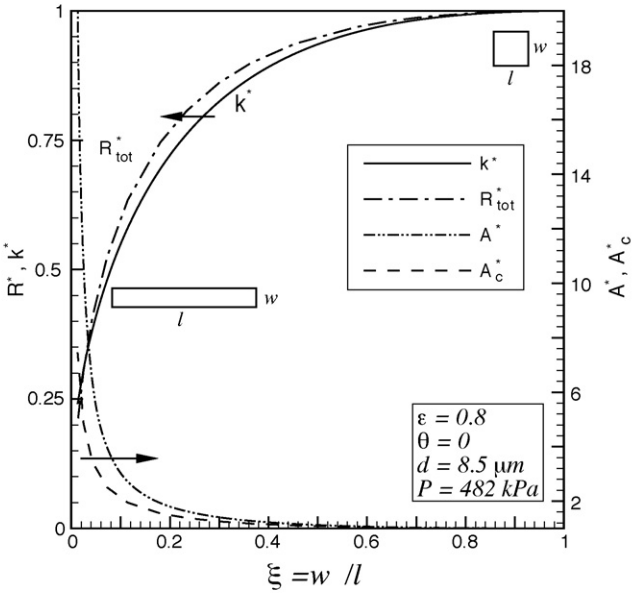

Fig. 11. Effect of aspect ratio on effective thermal conductivity.

to a larger basic cell area which negatively impacts the effective thermal conductivity. Because the effect of the cell height extension and total resistance reduction is higher than the area enlargement, the net effect is a bit increase in the effective thermal conductivity with fiber diameter. In the typical range of 5–10 μm for the fiber diameter, the effective thermal conductivity remains approximately constant.

3.2.5. Operating temperature

Fig. 13 shows the effect of temperature on the effective thermal conductivity. The typical operating temperatures of automotive PEM fuel cell is in the 80–90 ° C range while air cooled and air breathing cells operate at lower temperatures; we thus investigate variations in the 15–100 ° C range. The thermal and mechanical properties of the fiber are assumed to remain constant within this range; however, the effects of temperature variations are considered in gas(air) thermophysical properties e.g. M, k, etc. As shown in Fig. 13, the gap resistance R_{gc} increases slightly with temperature, whereas the gas resistance R_{g} decreases. The two effects balance each other and also the spreading resistance does not vary, therefore, the effective thermal conductivity remains approximately constant.

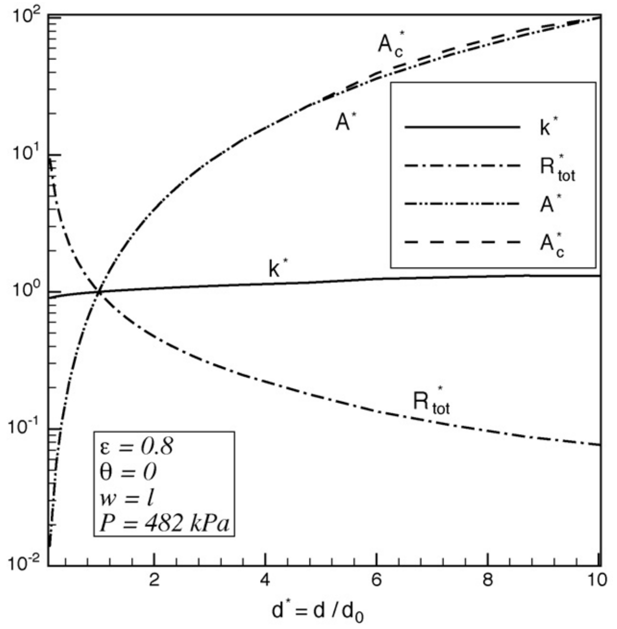

Fig. 12. Effect of fiber diameter on effective thermal conductivity.

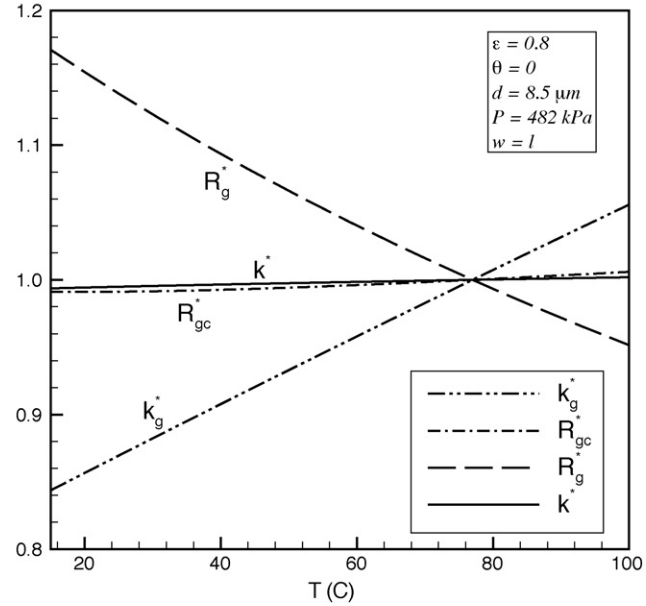

Fig. 13. Effect of the operating temperature on effective thermal conductivity.

4. Summary and conclusions

A compact analytical model for evaluating the effective thermal conductivity of fibrous GDLs has been developed. The model accounts for the salient geometric features, the effect of mechanical compression, and spreading resistance through fibers. The model predictions are in good agreement with existing experimental data over a wide range of porosities, $0.3 < \varepsilon < 0.8$. Parametric studies have been performed using the proposed model to investigate the trends and effects of bipolar plate pressure, aspect ratio, fiber diameter, fiber angle, and operating temperature. The highlights of the analysis are:

- Constriction/spreading resistance is the controlling component of the total resistance.
- Orthogonal arrangement of fibers, $\theta = 0$ yields better overall agreement with experimental data and corroborated by the recent results of Van Doormal [19].
- The influence of fiber angle θ on the effective thermal conductivity decreases at higher porosities.
- Higher bipolar pressure significantly improves the effective thermal conductivity.
- Reducing the aspect ratio, $\xi = w/l$, to approximately 0.7 has a negligible impact on the effective thermal conductivity. However, for $\xi < 0.3$, the effect of aspect ratio becomes important.

The analysis indicates that the best effective thermal conductivity is achieved when $\xi = 1$ (square basic cell).

- Neither changes in fiber diameter (5–10μm) nor operating temperature for the range of 15–100 °C have any significant effect on the effective thermal conductivity.

The compact model presented here, reproduces faithfully the effects of many operational and geometrical parameters on effective thermal conductivity. The model can be used to guide the design of improved GDLs, and can be readily implemented into fuel cell models that require specification of the effective thermal conductivity.

Acknowledgements

The authors are grateful for the financial support of the Natural Sciences and Engineering Research Council (NSERC) of Canada, and the Canada Research Chairs Program. The SEM image in Fig. 1 was provided by Aimy Bazylak.

References

[1] N. Djilali, D. Lu, Int. J. Therm. Sci. 41 (2002) 29–40.
[2] A. Hakenjos, H. Muenter, U. Wittstadt, C. Hebling, J. Power Sources 131 (2004) 213–216.
[3] J.P. Feser, A.K. Prasad, S.G. Advani, J. Power Sources 162 (2006) 1226–1231.
[4] J. Ramousse,S. Didierjean, P. Lottin, D. Maillet, Int. J. Therm. Sci. 47 (2008) 1–8.
[5] B.R. Sivertsen, N. Djilali, J. Power Sources 141 (1) (2005) 65–78.
[6] F. Danes, J.P. Bardon, Revue Générale de Thermique 36 (1997) 302–311.
[7] M. Khandelwal, M.M. Mench, J. Power Sources 161 (2006) 1106–1115.
[8] M. Bahrami, M.M. Yovanovich, J.R. Culham, Int. J. Heat Mass Transfer 49 (2006) 3691–3701.
[9] K.L. Johnson, Contact Mechanics, Cambridge University Press, London, UK, 1985 (Chapter 4).
[10] W. Sun, B.A. Peppley, K. Karan, J. Power Sources 144 (1) (2005) 42–53.
[11] V.S. Arpaci, P.S. Larsen, Convection Heat Transfer, Prentice-Hall, Englewood Cliffs, NJ, 1984 (Chapter 4).
[12] H.S. Carslaw, J.C. Jaeger, Conduction of Heat in Solids, second ed., Oxford University Press, London, UK, 1959.
[13] A.M. Clausing, B.T. Chao, J. Heat Transfer 87 (1965) 243–251.
[14] M.M. Yovanovich, E.E. Marotta, A. Bejian, D. Kraus, in: Heat Transfer Hand Book, John Wiley and Sons Inc, New York, 2003 (Chapter 4).
[15] E.H. Kennard, Kinetic Theory of Gases, McGraw-Hill, New York, 1938 (Chapter 8).
[16] M.M. Yovanovich, Spacecraft Radiative Transfer and Temperature Control, AIAA, New York, 83 (1992) 83–95.
[17] S. Song, M.M. Yovanovich, Fundamentals of Conduction and Recent Developments in Contact Resistance ASME HTD, 69 (1987) 107–115.
[18] Wolfram Mathematica 6, Wolfram Research, Inc., 1988–2007.
[19] M. Van Doormaal, Determination of permeability in fibrous porous media using the lattice Boltzmann method with application to PEM fuel cells, M. Eng. thesis, Queen's University, Kingston, 2006.
[20] M.V. Williams, E. Begg, L. Bonville, H.R. Kunz, J.M. Fenton, J. Electrochem. Soc., A 151 (8) (2004) 1173–1180.
[21] K. Rajashekara, J. IEEE 41 (3) (2005).
[22] H. Miyagawa, C. Sato, T. Masea, E. Drowna, J. Mater. Sci. Eng., A 412 (2005) 88–92.
[23] A. Kusoglu, A.M. Karlsson, M.H. Santare, S. Cleghorn, W.B. Johnson, J. Power Sources 161 (2006) 987–996.
[24] A. Rowe, X. Li, J. Power Sources 102 (2001) 82–96.
[25] H. Ju, C.Y. Wang, S. Cleghorn, U. Beuscherb, J. Electrochem. Soc., A 52 (2005) 1645–1653.

Appendix D

Effective Thermal Conductivity and Thermal Contact Resistance of Gas Diffusion Layers in PEM Fuel Cells. Part 1: Effects of Compressive Load

Reproduced by permission of Elsevier

Journal of Power Sources 196 (2011) 246–254

Contents lists available at ScienceDirect

Journal of Power Sources

journal homepage: www.elsevier.com/locate/jpowsour

Effective thermal conductivity and thermal contact resistance of gas diffusion layers in proton exchange membrane fuel cells. Part 1: Effect of compressive load

E. Sadeghi[a,b,*], N. Djilali[a], M. Bahrami[b]

[a] Dept. Mechanical Eng., and Institute for Integrated Energy Systems, University of Victoria, P.O. Box 3055, Victoria, BC, Canada V8W 3P6
[b] Mechatronic Systems Engineering, School of Engineering Science, Simon Fraser University, Surrey, BC, Canada V3T 0A3

ARTICLE INFO

Article history:
Received 7 May 2010
Received in revised form 11 June 2010
Accepted 11 June 2010
Available online 20 June 2010

Keywords:
TCR
Interface
Effective thermal conductivity
Conduction
Compression

ABSTRACT

Heat transfer through the gas diffusion layer (GDL) is a key process in the design and operation of a PEM fuel cell. The analysis of this process requires determination of the effective thermal conductivity as well as the thermal contact resistance associated with the interface between the GDL and adjacent surfaces/layers.

In the present study, a custom-made test bed that allows the separation of effective thermal conductivity and thermal contact resistance in GDLs under vacuum and ambient conditions is described. Measurements under varying compressive loads are performed using Toray carbon paper samples with a porosity of 78% for a range of thicknesses. The measurements are complemented by compact analytical models that achieve good agreement with experimental data. A key finding is that thermal contact resistance is the dominant component of the total thermal resistance; neglecting this phenomenon may result in significant errors in evaluating heat transfer rates and temperature distributions.

1. Introduction

The electrochemical reaction and associated irreversibilities in a proton exchange membrane (PEM) fuel cell generate a substantial amount of heat that results in temperature gradients in various components of a cell [1–4]. The product heat has to be extracted from the cell to maintain optimal working conditions; indeed the implementation of efficient and reliable cooling strategies for PEM fuel cells is crucial to ensure high efficiency, reliability and durability.

Accurate knowledge of the temperature distribution and associated heat transfer mechanisms is required to determine various transport phenomena such as water and species transport, reaction kinetics, and rate of phase change. For instance, saturation pressure, which determines phase equilibrium between liquid water and gas phases in both the gas flow channels and porous media of a fuel cell, varies non-linearly with temperature. A thermal analysis is also required to assess thermal-related phenomena in the gas diffusion layer (GDL) and the catalyst layer that can induce hygro-thermal stress and material degradation, and compromise performance and lifetime [5,6]. Any successful fuel cell thermal analysis requires two key transport coefficients: (i) the effective thermal conductivity of the gas diffusion layer (GDL) as a function of the micro-structural geometry of the GDL and the operating conditions, e.g. compressive load and temperature and (ii) the thermal contact resistance (*TCR*). The latter is an interfacial phenomenon arising due to imperfect contact at the interface between the GDL and the solid surface of the bipolar plates as well as at the catalyst layer–GDL interface. Considering the small thickness of the components that make up the membrane–electrode-assembly, and the very distinct surface morphology of the membrane, catalyst layer and GDL, interfacial transport phenomena are expected to have a significant impact in general, and *TCR* in particular can give rise to a significant resistance which will limit heat transfer rates through the GDL.

Generally, all surfaces have roughness and out-of-flatness at the microscale level, and the actual contact area is thus only a fraction of the nominal contact area [7]. In GDLs with high porosity, this scenario is even worse, with actual contact area expected to be less than 1% of the nominal cross-sectional area. In addition, the complexity and anisotropy of the GDL micro-structure make it intricate to define accurate values for *TCR* and the effective thermal conductivity.

Large differences in thermal conductivity of solid and fluid phases as well as high porosity of GDL micro-structure make it necessary to define an effective thermal conductivity, a transport parameter that plays an important role in fuel cell performance analysis [8] and that is required in computational models [9]. A few studies in the literature have focused on the analytical model-

---

* Corresponding author at: Dept. Mechanical Eng., and Institute for Integrated Energy Systems, University of Victoria, P.O. Box 3055, Victoria, BC, Canada V8W 3P6. Tel.: +1 7787828587; fax: +1 2507216051.
E-mail address: ehsans@uvic.ca (E. Sadeghi).

0378-7753/$ – see front matter © 2010 Elsevier B.V. All rights reserved.
doi:10.1016/j.jpowsour.2010.06.039

Nomenclature

A	cross-sectional area (m^2)
A_0	nominal contact area (m^2)
a	major semi-axis of contact area (m)
b	minor semi-axis of contact area (m)
D_{peak}	peak density of surface (m^{-1})
d	fiber mean diameter (m)
E	Young's modulus (Pa)
E^*	effective Young's modulus (Pa)
F	force (N)
h	separation of contacting surfaces (m)
k	thermal conductivity ($\mathrm{W\,m^{-1}\,K^{-1}}$)
k_{eff}	effective thermal conductivity ($\mathrm{W\,m^{-1}\,K^{-1}}$)
N	number of microcontacts
P_0	reference contact pressure (Pa)
P_{atm}	atmospheric pressure (Pa)
P_{c}	contact pressure (Pa)
P_{c}^*	dimensionless contact pressure
P_{g}	gas pressure (Pa)
Q	heat transfer rate (W)
R_{e}	effective radius of contacting bodies (m)
R_{GDL}	GDL thermal resistance ($\mathrm{K\,W^{-1}}$)
R_{p}	asperity radius (m)
R_{sp}	thermal spreading resistance ($\mathrm{K\,W^{-1}}$)
R_{tot}	total thermal resistance ($\mathrm{K\,W^{-1}}$)
r	fiber mean radius (m)
T	temperature (K)
TCR	thermal contact resistance ($\mathrm{K\,W^{-1}}$)
t	sample thickness (m)
t_0	nominal sample thickness (m)
z	height (m)

Greek symbols

α	aspect ratio of the contact area (ba^{-1})
ε	strain ($\Delta t \cdot t_0^{-1}$)
σ	root mean square of the surface roughness
ν	Poisson's ratio
λ	onset of elastic deformation (m)
δ	deviation in parameters
δ_{e}	elastic deformation (m)
δ_{s}	thickness reduction caused by fiber slippage (m)
δ_{tot}	total thickness reduction (m)
$\kappa(\cdot)$	elliptic integral of the first kind
$\psi(\cdot)$	constriction parameter
$\phi(\cdot)$	normal distribution

Subscripts

1	sample 1
2	sample 2
c	carbon fiber
fl	fluxmeter
low	lower contact surface
up	upper contact surface
uc	unit cell

ing of GDL thermal conductivity. Ramousse et al. [8] investigated the effective thermal conductivity of non-woven carbon felt GDLs and estimated the conductivity bounds using a model connecting the two phases (solid and gas) in series or parallel. They used Danes and Bardon correlation [10] to estimate the effective thermal conductivity of the solid phase. The model as well as the experimental measurements yielded conductivity values that are lower than most values reported in the literature. Using the unit cell concept, the present authors recently presented a compact analytical model to determine the effective thermal conductivity of GDLs [11]. A micro-structure of uniformly sized, equally spaced cylindrical fibers immersed in stagnant air was assumed, and the Hertzian theory [7] was used to calculate the contact area between the touching fibers, considering a range of fiber angles. The analysis was performed by constructing a thermal resistance network that takes into account the thermal paths through solid fibers (constriction and spreading resistance) and air (rarefaction effects).

The complexity of the GDL micro-structure and associated challenges in obtaining analytic solutions have lead most researchers toward numerical [12,13] and experimental methods [14–16]. Becker et al. [12] used 3D tomography to reconstruct a GDL and a numerically efficient pore morphology method to determine phase distributions and to deduce permeability, diffusivity and thermal conductivity as a function of the saturation under different compressive loads. Wang et al. [13] developed a numerical method based on the Lattice Boltzmann technique to predict the effective thermal conductivity of randomly fibrous media. Assuming a two-dimensional stochastic and random micro-structure, a generation-growth method was employed to reconstruct the porous medium based on diameter, length, core position, and alignment of each fiber.

Khandelwal and Mench [14] measured the through-plane thermal conductivity of GDLs by examining two different types of commercial GDLs with a variety of thicknesses and porosities. They studied the effect of temperature and polytetrafluoroethylene (PTFE) content on the effective thermal conductivity, and obtained values in close agreement with the manufacturer data. The effect of pressure on effective thermal conductivity was investigates by Nitta et al. [15] using a guarded-hot-plate apparatus and SGL SIGRACET® 10 BA GDL samples. The GDL thickness under compressive loads was monitored using a dial indicator. The thermal conductivity was found to be independent of compression. Using a similar apparatus, Burheim et al. [16] measured the effective thermal conductivity of uncoated SolviCore gas diffusion layers under various compaction pressures. They presented a methodology to find thermal conductivity and thermal contact resistance (*TCR*) and results showing that the effective thermal conductivity increases with compressive load while *TCR* decreases.

The available studies on thermal contact resistance of GDLs in the literature are limited to experimental measurements and there is a lack of analytical investigations in this field. However, several pertinent analytical and experimental approaches have been reported on electrical contact resistance [17–20]. These studies have employed fractal based models [17] or the Hertzian elastic theory [18–20] to find the contact area between the asperities of GDL and bipolar plate/catalyst layer surfaces and have the potential of being extended to thermal analysis.

A review of the literature indicates that in the majority of previous studies related to heat transfer in GDL, the *TCR* was 'bundled up' with the effective thermal conductivity and characterized using an aggregate value. One fundamental issue with combining the two is that *TCR* is an *interfacial phenomenon* that is a function of mechanical load and surface characteristics of both interfacing surfaces, whereas thermal conductivity is a transport coefficient characterizing the *bulk* medium. Thermal conductivity and *TCR* should therefore be distinguished. Furthermore, the effect of compressive load on thermal conductivity and *TCR* has not been thoroughly investigated.

The experimental technique developed in this study allows the deconvolution of *TCR* and thermal conductivity and was used to perform a comprehensive experimental study:

- to determine through-plane thermal conductivity of GDLs as a function of porosity, compressive load, and temperature; and
- to measure the thermal contact resistance at the interface of GDL and a solid surface as a function of mechanical load and porosity.

A custom-made test bed was designed and built that enables the measurements of thermal conductivity and *TCR* of porous media under vacuum and ambient pressure conditions. The test bed was equipped with a loading mechanism that allows the application of various compressive loads on the samples. Toray carbon papers with the porosity of 78% and different thicknesses are used in the experiments. The effect of ambient and compression is investigated, and includes measurement of the GDL thickness variation using a tensile-compression apparatus. The effective thermal conductivity and *TCR* are deduced from the total thermal resistance measurements by performing a series of experiments with GDL samples of various thicknesses and similar micro-structures. The effect of operating temperature (35–70 °C) on both thermal conductivity and *TCR* is also investigated. Furthermore, analytical models are developed to evaluate through-plane thermal conductivity of GDLs as well as the thermal contact resistance at the interface of GDL and a solid surface as a function of the compressive load. These models are compared against the experimental data obtained in this study.

2. Experimental study

2.1. Thermal test

The experimental apparatus and a schematic of the test column in the test chamber are shown in Fig. 1. The test chamber consists of a stainless steel base plate and a bell jar enclosing the test column. The test column consists of, from top to bottom: the loading mechanism, the steel ball, the heater block, the upper heat fluxmeter, the sample, the lower fluxmeter, the heat sink (cold plate), the load cell, and the polymethyl methacrylate (PMMA) layer. The heater block consists of circular flat copper in which cylindrical pencil-type electrical heaters are installed. The power to the heaters can be adjusted manually. In the present study, a 30 W Omega heater is used. It should be noted that the determination of the thermal conductivity and thermal contact resistance are independent of the heat flux setting through the sample, and that for the purpose of such measurements this heat flux need not be related to the heat generated in an operating fuel cell. The setting of the heater was selected to be sufficiently high to provide good temperature resolution, while ensuring that the temperature in the samples remained in a range representative of fuel cell operation.

The designed cold plate consists of a hollow copper cylinder, 1.9 cm high and 15 cm diameter. Cooling is accomplished using a closed loop water–glycol bath in which the coolant temperature can be set. The cold plate is connected to the chiller unit which adjusts the cold water temperature. A 1000 lb load cell is used to measure the applied load to the joint. The load is applied over a load button placed at the center of the load cell.

The fluxmeters were made of a standard electrolyte iron material. To measure temperatures six T-type thermocouples were attached to each fluxmeter at specific locations shown in Fig. 1. The thermal conductivity of the iron fluxmeter was known and used to measure the heat flow rate transferred through the contact region.

2.1.1. Sample preparation

Toray carbon papers TGP-H-120 and TGP-H-060 with the porosity of 78% were used. These samples have 5% wet proofing and their thicknesses are 0.37 mm and 0.19 mm, respectively. The samples were cut in circles with 25 mm diameter and sandwiched between the fluxmeters. Fig. 2 shows scanning electron microscopy (SEM) images of the carbon papers before loading.

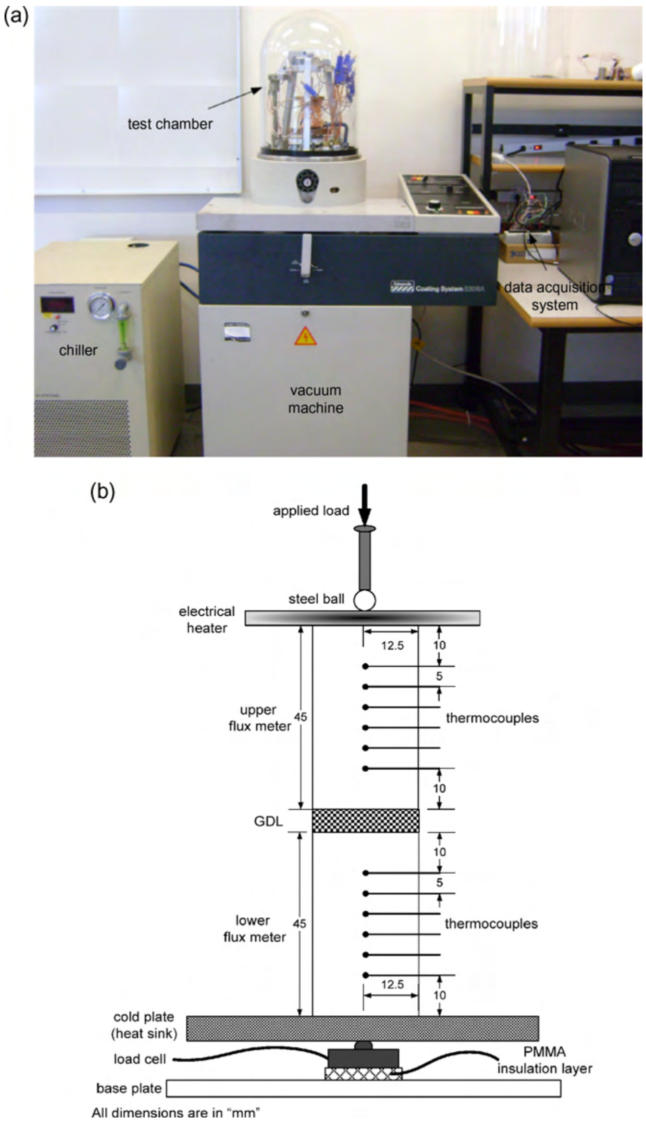

Fig. 1. (a) Experimental apparatus used for thermal conductivity and *TCR* test bed and (b) schematic view of the test column.

2.1.2. Test procedure

Experiments were conducted under vacuum and ambient conditions. A vacuum level of 10^{-5} mbar was achieved under the test chamber using the vacuum machine. To minimize heat transfer to the surrounding, the test column including the fluxmeters and samples was insulated using glass wool insulation layers. Temperatures and pressure were recorded at various compressive loads when steady-state conditions were achieved; to reach thermal equilibrium, all the experiment's parameters were kept constant and carefully monitored for approximately 4–5 h for each data point. The effects of compression were investigated over the range 0.2–1.5 MPa, i.e. up to values that correspond to the highest pressures transmitted in practice to the GDL from the current collecting plates [21].

The temperature gradient between the hot and cold plates results in essentially one-dimensional heat conduction from the top to the bottom of the test column. The temperature distribution is therefore stabilizing, and since the Grashof number is of the order of 10^{-6}, which is significantly lower than the critical value of 2500

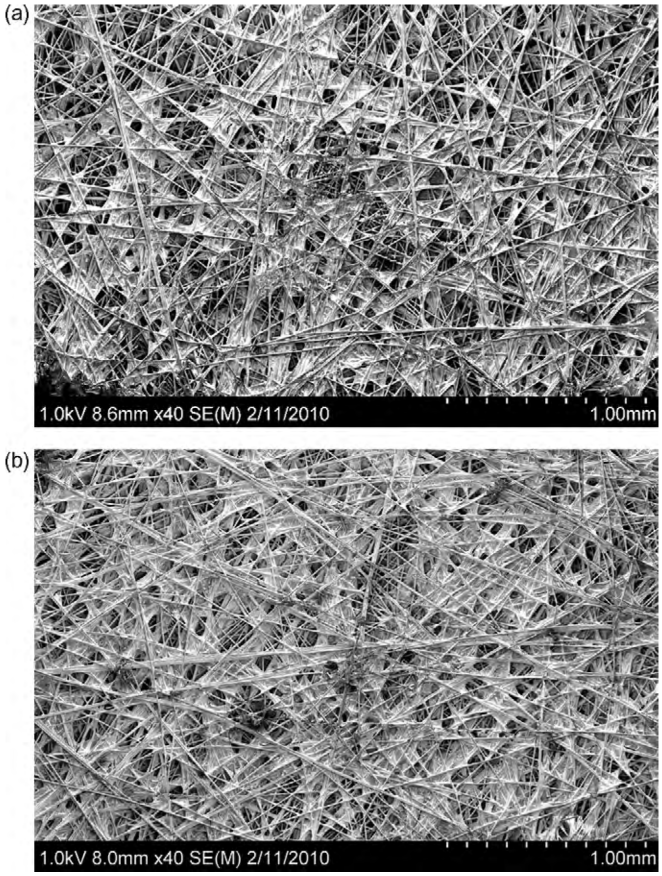

Fig. 2. SEM images of Toray carbon papers with 5% PTFE treatment and porosity of 78% before the experiments, ×40 magnification (a) TGP-H-120 with $t_0 = 0.37$ mm and (b) TGP-H-060 with $t_0 = 0.19$ mm.

corresponding to the lower threshold for natural convection [22], it is reasonable to assume negligible natural convection inside the GDL sample for the ambient pressure tests.

Radiation heat transfer between the fibers is also negligible since the temperature difference between fibers is small and the absolute temperature levels in the samples during the tests remain relatively low, i.e. less than 100 °C (373 K). Thus, the heat transfer through the fluxmeters is only due to diffusion through the fibers and air (atmospheric tests) and can be determined using Fourier's equation.

$$Q = -kA\frac{dT}{dz} \tag{1}$$

where dT/dz is the temperature gradient along the test column, k is the thermal conductivity of the fluxmeters, and A is the cross-sectional area of samples/fluxmeters. The temperatures at the top and bottom contact surfaces can be extrapolated through the measured heat flux. The total thermal resistance of the sample, R_{tot}, includes the sample thermal resistance and the thermal contact resistance (at the top and bottom surfaces) and can be expressed as:

$$R_{\text{tot}} = R_{\text{GDL}} + TCR = \frac{\Delta T_{\text{ul}}}{Q} \tag{2}$$

where ΔT_{ul} is the temperature difference between the upper and the lower contact surfaces. R_{GDL} and TCR are the GDL resistance and the total contact resistance, respectively. There are two interfaces between the GDL and the fluxmeters; it is assumed that the contact resistance at the top and bottom of the GDLs are equal; $TCR_{\text{up}} = TCR_{\text{low}} = (TCR/2)$.

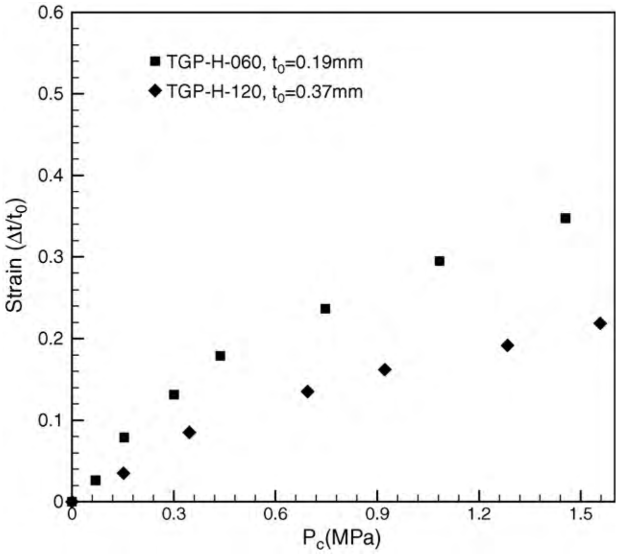

Fig. 3. Thickness variation of Toray carbon paper TGP-H-060 and TGP-H-120 under compression.

To deconvolute thermal conductivity and *TCR*, two experiments were performed with samples of different thicknesses; but with identical micro-structural parameters. Under the same pressure, the *TCR* for both samples is assumed to be equal. Applying Eq. (2) to both measurements and subtracting them yields the effective thermal conductivity:

$$k_{\text{eff}} = \frac{t_1}{R_{\text{GDL1}}A} = \frac{t_2}{R_{\text{GDL2}}A} \tag{3}$$

$$k_{\text{eff}} = \frac{t_1 - t_2}{(R_{\text{tot1}} - R_{\text{tot2}})A} \tag{4}$$

where t_1 and t_2 are the thicknesses of samples 1 and 2, respectively at the specific applied pressure, and A is the cross-section of samples. Eq. (4) can be used to find the effective thermal conductivity; the *TCR* can then be calculated by Eq. (2).

2.2. Mechanical test

The thickness variation of Toray carbon papers TGP-H-060 and TGP-H-120 under different compressive loads was measured using a tensile-compression apparatus. A Mitutoyo digital indicator with a 0.001 mm resolution was used to measure the thickness variation under compression. The GDL samples were cut in a circular shape of 25 mm diameter and then compressed by a steel rod using a pneumatic actuator. Various compression forces were applied on the GDL using the apparatus. A load cell with an accuracy of 2.5% was placed on the top of the samples. The load was increased at 15–20 min intervals to ensure mechanical equilibrium and steady-state condition. Measurements were repeated five times for each sample and the averaged values are reported in this work (see Fig. 3).

2.3. Uncertainty analysis

Considering the relationships for evaluating the effective thermal conductivity and the thermal contact resistance, i.e. Eqs. (4) and (2), the relevant parameters in the analysis can be expressed as:

$$R_{\text{tot}} = f(Q, \Delta T, t, A, P_c) \tag{5}$$

The main uncertainty in these experiments is due to errors in determining the heat flux through the sample which leads to

Table 1
Uncertainty of involving parameters in the analysis.

$\delta Q/Q$	$\delta\,\Delta T/\Delta T$	$\delta t/t$	$\delta A/A$	$\delta P_c/P_c$
4.3%	1.3%	2.7%	1.6%	2.5%

a maximum error of 4.3%. The maximum uncertainties for the thermocouples and the data acquisition readings are ±1 °C which introduces a maximum error of 1.3% between the interfaces of the sample and fluxmeters. Other uncertainties including those associated with the load cell, thickness, and cross-sectional area measurements and are listed in Table 1. The maximum uncertainty for the thermal resistance measurements can be calculated from [23]:

$$\frac{\delta R_{\text{tot}}}{R_{\text{tot}}} = \sqrt{\left(\frac{\delta Q}{Q}\right)^2 + \left(\frac{\delta \Delta T}{\Delta T}\right)^2 + \left(\frac{\delta t}{t}\right)^2 + \left(\frac{\delta A}{A}\right)^2 + \left(\frac{\delta P_c}{P_c}\right)^2} \quad (6)$$

For the present study, the maximum uncertainty is estimated to be ±6%.

3. Analytical study

3.1. Thermal conductivity model

To determine the through-plane effective thermal conductivity of fibrous GDL, a unit cell approach is employed [11]. The goal of this approach is to model the random and anisotropic structure of GDL with a relatively simple geometry which can predict the effective thermal conductivity accurately. The proposed geometrical model is shown in Fig. 4 and consists of uniformly sized equally spaced cylindrical fibers immersed in stagnant air. The fibers angle, θ, can be varied in this model.

Although the fibers are randomly oriented in practice, the averaged effect of this randomness on the transport properties of a sample is well represented by n unit cells with an orthogonal arrangement as shown in Sadeghi et al. [11] comparison of model predictions and experiments; this is corroborated by the recent results of Van Doormaal and Pharoah [24]. Thus, in the present study, the orthogonal and square arrangement of fibers is considered. The micro-structure of carbon papers is deformed non-linearly with the compressive load as shown in Fig. 3. This non-linear deformation is a complex combination of elastic and plastic deformations and slippage and breakage of fibers, binders, and PTFE which is clear in Fig. 5. We modeled this deformation as a combination of elastic deformation and slipping of fibers. A schematic of the deformation of the unit cell under the load is shown in Fig. 6. The total thickness reduction is the summation of elastic deformation and thickness variation as a result of fiber slippage.

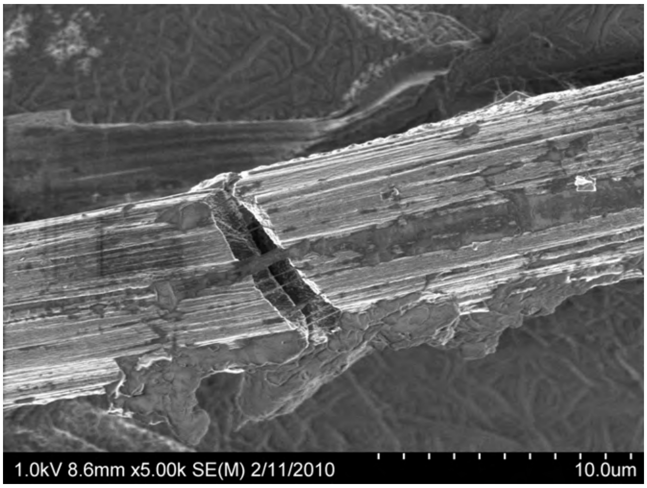

Fig. 5. SEM image of a broken TGP-H-120 fiber after compression, ×5000 magnification.

$$\delta_{\text{tot}} = \delta_s + \delta_e = \epsilon \cdot d \quad (7)$$

where d is the mean diameter of fibers and δ_e and δ_s are the thickness reductions as a result of elastic deformation and fiber slippage, respectively. The deformation of the carbon paper under the load shown in Fig. 3 is correlated by

$$\varepsilon = \frac{\Delta t}{t_0} = \begin{cases} 0.274[1-\exp(-0.988P_c^*)] : \text{TGP-H-120} \\ 0.449[1-\exp(-1.063P_c^*)] : \text{TGP-H-060} \end{cases} \quad (8)$$

where P_c^* is the contact pressure in MPa non-dimensionalized with respect to the reference pressure $P_0 = 1$ MPa.

To find the contact area between fibers, the Hertzian contact theory [7] is applied. Based on this theory, when a cylindrical fiber

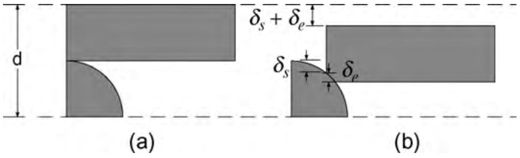

Fig. 6. Contacting fibers in the unit cell: (a) before compression and (b) after compression.

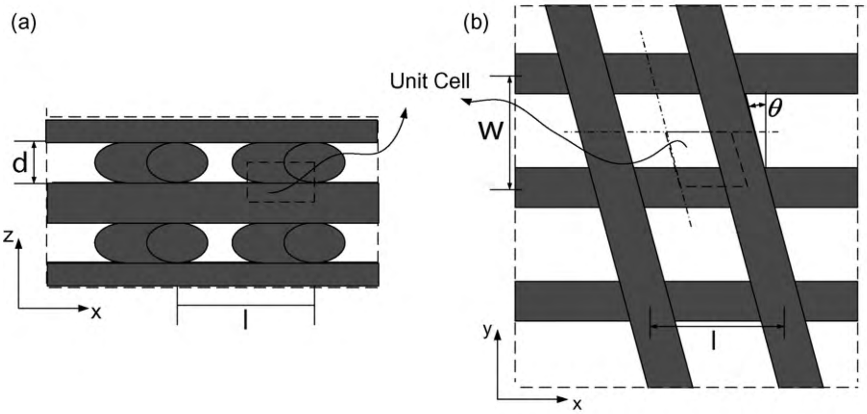

Fig. 4. Geometrical model of GDL: (a) front view and (b) top view [10].

contacts another cylindrical fiber eccentrically, as is the case here, the contact spot is close to an ellipse and the relation between the elastic deformation δ_e and the load F can be expressed approximately in the terms of deformations as [7]:

$$F = \frac{4}{3} E^* R_e^{1/2} \delta_e^{3/2} \tag{9}$$

where R_e is the equivalent radius of the principal radii of curvature of two contacting bodies which is equal to the average fiber radius for the present study. E^* is the effective Young's modulus which can be defined as a function of Young's modulus and Poisson's ratio of two contacting bodies [7].

$$E^* = \left(\frac{1-\nu_1{}^2}{E_1} + \frac{1-\nu_2{}^2}{E_2} \right)^{-1} \tag{10}$$

The major and minor radii of the contact area can be found from the geometrical relations of the deformed unit cell shown in Fig. 6(b).

$$a = \sqrt{r^2 - (r-\delta_e)^2} \tag{11}$$

$$b = \sqrt{r^2 - (r-\delta_e-\lambda)^2} - \sqrt{r^2-(r-\lambda)^2} \tag{12}$$

where λ is the onset of elastic deformation, the thickness variation before the start of the elastic deformation. Through a comparison with experimental data, λ is found to be $\delta_s/60$ and $\delta_s/15$ for TGP-H-060 and TGP-H-120, respectively. Comparison of different thermal resistances against the heat transfer in the unit cell indicates that the constriction/spreading resistance R_{sp} is the controlling resistance [11]. Thus to develop a compact model, the contributions of other resistances can be neglected. When heat flows in/out of a body through a small area, the heat flux lines are correspondingly constricted/spread apart and the resulting thermal resistance is referred to as constriction/spreading resistance. The spreading resistance can be approximated by the solution of an elliptical heat source on a circular flux tube given by [25]:

$$R_{sp} = \frac{1.6974}{\pi^2 k_s b} \psi(\alpha) \cdot \kappa \left(1 - \frac{a^2}{b^2} \right) \tag{13}$$

where $\psi(\alpha)$ is the constriction parameter which can be expressed as [26]:

$$\psi(\alpha) = (1-\alpha)^{1.5} \tag{14}$$

where α is the ratio of the contact size to the fiber radius, $\alpha = \sqrt{ab}/r$. $\kappa(\cdot)$ is the complete elliptic integral of the first kind defined as

$$\kappa\left(1-\frac{a^2}{b^2}\right) = \int_0^{\pi/2} \frac{dt}{\sqrt{1-(1-(a^2/b^2))\sin^2 t}} \tag{15}$$

The effective thermal conductivity of GDL can be found through the relationship between the total thermal resistance and the effective thermal conductivity:

$$k_{eff} = \frac{t_{uc}}{R_{tot} A_{uc}} = \frac{d(1-\varepsilon)}{2 R_{sp} A_{uc}} \tag{16}$$

where t_{uc} is the thickness of the unit cell under compression and A_{uc} is the cross-sectional area of the unit cell with the width of $w/2$, $A_{uc} = w^2/4$.

3.2. Thermal contact resistance model

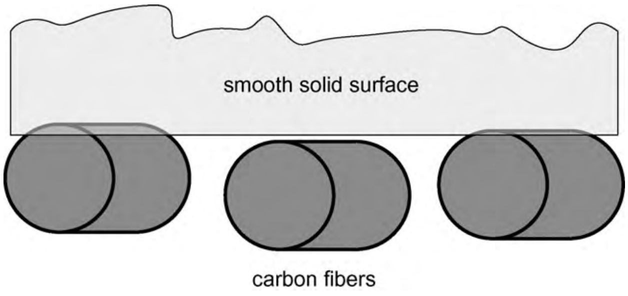

Fig. 7. GDL fibers in contact with a smooth solid surface.

All surfaces are inherently rough and the actual contact area consists of microscopic scale interfaces between asperities of the two contacting bodies. Therefore, the topologies of both contacting surface are important in understanding their interfacial behavior [18]. To verify our experimental data for *TCR*, an analytical model is developed using the Greenwood and Williamson statistical model [27]. This model is based on the Hertz solution for individual elastic contacts and assumes that only asperities originally higher than the separation of the surfaces are in contact. Also, the model only considers the solid microcontacts corresponding to the vacuum condition.

The surface roughness of the fluxmeters and carbon papers are measured using a Mitutoyo profilometer. The average roughness for the fluxmeters is less than 1 μm which is insignificant compared to the average pore size and fiber diameter, and therefore these surfaces can hence be considered smooth. A schematic of the contact between a smooth solid surface and carbon fibers of GDL in Fig. 7 shows that only a small portion of the solid surface is in contact with the fibers.

For carbon papers with high porosity and a random fiber distribution on the surface, it is complicated to define roughness parameters. In this study, we assumed that the carbon paper surface acts as a rough solid surface and we determined the roughness parameters through profilometry. The measured parameters, averaged data for TGP-H-120 and TGP-H-060, are shown in Table 2. The asperity radius is assumed to be equal to the average fiber radius, $R_p = r = 4.25$ μm.

The total contact force can be found by [27]:

$$F = P_c A_0 = N \int_h^\infty \frac{4}{3} E^* R_e^{1/2} (z-h)^{3/2} \phi(z) dz \tag{17}$$

where N is the total number of contact points and h is the separation of the surfaces. P_c and A_0 are the contact pressure and the nominal contact area, respectively. $\phi(z)$ is the normal distribution of the surface height which can be described as

$$\phi(z) = \frac{1}{\sigma\sqrt{2\pi}} \exp\left(-\frac{z^2}{2\sigma^2}\right) \tag{18}$$

where σ is the root mean square of the surface roughness. Since the deformation of GDL under compression is significant, a portion of the force F is absorbed for the thickness reduction. To find the actual contact area, the thickness reduction of the unit cell close to the contact surface should be subtracted from the total deformation. The radius of a contact spot at the distance z from the separation line of the contacting surfaces can be expressed as [7]:

$$a(z) = \sqrt{(z-h-\epsilon\delta)R_p} \tag{19}$$

The contact resistance of this contact spot can be written as the summation of the constriction resistance in the fluxmeter and the

Table 2
Input data for *TCR* modeling of Toray carbon papers.

σ (μm)	D_{peak} (mm^{-1})	E_c (GPa)	E_{f1} (GPa)	K_c (W m^{-1} K^{-1})	k_{fl} (W m^{-1} K^{-1})
8.96	12.6	3.2	210	120	66

spreading resistance in the adjunct carbon fiber.

$$R(z) = \frac{1}{4k_{\mathrm{fl}}a(z)} + \frac{1}{4k_{\mathrm{c}}a(z)} \tag{20}$$

Therefore, the total contact resistance can be expressed as the parallel combination of all contact spots.

$$TCR = \left(\frac{2Nk_{\mathrm{fl}}k_{\mathrm{c}} \int_{h+\varepsilon d}^{\infty} \sqrt{(z-h-\varepsilon d)R_{\mathrm{p}}}\,\phi(z)dz}{k_{\mathrm{fl}}+k_{\mathrm{c}}} \right)^{-1} \tag{21}$$

where k_{fl} and k_{c} are the thermal conductivities of the fluxmeters and the carbon fiber, respectively. For more convenience in evaluating integrals and performing parametric studies, a code was written in Fortran for the *TCR* and effective thermal conductivity modeling.

4. Results and discussion

The measurements were taken at different compressive loads in a vacuum as well as under ambient pressure condition to study the effects of the compressive load and the contribution of heat conduction in air on *TCR* and effective thermal conductivity.

Fig. 8(a) shows the temperature variation along the test column (upper and lower fluxmeters) for TGP-H-120 Toray carbon paper at atmospheric pressure. As expected, the temperature variation is linear along the column; the small difference in the upper and the lower fluxmeters slopes is a result of the temperature difference, since the fluxmeters thermal conductivity is a function of temperature. Perfect thermal insulation (adiabatic conditions) cannot be achieved in practice and small thermal losses occur to the test structure and the surroundings as shown by the relative difference in heat transfer rates for the upper and lower fluxmeters in Fig. 8(b) at various compressive loads. The maximum difference is 4.1% at low pressures, decreasing to 1.4% for higher contact pressures.

The effective thermal conductivity values at different contact pressures are compared with the analytical model, Eq. (16), in Fig. 9 for vacuum and atmospheric pressure conditions. The effective conductivity increases with an increase in the compressive load due to larger size and number of contacts between the fibers. The manufacturer's effective thermal conductivity of 1.7 W m^{-1} K^{-1} differs by 4.4% from our result at a relatively low pressure of 0.478 MPa. A small difference (less than 3%) can be observed between thermal conductivity values obtained under atmospheric and vacuum conditions, indicating that the air trapped in gaps/pockets of the medium provide an additional, but relatively ineffective path for heat conduction. Comparison of the model predictions and experimental data shows good agreement for both vacuum and atmospheric pressure conditions and over a wide range of compressive loads.

Fig. 10 shows the thermal contact resistance of both types of Toray carbon papers under different compressive loads. Again, the present analytical model for *TCR* under vacuum condition, Eq. (21), correlates very satisfactorily (within 15%) with the experimental data.

Since air fills the gaps between the contact surfaces and provides another path for heat conduction across the contact interface, the thermal contact resistance and consequently the total thermal resistance decrease. This reduction is less pronounced at higher contact pressures when the contact area increases providing preferential thermal paths. Under both ambient and vacuum conditions, *TCR* decreases with an increase in compressive load due to the increased contact area. It should also be noted that increasing compression beyond a certain level induces fiber breakage and irreversible deformations [28]; this results in hysteresis effects under cyclic loads. These hysteresis effects will be studied in-depth in Part 2 of this study.

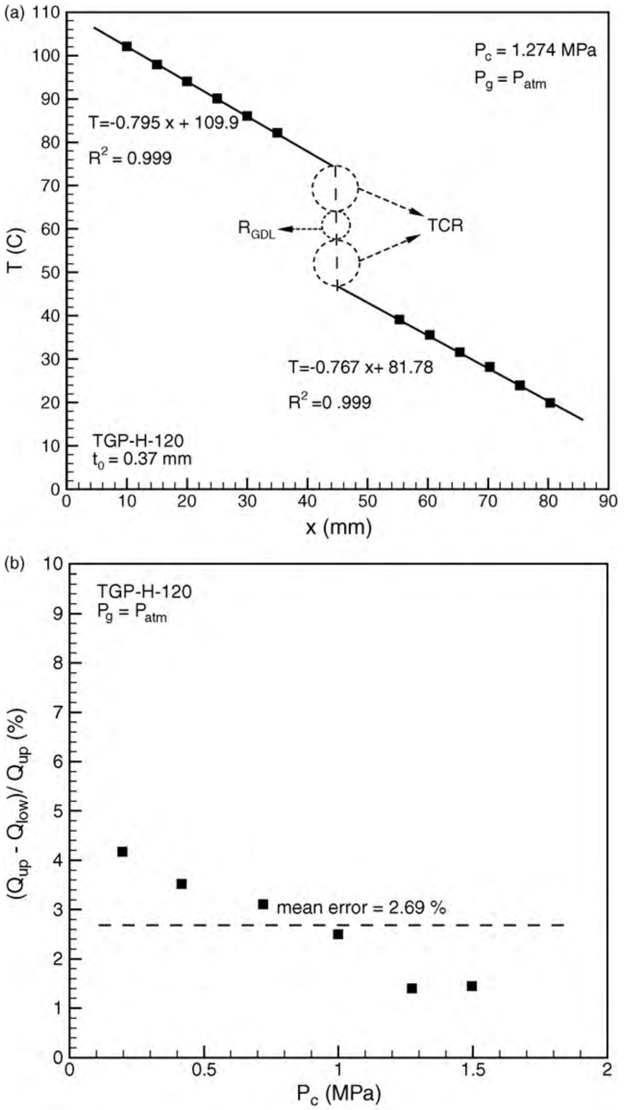

Fig. 8. (a) Temperature distribution along the test column; (b) relative difference in the heat flux passing through the upper and the lower fluxmeters.

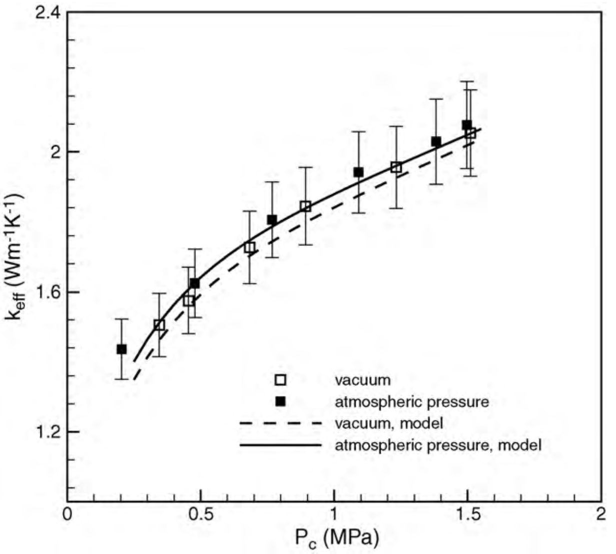

Fig. 9. Effective thermal conductivity of the Toray carbon papers at vacuum and atmospheric pressures: experimental data and model.

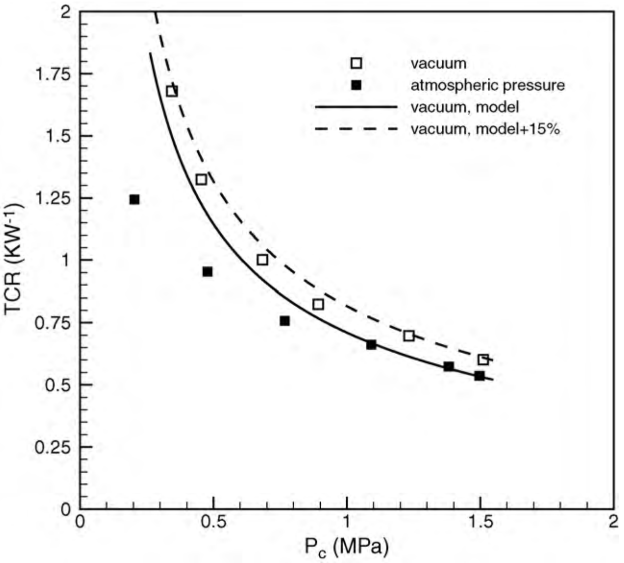

Fig. 10. Comparison of thermal contact resistance at vacuum and atmospheric pressure.

Fig. 11 shows the *TCR* to total resistance ratio as a function of compression, and we observe that:

- *TCR* is clearly the dominant resistance, contributing between 65 and 90% of the total resistance.
- As expected, the relative contribution of *TCR* is more important for thinner materials; the average *TCR* ratio for TGP-H-120 and TGP-H-060 at atmospheric pressure is 68% and 82%, respectively.

Both thermal conductivity and *TCR* decrease with increasing compression; however, as shown in Fig. 11, the *TCR* to total resistance ratio remains approximately constant.

The variations of the total thermal resistance and of the effective thermal conductivity with temperature are shown in Fig. 12 for TGP-H-120 sample subjected to a constant contact pressure of 0.75 MPa. The effective thermal conductivity decreases slightly with increasing temperature, while the total resistance remains approximately constant. Considering that the *TCR* is the controlling component of the total resistance, we can conclude that the *TCR* does not depend on temperature, at least in the range of temperatures considered here.

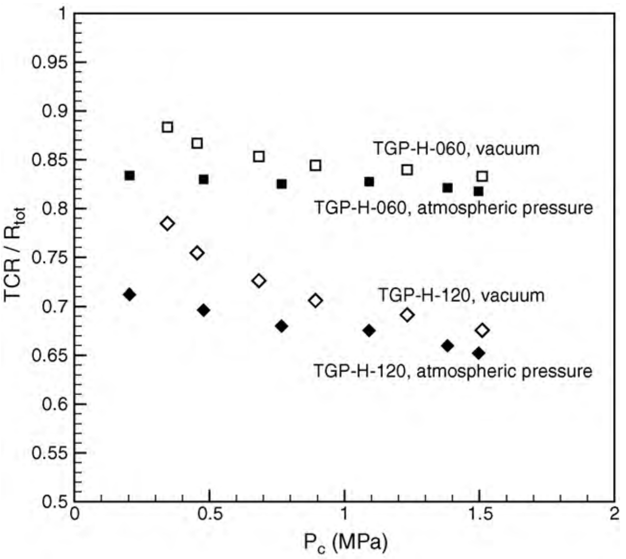

Fig. 11. Thermal contact resistance to total resistance ratio at different pressures.

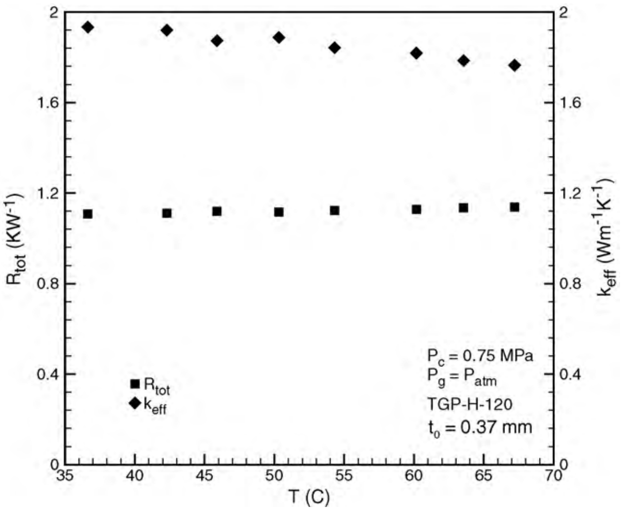

Fig. 12. Effect of operation temperature on the total thermal resistance.

The reduction in thermal conductivity can be attributed to the presence of carbonized thermo-setting resins used as a binder in GDLs [29]. The thermal conductivity of these thermo-setting polymers decreases with increasing temperature [30], and this would result in a reduction in the effective thermal conductivity of the medium.

5. Summary and conclusions

A test bed was designed and built and analytic models were developed to measure and predict thermal conductivity and thermal contact resistance of GDLs under various compressive loads. The model predictions are in good agreement with experimental data over a wide range of compressive loads from 0.2 to 1.5 MPa. Parametric studies performed to investigate the trends and effects of compression, conduction in air, and operating temperature show that the effective thermal conductivity increases with the compressive load and decreases with an increase with operating temperature, but that it is relatively insensitive to ambient air pressure. An important finding is the dominant contribution of thermal contact resistance to the total thermal resistance. The ratio of thermal contact to bulk GDL resistance remains approximately constant, e.g. (4.6/1) for TGP-H-060 at atmospheric pressure over a range of conditions.

This work has helped clarify the impact of several operational parameters on the thermal properties of GDLs and provided new insights on the importance of a key interfacial phenomenon. Further work will be required to investigate the effect of cycling changes in conditions encountered in operating fuel cell stacks, and to extend the measurements and theoretical analysis to other MEA interfaces, such as that between the micro-porous layer and the GDL.

Acknowledgements

The authors are grateful for the financial support of the Natural Sciences and Engineering Research Council (NSERC) of Canada, and the Canada Research Chairs Program.

References

[1] N. Djilali, D. Lu, Int. J. Therm. Sci. 41 (2002) 29–40.
[2] T. Berning, N. Djilali, J. Electrochem. Soc. 150 (2003) A1589–A1598.

[3] S. He, M.M. Mench, S. Tadigadapa, Sens. Actuators A: Phys. 125 (2006) 170–177.
[4] P.J.S. Vie, S. Kjelstrup, Electrochim. Acta 49 (2004) 1069–1077.
[5] A. Kusoglu, Y. Tang, M.H. Santare, A.M. Karlsson, S. Cleghorn, W.B. Johnson, J. Fuel Cell Sci. Technol. 6 (2009) 011012–011019.
[6] A. Kusoglu, A.M. Karlsson, M.H. Santare, S. Cleghorn, W.B. Johnson, J. Power Sources 161 (2006) 987–996.
[7] K.L. Johnson, Contact Mechanics, Cambridge Univ. Press, London, UK, 1985, Ch. 4, 13.
[8] J. Ramousse, S. Didierjean, P. Lottin, D. Maillet, Int. J. Therm. Sci. 47 (2008) 1–6.
[9] A. Hakenjos, H. Muenter, U. Wittstadt, C. Hebling, J. Power Sources 131 (2004) 213–216.
[10] F. Danes, J.P. Bardon, Revue Générale de Thermique 36 (1997) 302–311.
[11] E. Sadeghi, M. Bahrami, N. Djilali, J. Power Sources 179 (2008) 200–208.
[12] J. Becker, V. Schulz, A. Wiegmann, J. Fuel Cell Sci. Technol. 5 (2008) 21006–21015.
[13] M. Wang, J. He, J. Yu, N. Pan, Int. J. Therm. Sci. 46 (2007) 848–855.
[14] M. Khandelwal, M.M. Mench, J. Power Sources 161 (2006) 1106–1115.
[15] I. Nitta, O. Himanen, M. Mikkola, Fuel Cells 08 (2008) 111–119.
[16] O. Burheim, P.J.S. Vi, J.G. Pharoah, S. Kjelstrup, J. Power Sources 195 (2010) 249–256.
[17] V. Mishra, F. Yang, R. Pitchumani, J. Fuel Cell Sci. Technol. 1 (2004) 2–9.
[18] Y. Zhou, G. Lin, A.J. Shih, S.J. Hu, J. Power Sources 163 (2007) 777–783.
[19] Z. Wu, S. Wang, L. Zhang, S.J. Hu, J. Power Sources 189 (2009) 1066–1073.
[20] T. Swamy, E.C. Kumbar, M.M. Mench, J. Electrochem. Soc. 157 (2010) B77–B85.
[21] S. Escribano, J.-F. Blachot, J. Etheve, A. Morin, R. Mosdale, J. Power Sources 156 (2006) 8–13.
[22] V.S. Arpaci, P.S. Larsen, Convection Heat Transfer, Prentice-Hall, Englewood Cliffs, NJ, 1984, Ch. 4.
[23] J.R. Taylor, An Introduction to Error Analysis: The Study of Uncertainties in Physical Measurements, second ed., University Science Books, Sausalito, US, 1997, Ch. 3.
[24] M.A. Van Doormaal, J.G. Pharoah, Int. J. Numer. Meth. Fluids 59 (2009) 75–89.
[25] M.M. Yovanovich, Progr. Astronaut. Aeronaut.: Radiat. Trans. Therm. Control 49 (1976) 397–418.
[26] M.G. Cooper, B.B. Mikic, M.M. Yovanovich, Int. J. Heat Mass Trans. 12 (1969) 279–300.
[27] J.A. Greenwood, B.P. Williamson, Proc. R. Soc. London: Ser. A: Math. Phys. Sci. 295 (1966) 300–319.
[28] A. Bazylak, D. Sinton, Z.-S. Liu, N. Djilali, J. Power Sources 163 (2007) 784–792.
[29] M.F. Mathias, J. Roth, J. Fleming, W. Lehnert, in: W. Vielstich, H.A. Gasteiger, A. Lamm (Eds.), Handbook of Fuel Cells-Fundamental, Technology and Application, vol. 3, John Wiley & Sons, Ltd., 2003, pp. 517–537.

Books, Sausalito, US, 1997, Ch. 3.
[24] M.A. Van Doormaal, J.G. Pharoah, Int. J. Numer. Meth. Fluids 59 (2009) 75–89.
[25] M.M. Yovanovich, Progr. Astronaut. Aeronaut.: Radiat. Trans. Therm. Control 49 (1976) 397–418.
[26] M.G. Cooper, B.B. Mikic, M.M. Yovanovich, Int. J. Heat Mass Trans. 12 (1969) 279–300.
[27] J.A. Greenwood, B.P. Williamson, Proc. R. Soc. London: Ser. A: Math. Phys. Sci. 295 (1966) 300–319.
[28] A. Bazylak, D. Sinton, Z.-S. Liu, N. Djilali, J. Power Sources 163 (2007) 784–792.
[29] M.F. Mathias, J. Roth, J. Fleming, W. Lehnert, in: W. Vielstich, H.A. Gasteiger, A. Lamm (Eds.), Handbook of Fuel Cells-Fundamental, Technology and Application, vol. 3, John Wiley & Sons, Ltd., 2003, pp. 517–537.

[30] C.L. Choy, Y.W. Wong, G.W. Yang, T. Kanamoto, J. Polym. Sci.: Polym. Phys. 37 (1999) 3359–3367.

Appendix E

Effective Thermal Conductivity and Thermal Contact Resistance of Gas Diffusion Layers in PEM Fuel Cells. Part 2: Hysteresis Effect under Cyclic Compressive Load

Reproduced by permission of Elsevier

Journal of Power Sources 195 (2010) 8104–8109

Contents lists available at ScienceDirect

Journal of Power Sources

journal homepage: www.elsevier.com/locate/jpowsour

Effective thermal conductivity and thermal contact resistance of gas diffusion layers in proton exchange membrane fuel cells. Part 2: Hysteresis effect under cyclic compressive load

E. Sadeghi[a,b,*], N. Djilali[a], M. Bahrami[b]

[a] Dept. Mechanical Eng., and Institute for Integrated Energy Systems, University of Victoria, P.O. Box 3055, Victoria, BC, Canada V8W 3P6
[b] Mechatronic Systems Engineering, School of Engineering Science, Simon Fraser University, Surrey, BC, Canada V3T 0A3

ARTICLE INFO

Article history:
Received 15 July 2010
Accepted 19 July 2010
Available online 22 July 2010

Keywords:
Hysteresis
Cyclic compression
TCR
Effective thermal conductivity
Heat transfer

ABSTRACT

Heat transfer through the gas diffusion layer (GDL) is a key process in the design and operation of a PEM fuel cell. The analysis of this process requires the determination of the effective thermal conductivity as well as the thermal contact resistance between the GDL and adjacent surfaces/layers. The Part 1 companion paper describes an experimental procedure and a test bed devised to allow separation of the effective thermal conductivity and thermal contact resistance, and presents measurements under a range of static compressive loads. In practice, during operation of a fuel cell stack, the compressive load on the GDL changes.

In the present study, experiments are performed on Toray carbon papers with 78% porosity and 5% PTFE under a *cyclic* compressive load. Results show a significant hysteresis in the loading and unloading cycle data for total thermal resistance, thermal contact resistance (TCR), effective thermal conductivity, thickness, and porosity. It is found that after 5 loading-unloading cycles, the geometrical, mechanical, and thermal parameters reach a "steady-state" condition and remain unchanged. A key finding of this study is that the TCR is the dominant component of the GDL total thermal resistance with a significant hysteresis resulting in up to a 34% difference between the loading and unloading cycle data. This work aims to clarify the impact of unsteady/cyclic compression on the thermal and structural properties of GDLs and provides new insights on the importance of TCR which is a critical interfacial transport phenomenon.

1. Introduction

Commercialization of PEM fuel cells requires further progress in improving operational lifetime [1]. A number of degradation mechanisms need to be better understood, including those associated with the deterioration of the gas diffusion layer (GDL) due to mechanical stresses. In the companion paper [2] the effects of *constant* compressive loads representative of the clamping of a stack were investigated for GDLs. In practice, the GDL as well as other components, including the membrane and catalyst layer, will be subjected to additional hygro-thermal stresses that arise due to varying temperature and relative humidity during operation, and that are *cyclic* in nature. These stresses induce material degradation and compromise performance and lifetime [3,4]. The variation in the compressive load affects all the transport phenomena and consequently the performance of the entire system. In addition, servicing and/or reconditioning that involves unclamping and opening of a stack may be required on a number of occasions over the course of the operational lifetime of the stack, resulting in another type of cyclic compression. The effects of cyclic compression on the fuel cell components need to be examined and better understood.

The focus in this study is on the GDL which provides five key functions in a PEM fuel cell: (1) mechanical support, (2) electronic conductivity, (3) heat removal, (4) reactant access to catalyst layers, and (5) product removal [5]. Thus, accurate knowledge of the mechanical and thermal characteristics of GDLs under different compressive loads is required to determine related transport phenomena such as water and species transport, reaction kinetics, and the rate of phase change.

Several studies are available on the effects of steady-state compression on fuel cell components and performance; however, the effects of cyclic compression have not been studied in-depth. Rama et al. [1] presented a review of the causes and effects of performance degradation and failure in various components of PEM fuel cells. They reported that over-compression and inhomogeneous compression of GDLs induced during stack assembly or during operation reduce the porosity, hydrophobicity, and gas permeabil-

---

* Corresponding author at: Dept. Mechanical Eng., and Institute for Integrated Energy Systems, University of Victoria, P.O. Box 3055, Victoria, BC, Canada V8W 3P6. Tel.: +1 7787828587; fax: +1 2507216051.
E-mail address: ehsans@uvic.ca (E. Sadeghi).

0378-7753/$ – see front matter © 2010 Elsevier B.V. All rights reserved.
doi:10.1016/j.jpowsour.2010.07.051

ity. This increases the tendency for flooding in GDLs, which results in an increase in mass transport losses.

Kleemann et al. [6] investigated the local compression distribution in the GDL and the associated effect on material electrical resistance and electrical contact resistance. They also measured the mechanical properties of fibrous paper and non-woven GDLs. The mechanical properties included Young's modulus, the shear modulus, and Poisson's ratio for in-plane and through-plane directions. They found that the combined value of the through-plane resistance and of the contact resistance with the microporous layer and catalyst layer is highly compression dependent and increases sharply at low compression pressures.

Escribano et al. [7] measured the thickness reduction of different types of GDLs including cloth, felt, and paper for the first and second loading over a range of compressive loads. They reported differences between the thickness data; the thickness values for the second loading were smaller and their variation over the range of compressions was smoother.

Zhou et al. [8] studied the effect of the clamping force on the electrical contact resistance and the porosity of the GDL using a finite element method. They assumed the GDL to be a porous elastic material and reported that after stack loading, the porosity was not uniform and that its minimum occurred in the middle of flow-field plate rib.

Bazylak et al. [9] used scanning electron microscopy (SEM) to investigate the effect of compression on the morphology of the GDL. They reported that the damage to the GDL is non-uniform under a small compression which was attributed to the surface roughness. However, as the compression pressure is increased, the damage was found to be more isotropic over the entire sample [9]. Bazylak et al. [9] experimentally showed that compressing the GDL causes a breakup of fibers and a deterioration of the PTFE coating.

Several studies used a guarded-hot-plate apparatus to measure the effective thermal conductivity and TCR of GDLs under different pressures [2,10–12]. Nitta et al. [10] argued that the effective thermal conductivity is independent of compression but Burheim et al. [11] reported that the effective thermal conductivity increases with compressive load; however, both studies showed that TCR, decreases with an increase in the compressive load. In the companion Part 1 of this study [2] we showed that the effective thermal conductivity increases with compression due to an increase in the number and size of contact spots. Khandelwal and Mench [12] investigated the effect of load cycling on the TCR between the GDL and an aluminum bronze material as well as the total resistance of the GDL by compressing the sample to 2 MPa and then releasing it for a single cycle. They found that the measured total resistance and TCR differed by 20% and 38%, respectively between the loading and unloading phases.

Although the studies available on the effect of compression-release on GDL properties are limited, numerous investigations have been performed in textile engineering that are relevant to the fibrous structure of GDLs. The first theoretical model in this field was proposed by van Wyk [13,14] in 1946 to explain the compression behavior of fiber assemblies with random orientations. van Wyk [13,14] assumed that the compression of a fibrous assembly increases the number of fiber–fiber contact points leading to individual fibers becoming bent between these contact points. He found a linear relationship between the pressure and the cube of the fiber volume fraction. van Wyk's relationship is a classical model in textile engineering, however, it does not account for fiber slippage and friction during compression. Also, it does not explain the non-recoverable strain during compression and the mechanical hysteresis during compression-release cycling. Recent studies [15–20] have focused on accounting for the fiber slippage and the hysteresis observed during compression-release cycling. The cycling induces energy dissipation as a result of viscous damping or frictional losses. An approach taken to model the hysteresis behavior of fibrous media is to consider the structure as a combination of series and parallel springs, dashpots, and Coulomb frictional element [15,16]. Dunlop [15] used such a model to perform simulation that yield a hysteresis loop with a shape similar to the experimental data, but no model verification was performed. Also, the viscoelastic nature of fibers was not considered. The compression hysteresis was theoretically modeled and verified against experimental data in [17–19] by applying the force, angular momentum, and bending equations to fiber assemblies. These models [17–19] reproduced the experimentally observed trends correctly but the values are different. Also, the hysteresis effect was independent of the number of load cycles as a result of neglecting the viscoelastic behavior of the fibers. Stankovic [20] measured the strain of different fabrics including hemp, cotton, viscous, and acrylic fabrics under compression-release cycles and observed a hysteresis in the stress–strain curve. He [20] reported that the hysteresis becomes smaller with repeated load cycling, and approaches zero at the 5th cycle.

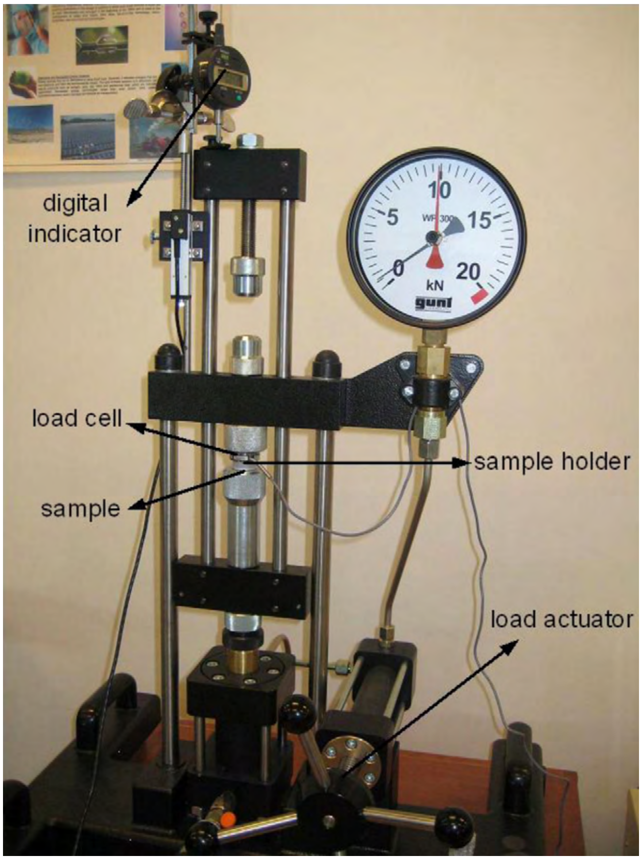

Fig. 1. Experimental apparatus used for thickness measurement.

Our literature review shows that the majority of the available studies have focused on the effect of steady-state compression on the structure and properties of GDLs; even though, cyclic compression occurs during the operation and lifecycle of a PEM fuel cell stack. The present study contributes to addressing this gap through a systematic investigation of the effects of cyclic compression on the GDL thermal and structural properties.

A test bed was designed and built to enable the measurement of thermal conductivity and TCR of porous media. The test bed was equipped with a loading mechanism that allows the application of various compressive loads on GDLs. Also, a tensile- compression apparatus is used to measure the thickness variation of GDLs under compression. Toray carbon papers with a porosity of 78% and

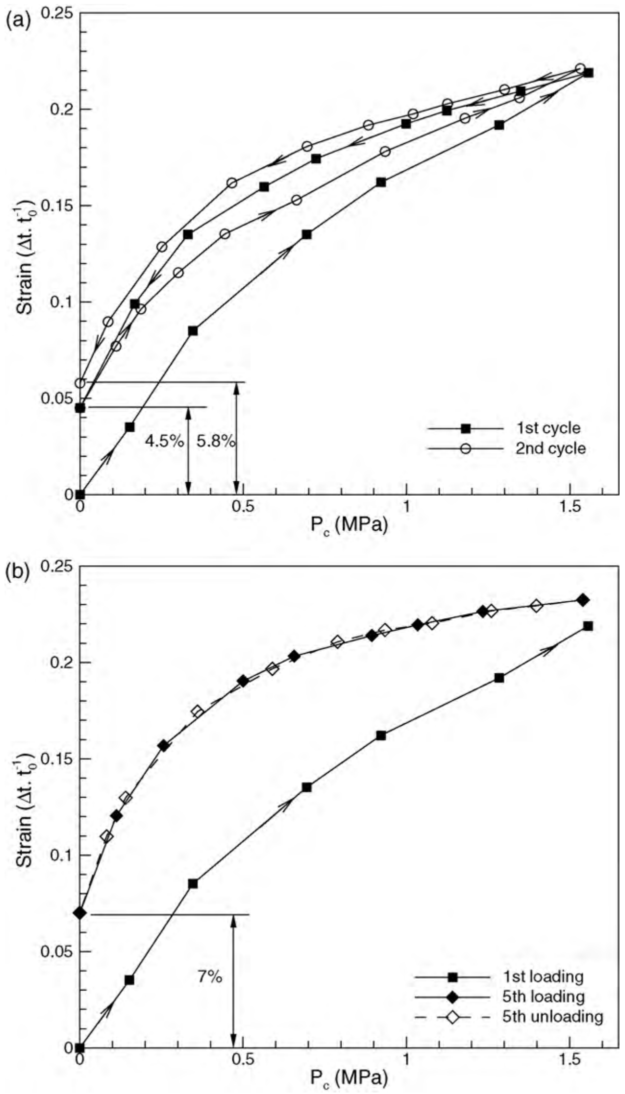

Fig. 2. Hysteresis in thickness variation of Toray carbon paper, 78% porosity and 5% PTFE, under cyclic compressive loads: (a) comparison of 1st and 2nd cycles; (b) comparison of 1st loading and 5th unloading.

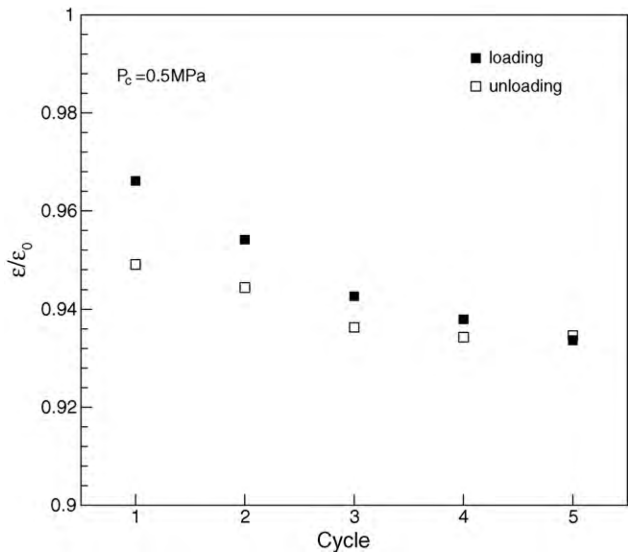

Fig. 3. Normalized porosity at different loading–unloading cycles, $P_c = 0.5$ MPa.

5% PTFE content are used in the experiments. The effects of cyclic compression on the effective thermal conductivity, total thermal resistance, TCR, thickness and porosity of the GDL are investigated under vacuum condition. The load cycling in the experiments is continued until the loading and unloading data coincide. As we show later, this occurs at the 5th cycle for all properties. The compression-release curve of the thermal and structural properties is presented and the hysteresis observed in their behavior is explained.

2. Experimental study

The experimental apparatus for the thermal tests is a custom-made test bed designed for thermal conductivity and TCR measurements under vacuum and ambient pressure conditions and is described in detail in Part 1 [2]. Toray carbon paper TGP-H-120 with a porosity of 78%, 5% wet proofing, and an initial thickness of 0.37 mm was used in the mechanical and thermal experiments under cyclic compression. The apparatus used to monitor the sample thickness is shown in Fig. 1.

Thermal experiments were conducted under vacuum condition. A vacuum level of 10^{-5} mbar was achieved under the test chamber using the vacuum machine. Cyclic compressive loads were applied to the sample continuously while simultaneously recording temperature and pressure at each load of the loading and unloading paths when steady-state conditions were achieved. The compression-release cycling was continued until no significant hysteresis effects were observed in loading-unloading curves; as discussed later, this happens at the 5th cycle.

The thickness of the GDL sample under the cyclic compressive load was measured separately using the tensile-compression apparatus shown in Fig. 1. The loading was stopped at the end of the 5th cycle when the difference between the loading and unloading paths became negligible. More details on the test procedure and data reduction of the thermal and mechanical experiments are provided in Part 1 of this study [2].

3. Results and discussion

Fig. 2 shows the thickness variation of the Toray carbon paper TGP-H-120 under cyclic compressive load. The thickness reduction is more significant at the beginning of the loading and as the pressure increases, the slope of thickness variation decreases. Since the micro-structure becomes more packed, its resistance to deformation under the load is higher. During unloading a number of deformed, slipped or broken fibers do not return to their original state; this results in a difference between the loading and unloading paths, creating the compression hysteresis. When the cyclic compression is repeated, the hysteresis effect becomes smaller, and the deformation reaches a steady-state. The variation in hysteresis may be a result of the viscoelastic behavior of the GDL fibers [16–20]. The difference between the unloaded and fresh samples is 4.5% for the first cycle. The difference gradually increases with each subsequent cycle, and reaches 7% at the 5th cycle and remains unchanged afterward. This result is consistent with the experimental data of Stankovic [20] which shows no change in the stress–strain curve after the 5th cycle for a variety of fabrics. The variation of the normalized porosity (i.e. the ratio of compressed to fresh GDL porosities) at different loading–unloading cycles is shown in Fig. 3 for a typical compressive load of 0.5 MPa. As shown, the porosity decreases as the number of cycles increases; this is a direct result of more permanent (irreversible) deformations in the micro-structure. We note that the difference between the porosity values of the loading and unloading paths decreases with continuing load cycling and becomes negligible at the 5th cycle.

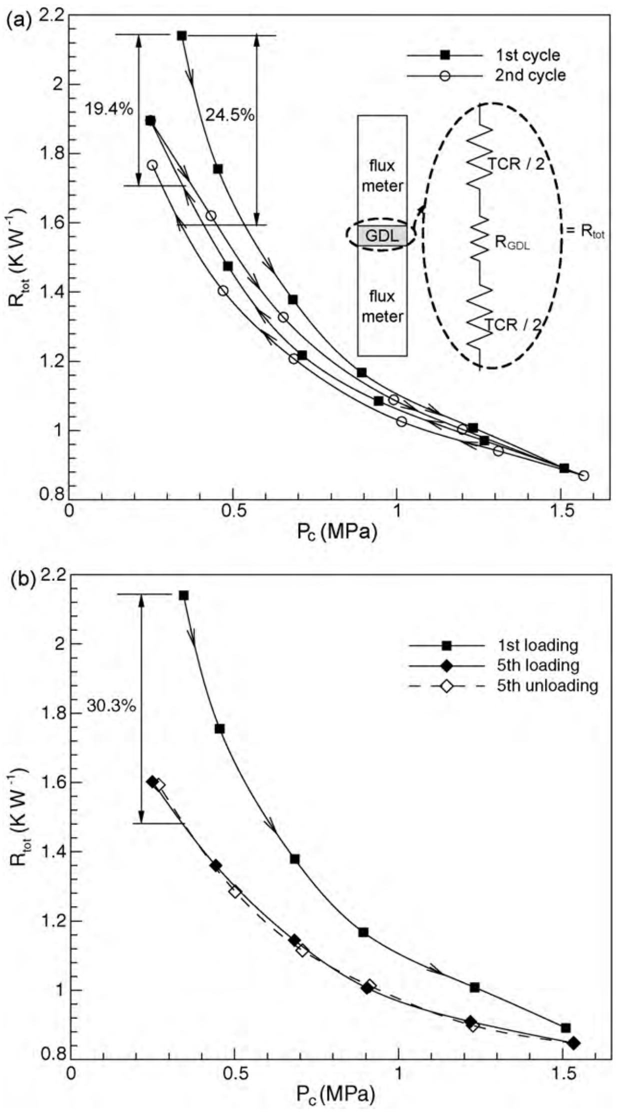

Fig. 4. Hysteresis in total thermal resistance under cyclic compressive load: (a) comparison of 1st and 2nd cycles; (b) comparison of 1st loading and 5th unloading.

The impact of cyclic compressive load on the total thermal resistance of the GDL sample under vacuum condition is shown in Fig. 4. The total resistance decreases with an increase in compressive load due to the increased contact area between the GDL fibers as well as at the interface between the GDL and the fluxmeters surfaces. Increasing compression causes fiber breakage, irreversible deformations, and fiber slippage resulting in a hysteresis behavior in the total resistance of the unloaded structure. The hysteresis effect becomes gradually less important for the following cycles and eventually negligible at the 5th cycle. The hysteresis causes 19.4% and 24.5% differences in the total thermal resistance of the unloaded GDL sample with respect to the thermal resistance at the beginning of the loading process for the first and the second cycles, respectively, see Fig. 4. The hysteresis for the first cycle is consistent with the result of Khandelwal and Mench [12]. The thermal resistance hysteresis gradually increases and reaches 30.3% at the 5th cycle. A similar behavior is observed for the TCR variation under cyclic compression, which is shown in Fig. 5. However, the hysteresis seems to be higher for the TCR and starts at 22.5% at the first cycle, continues to 28.4% at the second cycle and reaches 34.5% at the end (5th cycle).

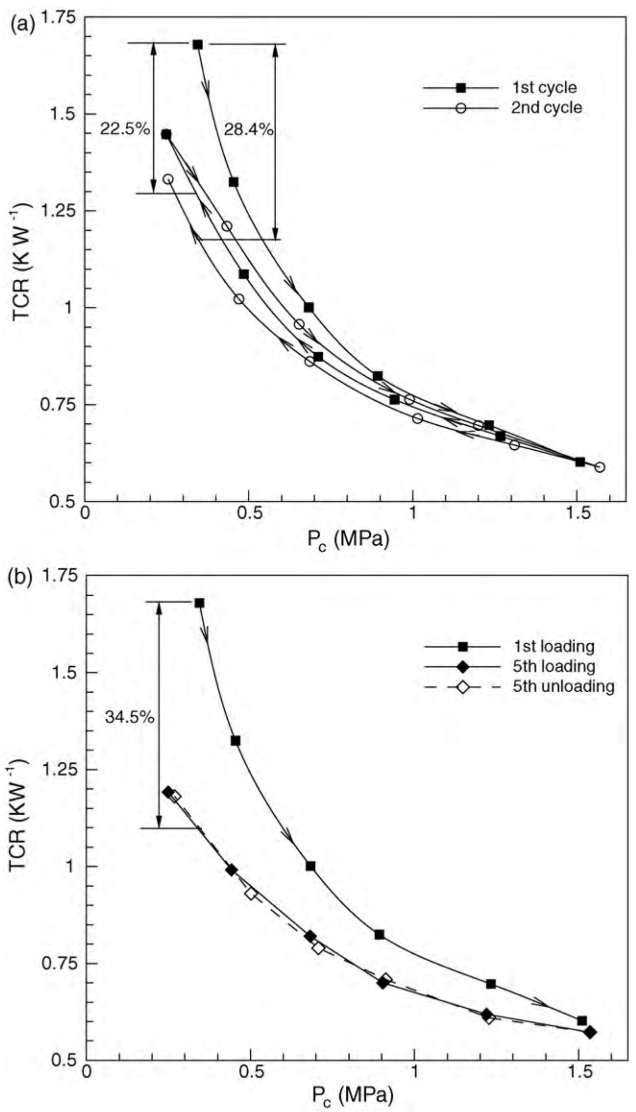

Fig. 5. Thermal contact resistance hysteresis under cyclic compressive load (a) comparison of 1st and 2nd cycles; (b) comparison of 1st loading and 5th unloading.

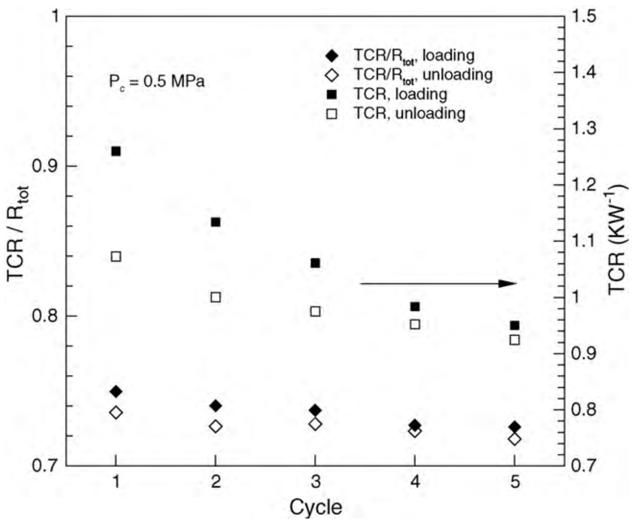

Fig. 6. TCR and “TCR to total resistance ratio” at different loading–unloading cycles, P_c = 0.5 MPa.

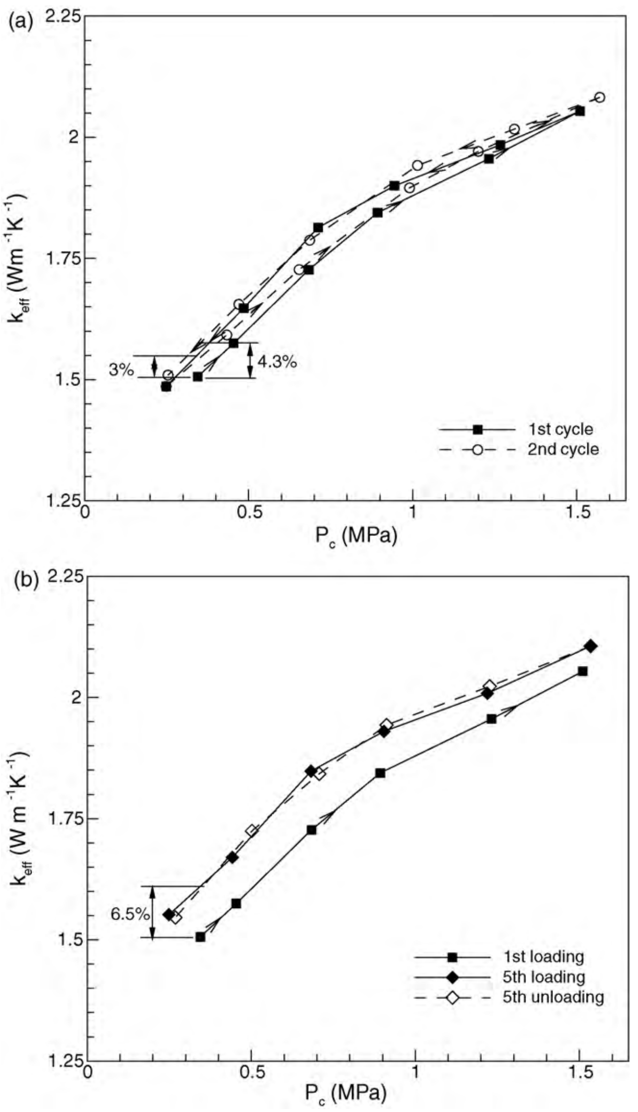

Fig. 7. Effect of loading and unloading on the GDL effective thermal conductivity: (a) comparison of 1st and 2nd cycles; (b) comparison of 1st loading and 5th unloading.

The variations of the TCR and "TCR to total resistance ratio" at different loading–unloading cycles are shown in Fig. 6 for a typical compressive load of 0.5 MPa. As expected, the TCR decreases as the number of loading cycles increases due to enhanced contact area at the GDL–solid (fluxmeter) interfaces. As the load cycling continues, the hysteresis in the TCR values decreases and becomes negligible for the 5th cycle. It should be noted that the "TCR to total resistance ratio" remains approximately constant during the loading–unloading cycles; it is also noteworthy that the TCR includes 73% of the total resistance of the sandwiched GDL. This clearly indicates the importance of TCR which remains the dominant resistance in the assembly even after several loading-unloading cycles. More importantly, the TCR to total resistance ratio remains almost constant; one can conclude that the loading-unloading cycles have an approximately equal impact (hysteresis effect) on both bulk resistance and TCR of GDLs. It should be emphasized that the TCR is an interface phenomenon and depends on the fibrous micro-structure (bulk GDL properties) and the solid surface characteristics as well as the compressive load; whereas the effective thermal conductivity is primarily a bulk property of a GDL. Consequently, any successful solution to reduce thermal resistance and/or improve thermal management of the membrane electrode assembly (MEA) should include interfacial phenomena such as the TCR, which to date have been largely overlooked.

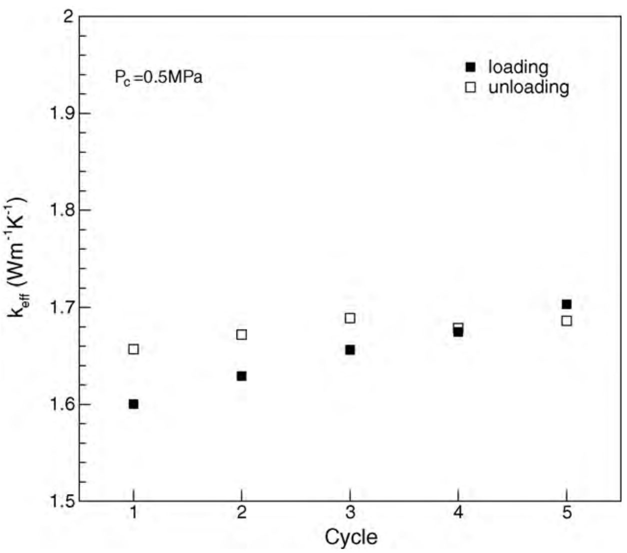

Fig. 8. Effective thermal conductivity at different loading–unloading cycles, $P_c = 0.5$ MPa.

Fig. 7 shows the effective thermal conductivity values at different contact pressures during the loading–unloading process. The effective conductivity increases with an increase in the compressive load due to larger contact areas between the contacting fibers providing a lower resistance path for heat flow [2]. Hysteresis is also observed in the thermal conductivity behavior as a result of the hysteresis in the total thermal resistance, TCR, and the sample thickness. The hysteresis in thermal contact resistance and TCR increases the thermal conductivity during unloading, whereas the mechanical hysteresis (reduction in thickness) has a reverse effect; the net effect is a smaller hysteresis in the effective thermal conductivity behavior in comparison with the TCR. This results in a maximum difference of 6.5% between the effective conductivity values of the unloaded GDL at the 5th cycle and the loaded GDL at the starting point.

The variation of the effective thermal conductivity of GDL under compression-release cycles is shown in Fig. 8 under vacuum condition for a typical compressive load of 0.5 MPa. The effective con-

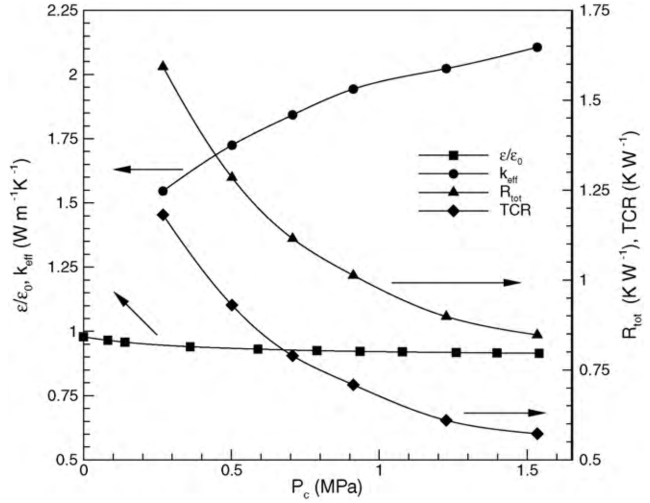

Fig. 9. Thermal and geometrical properties of Toray carbon paper TGP-H-120 with 5% wet proofing at quasi steady-state condition (after 5th loading cycle) under vacuum condition.

ductivity slowly increases with the number of loading cycles. Also, the thermal conductivity values during unloading are higher as a result of the irreversible deformations that occur during loading.

The results show that the thermal and geometrical properties of GDLs reach a quasi steady-state condition and remain unchanged after the 5th compression-release cycle. In practice, a fuel cell stack is subjected to many more than five loading–unloading cycles; therefore, the steady-state values for properties should be used in PEM fuel cell modeling. Fig. 9 summarizes the effective thermal conductivity, TCR, normalized porosity, and total thermal resistance (bulk and TCR) for the GDL sample used in this study over a range of compressive load.

4. Summary and conclusions

A test bed was designed and built to measure and predict thermal conductivity and thermal contact resistance of GDLs under cyclic compressive loads and vacuum condition. Toray carbon papers with 78% porosity and 5% PTFE were compressed from 0.25 MPa to approximately 1.5 MPa and then decompressed to the starting point to investigate the effects of cyclic compressive load. The number of load cycles was continued until hysteresis effects became negligible; this occurred at the 5th cycle. The thickness of the GDL was measured under cyclic compressive load using a tensile-compression machine. Results show a significant hysteresis in the total thermal resistance, TCR, effective thermal conductivity and porosity. This hysteresis is more pronounced for the TCR, and relatively smaller for the effective conductivity.

An important finding is the dominant contribution of thermal contact resistance. The ratio of thermal contact to bulk GDL resistance remains approximately constant (2.7/1) over the cyclic compressive load investigated in this work. Also, the effective thermal conductivity increases during unloading due to irreversible deformations occurring during the loading process such as fiber breakage and fiber displacement.

This work has helped clarify the impact of unsteady/cyclic compression on the thermal and structural properties of GDLs and provides new insights on the importance of a key interfacial phenomenon, as well as data that should contribute to further progress in computational fuel cell models.

Acknowledgements

The authors are grateful for the financial support of the Natural Sciences and Engineering Research Council (NSERC) of Canada, and the Canada Research Chairs Program.

References

[1] P. Rama, R. Chen, J. Andrews, J. Power Energy 222 (2008) 421–441.
[2] E. Sadeghi, N. Djilali, M. Bahrami, J. Power Sources (2010), doi:10.1016/j.jpowsour.2010.06.039.
[3] A. Kusoglu, Y. Tang, M.H. Santare, A.M. Karlsson, S. Cleghorn, W.B. Johnson, J. Fuel Cell Sci. Technol. 6 (2009) 011012–011019.
[4] A. Kusoglu, A.M. Karlsson, M.H. Santare, S. Cleghorn, W.B. Johnson, J. Power Sources 161 (2006) 987–996.
[5] J.P. Feser, A.K. Prasad, S.G. Advani, J. Power Sources 162 (2006) 1226–1231.
[6] J. Kleemann, F. Finsterwalder, W. Tillmetz, J. Power Sources 190 (2009) 92–102.
[7] S. Escribano, J.-F. Blachot, J. Etheve, A. Morin, R. Mosdale, J. Power Sources 156 (2006) 8–13.
[8] P. Zhou, C.W. Wu, G.J. Ma, J. Power Sources 159 (2006) 1115–1122.
[9] A. Bazylak, D. Sinton, Z.-S. Liu, N. Djilali, J. Power Sources 163 (2007) 784–792.
[10] I. Nitta, O. Himanen, M. Mikkola, Fuel Cells 08 (2008) 111–119.
[11] O. Burheim, P.J.S. Vi, J.G. Pharoah, S. Kjelstrup, J. Power Sources 195 (2010) 249–256.
[12] M. Khandelwal, M.M. Mench, J. Power Sources 161 (2006) 1106–1115.
[13] C.M. van Wyk, Onderstepoort., J. Vet. Sci. Anim. Ind. 21 (1946) 99–107.
[14] C.M. van Wyk, J. Text. Inst. 37 (1946) T285–T305.
[15] J.I. Dunlop, J. Text. Inst. 74 (1983) 92–97.
[16] I. Krucinska, I. Jalmuzna, W. Zurek, Text. Res. J. 74 (2004) 127–133.
[17] G.A. Carnaby, N. Pan, Text. Res. J. 59 (1989) 275–284.
[18] N.B. Beil, W.W. Roberts, Text. Res. J. 72 (2002) 341–351.
[19] N.B. Beil, W.W. Roberts, Text. Res. J. 72 (2002) 375–382.
[20] S.B. Stankovic, Polym. Eng. Sci. 48 (2008) 676–682.

Appendix F

A Novel Approach to Determine the In-Plane Thermal Conductivity of Gas Diffusion Layers in Proton Exchange Membrane Fuel Cells

Reproduced by permission of Elsevier

Accepted Manuscript

Title: A novel approach to determine the in-plane thermal conductivity of gas diffusion layers in proton exchange membrane fuel cells

Authors: E. Sadeghi, N. Djilali, M. Bahrami

PII: S0378-7753(10)02143-9
DOI: doi:10.1016/j.jpowsour.2010.11.151
Reference: POWER 13931

To appear in: *Journal of Power Sources*

Received date: 20-9-2010
Revised date: 28-11-2010
Accepted date: 29-11-2010

Please cite this article as: E. Sadeghi, N. Djilali, M. Bahrami, A novel approach to determine the in-plane thermal conductivity of gas diffusion layers in proton exchange membrane fuel cells, *Journal of Power Sources* (2010), doi:10.1016/j.jpowsour.2010.11.151

Research Highlights

A new thermal measurement technique was developed to measure the in-plane thermal conductivity of GDLs for various polytetrafluoroethylene (PTFE) contents. Toray carbon papers TGP-H-120 with PTFE content of *5* to *30%* were used in the experiments. The experiments were complemented by a compact model for the in-plane thermal conductivity that accounts for heat conduction through randomly oriented fibers, contact area between fibers, and PTFE covered regions. The model predictions are in good agreement with experimental data over a range of PTFE content.

An important finding is that the in-plane effective thermal conductivity remains almost unchanged, $k \approx 17.5\, Wm^{-1}K^{-1}$, over a wide range of PTFE content; this value is approximately *12* times higher than the through-plane conductivity. However, the thermal contact resistance and the end effects increases with the PTFE content due to increased number of PTFE coated fibers.

In addition to providing for the first time through-plane effective conductivity data, this work clarifies the effect of PTFE content on the effective thermal conductivity and contact resistance of GDLs, and provides input data for fuel cell models.

A novel approach to determine the in-plane thermal conductivity of gas diffusion layers in proton exchange membrane fuel cells

E. Sadeghi[a,b,*], N. Djilali[a], M. Bahrami[b]

[a] Dept. Mechanical Eng., and Institute for Integrated Energy Systems, University of Victoria, P.O. Box 3055, Victoria, BC, Canada, V8W 3P6

[b] Mechatronic Systems Engineering, School of Engineering Science, Simon Fraser University, Surrey, BC, Canada V3T 0A3

Abstract

Heat transfer through the gas diffusion layer (GDL) is a key process in the design and operation of a proton exchange membrane (PEM) fuel cell. The analysis of this process requires determination of the effective thermal conductivity. This transport property differs significantly in the through-plane and in-plane directions due to the anisotropic micro-structure of the GDL.

A novel test bed that allows separation of in-plane effective thermal conductivity and thermal contact resistance in GDLs is described in this paper. Measurements are performed using Toray carbon paper TGP-H-120 samples with varying polytetrafluoroethylene (PTFE) content at a mean temperature of 65-70°C. The measurements are complemented by a compact analytical model that achieves good agreement with experimental data. The in-plane effective thermal conductivity is found to remain approximately constant, $k \approx 17.5\ Wm^{-1}K^{-1}$, over a wide range of PTFE content, and its value is about 12 times higher than that for through-plane conductivity.

Key words: conduction heat transfer, in-plane thermal conductivity, fibrous porous media, anisotropic micro-structure, polytetrafluoroethylene coating

---

* Corresponding author at: Dept. Mechanical Eng., and Institute for Integrated Energy Systems, University of Victoria, P.O. Box 3055, Victoria, BC, Canada V8W 3P6. Tel.: +1 7787828587; fax: +1 2507216051. E-mail address: ehsans@uvic.ca (E. Sadeghi).

Nomenclature

A = cross-sectional area of fluxmeters, heat radiation area (m^2)

A_f = cross-sectional area of a fiber (m^2)

A_{in} = cross-sectional area of GDL (m^2)

a = radius of contact area between fibers (m)

b = radius of the area covered by PTFE at contact points (m)

e = emissivity, Eq. (1)

F_{ij} = view factor, Eq. (1)

k = thermal conductivity ($Wm^{-1}K^{-1}$)

k_{cell} = in-plane effective thermal conductivity of each cell, Fig. 3 ($Wm^{-1}K^{-1}$)

$k_{eff,in}$ = in-plane effective thermal conductivity of GDL ($Wm^{-1}K^{-1}$)

$k_{eff,in,0}$ = in-plane effective thermal conductivity of GDL, no PTFE ($Wm^{-1}K^{-1}$)

$k_{Parallel}$ = effective thermal conductivity based on the Parallel model ($Wm^{-1}K^{-1}$)

k_{PTFE} = thermal conductivity of PTFE ($Wm^{-1}K^{-1}$)

k_s = thermal conductivity of carbon fiber ($Wm^{-1}K^{-1}$)

L = length of GDL sample, distance between sample holders, Figs. 1, 3 (m)

m = number of cells

N = total number of GDL samples in the experiment

n = number of fibers in each cell

Q = heat transfer rate (W)

Q_{ij} = Radiation heat transfer between bodies *i* and *j* (W)

q = heat flux (Wm^{-2})

R_{cell} = cell thermal resistance (KW^{-1})

R_{end} = thermal resistance at sample ends (KW^{-1})

R_{fl} = thermal resistance of fluxmeter (KW^{-1})

R_{GDL} = GDL thermal resistance (KW^{-1})

R_{gr} = groove thermal resistance (KW^{-1})

R_{junc} = total thermal resistance at each cell interface (KW^{-1})

R_{layer} = summation of GDL and groove thermal resistance (KW^{-1})

R_{PTFE} = thermal resistance of PTFE in contact regions of fibers (KW^{-1})

R_{SH} = sample holder thermal resistance (KW^{-1})

R_{tot} = total thermal resistance (KW^{-1})

R_w = thermal resistance of wooden block (KW^{-1})

r = fibers' mean radius (m)

T = temperature (K)

TCR = thermal contact resistance between fibers (KW^{-1})

t = sample thickness (m)

$\bar{V}$ = average volume of a fiber (m^3)

V_s = total volume of fibers (m^3)

V_{tot} = total volume of GDL sample (m^3)

W = width (m)

z = heat flow direction (m)

Greek symbols

α = radius of contact area between fibers over fiber radius, ar^{-1}

β = radius of area covered by PTFE over fiber radius, br^{-1}

λ = weight fraction of PTFE content

σ = Stefan-Boltzmann constant

ε_0 = GDL porosity before PTFE treatment

θ = angle between fiber and heat flux directions

θ_m = maximum fiber angle

ϕ_s = fiber volume fraction

ℓ = fiber average length (m)

Subscripts

1 = right side of the experiment setup

2 = left side of the experiment setup

i = body *i*

j = body *j*

low = lower fluxmeter

r = radiation

up = upper fluxmeter

1. Introduction

The temperature distribution in a proton exchange membrane (PEM) fuel cell is non-uniform due to the electrochemical reaction and associated irreversibilities [1-5]. Accurate knowledge of the temperature distribution and associated heat transfer rates is required to determine various transport phenomena such as water and species transport, reaction kinetics, and rate of phase change. Thermal transport also impacts design, efficiency, reliability and durability of the system [6-8].

A key thermo-physical property for thermal analysis of fuel cells is the thermal conductivity of the membrane-electrode assembly components, particularly the gas-diffusion layer (GDL) [9, 10]. The fibrous anisotropic micro-structure of a GDL combined with the large differences between the thermal conductivity of the solid (carbon fibers) and fluid (air/water) phases make it challenging to determine the dependence of the effective thermal conductivity on direction.

The majority of the thermal analyses of fuel cells have relied on a simplified model representation that assumes an isotropic thermal conductivity [10-12] that is determined as a combination of the parallel and series models and/or based on the geometric mean of the thermal conductivities of solid and fluid phases [11, 12]. Although the thermal resistance of GDLs for the in-plane direction is higher compared to the through-plane direction, heat transfer to the bipolar plate (BPP) occurs in both directions due to the alternating nature of the land and channel areas [13]. In the few modeling studies that have considered anisotropy, parametric investigations have shown that the prescription of anisotropic properties has a major impact on current density distribution and on the relative importance of limiting transport processes [13-15]. The determination of the in-plane thermal conductivity is therefore an important parameter for thermal analysis and management of PEM fuel cells and stacks.

Theoretical prediction of the in-plane thermal conductivity of GDLs includes the work of Zamel et al. [16] who developed a numerical model to estimate the through-plane and in-plane effective thermal conductivities of a dry untreated carbon paper GDL. They studied the effects of porosity, fiber distribution and compression on the effective thermal conductivity and concluded that the impact of fiber distribution is more pronounced for the through-plane direction than the in-plane direction. The numerical results indicate that porosity is an essential determinant of the effective thermal conductivity of a GDL but not compression. Based on the results, Zamel et al. [16] proposed correlations for the effective thermal conductivity of a dry GDL with no binder or hydrophobic treatment.

GDL's are generally treated with polytetrafluoroethylene (PTFE) to render it hydophobic and enhance liquid water transport [17]. The effect of PTFE treatment on the thermal transport parameters has been investigated by Khandelwal and Mench [18]. Their measurements for

SIGRACET® GDLs showed that for 20% PTFE content, the through-plane thermal conductivity was reduced by *54%* compared to untreated GDL samples; the thermal contact resistance on the other hand was not significantly affected by the variation of PTFE content. These results are opposite to expected trends from physical considerations; additional PTFE is for instance expected to displace lower conductivity air, and hence results in higher effective thermal conductivity. Karimi et al. [19] investigated the effect of PTFE coating on the through-plane conductivity and thermal contact resistance of SpectraCarb GDLs, and reported that the effective thermal conductivity of PTFE-treated GDLs increased slightly at low compression loads and decreased slightly at higher loads. For low compression loads, they also reported significantly higher thermal contact resistance values for PTFE-treated samples compared to untreated ones. This difference decreased with an increase in applied pressure.

Several experimental approaches have been proposed to measure *electrical* conductivity of GDLs. Ismail et al. [20] measured the in-plane and through-plane electrical conductivity of SIGRACET® GDLs, and found the in-plane electrical conductivity remains approximately constant with an increase in PTFE content. They also reported that the through-plane electrical contact resistance increases with PTFE content.

The micron scale of the fibers combined with the brittle nature of the GDL structure make it challenging to measure the *in-plane thermal conductivity* of such random micro-structures, and to the author's knowledge, no experimental data has been reported in the open literature.

This paper presents a combined experimental and theoretical investigation focusing on the determination of the in-plane thermal conductivity of PTFE-coated GDLs. Building on our previous study that dealt with the through-plane conductivity and contact resistance [21], the existing test bed was modified and an experimental technique developed that enables the measurement of in-plane thermal conductivity of fibrous porous media and thin films. Toray carbon papers TGP-H-120 with different PTFE contents are used in the experiments. The in-plane effective thermal conductivity and contact resistance are deduced from the total thermal resistance measurements by performing a series of experiments with GDL samples of different lengths but similar micro-structures. Furthermore, a compact analytical model is proposed to predict the in-plane thermal conductivity of GDLs as a function of porosity and PTFE content.

2. Experimental study

The experimental apparatus and a schematic of the test setup for the in-plane thermal conductivity measurement are shown in Fig. 1. The test chamber consists of a stainless steel base plate and a bell jar enclosing the test column. The test column consists of, from top to bottom: the loading mechanism; the heater block; the upper fluxmeter; the sample holders; the sample assembly; the lower fluxmeter; the heat sink (cold plate); and the polymethyl-methacrylate (PMMA) layer.

The heater block was made of a flat aluminum block in which a pencil-type electrical heater was installed. The designed cold plate consisted of a hollow copper cylinder, *1.9 cm* high and *15 cm* diameter. Cooling was accomplished using a closed loop water-glycol bath in which the coolant temperature can be set. The cold plate was connected to the chiller unit which adjusts the cold water temperature. A load was applied on the upper wooden block and fluxmeter to improve the contact between the sample holders and the fluxmeters.

The fluxmeters were made of standard electrolyte iron. To measure temperatures along the fluxmeters, six T-type thermocouples were attached to each fluxmeter at specific locations shown in Fig. 1 (b). The thermal conductivity of the fluxmeters was known and used to measure the heat flow rate. The sample holders were made of aluminum and have two grooves with the width of *1.15 mm.* Two T-type thermocouples were attached to each sample holder near the grooves to measure the temperature.

2.1. Sample preparation

Toray carbon papers TGP-H-120 with the base porosity (porosity of the untreated GDL) of *78%* were used. Samples with a wide range of PTFE content, from *5%* to *30%,* were used. The thickness of GDL samples was measured using a Mitutoyo digital micrometer with the accuracy of *0.001 mm*. The measurements were performed *10* times for each sample at different locations, and the average values are reported in Table 1. Rectangular test samples were cut with a width of *35 mm* and different lengths.

2.2. Test procedure

The experiments were performed under a vacuum to ensure negligible convection heat transfer. Depending on the thickness, a number of similar GDL samples, e.g. three sheets for TGP-H-120, were stacked together and inserted in each groove of the sample holders as shown in Fig. 1. The use of several layers of GDLs mitigated some of the experimental challenges and uncertainties: use of a single GDL layer between the sample holders leads to an excessive temperature drop across the sample holders, which in turn results in insufficient heat flow across the GDL that cannot be measured accurately. This is due to micron size cross-sectional area of the GDL. After investigating and trying different methods, the present sample holders featuring multiple grooves that can hold several GDLs was devised to overcome these challenges.

To reduce the contact resistance between the groove walls and the samples, a thin layer of thermal paste was applied inside each groove. To improve the stability of the sample holders and provide a good contact with the fluxmeters, compressive loads were applied to the upper wooden block and the upper fluxmeter; this is solely to keep the test column together. Thermal paste was also used to reduce the thermal contact resistance at the interfaces between the sample holders and the fluxmeters.

Temperatures were monitored continuously and recorded when steady-state conditions were achieved. This took approximately 7 hours for each experiment. The fairly long equilibration time is due to the restricted cross sectional area through which heat transfer takes place. The temperature gradient between the hot and cold plates results in one-dimensional heat conduction from the top to the bottom of the test column. The thermal resistance network corresponding to the experimental set up is shown in Fig. 2 (a). Natural convection heat losses are negligible in the vacuum chamber. Radiation heat losses from the fluxmeters and end plates can be estimated from the following relationship [22].

$$Q_{ij} = \frac{\sigma\left(T_i^4 - T_j^4\right)}{\frac{1-e_i}{e_i A_i} + \frac{1}{A_i F_{ij}} + \frac{1-e_j}{e_j A_j}} \qquad (1)$$

where, $\sigma = 5.67 \times 10^{-8} Wm^{-2}K^{-4}$ is the Stefan-Boltzmann constant. Q_{ij} is the radiation exchange between bodies i and j, and e is the emissivity. Also, F_{ij} is the view factor defined as the fraction of the radiation that leaves A_i and is intercepted by A_j. To find the radiation heat losses, Eq. (1) is employed which provides the maximum radiative heat transfer between two bodies. The investigated radiation losses from the fluxmeters to the wooden blocks and the chamber wall are less than *1%* of the total heat flow passing the fluxmeters. Also, small temperature difference between the fibers in GDLs as well as relatively low temperature levels (less than 370 K) inside the medium ensure negligible radiation heat transfer in the GDL. Thus, heat transfer is only due to conduction and can be determined using Fourier's equation.

$$Q = -kA\frac{dT}{dz} \tag{2}$$

where, dT/dz is the temperature gradient along the test column, k is the thermal conductivity of the fluxmeters, and A is the cross-sectional area of the fluxmeters. Considering negligible heat losses, the resistance network shown in Fig. 2(a) can be reduced to Fig. 2(b). The total thermal resistance between two sample holders, R_{tot}, includes the samples' thermal resistance and the resistances at the sample ends (a combination of the thermal contact resistance between the grooves and the samples and other possible resistances caused by the edges of the grooves at each end) and can be expressed as:

$$R_{tot} = \frac{R_{layer}}{N} = \frac{R_{GDL} + R_{gr1} + R_{gr2}}{N} = \frac{R_{GDL}}{N} + \frac{R_{end}}{N} = \frac{\Delta T}{Q} \tag{3}$$

where, ΔT is the temperature difference between the two sample holders and N is the total number of GDLs layers stacked in the grooves. R_{GDL} and R_{end} are the thermal resistance of each sample and the total thermal resistance at the end points of each sample, respectively. There is a small difference between the heat flow values measured for the upper and lower fluxmeters due to heat losses to the lower wooden block and to experimental uncertainties; heat losses to the wooden block are about *4%* of the heat flow passing the upper fluxmeter. Therefore, the actual heat flux which passes through the GDL samples is the heat flux measured at the lower fluxmeter. To ensure accuracy, this heat flow rate was used in the analysis, i.e., Eq. (3). To find the in-plane thermal conductivity, two sets of experiments were performed with different sample lengths. Under the same experimental conditions, R_{end} for both experiments was assumed to be equal. Applying Eq. (3) to both of the measurements and subtracting them, one can find the in-plane effective thermal conductivity.

$$k_{eff,in} = \frac{L_1}{R_{GDL1}A} = \frac{L_2}{R_{GDL2}A} \tag{4}$$

$$k_{eff,in} = \frac{N(L_1 - L_2)}{(R_{tot1} - R_{tot2})A_{in}} \tag{5}$$

where, $L_1$and L_2 are the sample length, the distance between the two sample holders, in experiment 1 and 2, and A_{in} is the in-plane cross-section of each sample.

2.3. Uncertainty analysis

Considering the relationship for evaluating the in-plane effective thermal conductivity, i.e. Eqs.(3), (5), the relevant parameters in the analysis can be expressed as:

$$k_{eff,in} = f(Q, \Delta T, t, W, L) \tag{6}$$

The main uncertainty in our experiments is due to errors in determining the heat flux through the sample holders which leads to a maximum error of 3.7%. The maximum uncertainties for the thermocouples and the data acquisition readings are ± 1℃ which introduces a maximum error of 1.8% between two sample holders. Other uncertainties including those associated with the width, thickness, and length measurements are 0.3%, 0.3%, and 0.9%, respectively. The maximum uncertainty for the thermal resistance measurements can be calculated from [23]:

$$\frac{\delta k_{eff,in}}{k_{eff,in}} = \sqrt{\left(\frac{\delta Q}{Q}\right)^2 + \left(\frac{\delta \Delta T}{\Delta T}\right)^2 + \left(\frac{\delta t}{t}\right)^2 + \left(\frac{\delta W}{W}\right)^2 + \left(\frac{\delta L}{L}\right)^2} \tag{7}$$

For the present study, the maximum uncertainty is estimated to be ±4.2%.

3. Analytical study

The complex micro-structure and associated heat transfer mechanism of fibrous GDLs make it difficult to develop an analytic model for the effective thermal conductivity. To model the in-plane effective thermal conductivity, a random micro-structure divided into *m* equally-sized cells is considered. Each cell consists of *n* fibers with an average radius of *r* and an average length of ℓ which are randomly oriented in the *xy* plane with an angle θ to the in-plane heat flow direction and stacked vertically in *z* direction, as shown in Fig. 3. The fiber angle θ can vary in this representation.

Considering that the primary path for the heat conduction is through the fibers and heat transfer between the fibers in a cell is negligible due to large contact resistances, a parallel equivalent circuit model can be used to determine the thermal conductivity in each cell. The heat conducted through the i^{th} fiber with an angle θ_i to the heat flux vector $\vec{q}_i$ is $q_i \cos\theta_i$, therefore, each fiber deviates from the Parallel model by $\cos\theta_i$. Thus, the effective conductivity for each cell, k_{cell}, can be written as:

$$k_{cell} = \frac{\sum_{i=1}^{n} \cos\theta_i}{n} k_{Parallel} = \frac{\sum_{i=1}^{n} \left(k_s A_f \cos\theta_i\right)}{(n\, A_f/\phi_s)} = \overline{\cos\theta}\ \phi_s k_s \tag{8}$$

where, n and $\bar{\theta}$ are the number of fibers in a cell and the average angle of fibers with respect to the heat flux direction, respectively. k_s and $A_f$is are the fiber thermal conductivity and cross-sectional area, respectively. ϕ_s is the fiber volume fraction, i.e. $\phi_s = 1 - \varepsilon_0$, where ε_0 is the GDL porosity before PTFE treatment. We assume that the heat flow is transferred from cell to cell through the junctions. The length of each cell is defined as the average conduction path in a cell, $\ell\,\overline{\cos\theta}$. Since the fibers are stacked together in a packed micro-structure, it is assumed that each fiber of two neighboring cells is in contact with two fibers from the top and bottom and carries heat from them as shown in Fig. 4. The contact between the fibers at a junction is shown in Fig. 5.

To estimate the in-plane effective thermal conductivity of the medium, the total resistance is needed which can be found using the thermal resistance network shown in Fig. 6.

The number of cells as well as the number of fibers in each cell is required to evaluate the thermal resistances. These values can be found through:

$$m = \frac{L}{\ell\,\overline{\cos\theta}} \tag{9}$$

$$n = \frac{V_s}{m\bar{V}} = \frac{\phi_s V_{tot}}{m\bar{V}} = \frac{Wt\phi_s\ \overline{\cos\theta}}{\pi r^2} \tag{10}$$

where, $\overline{V}$, W and t are the average volume of each fiber, the width and the thickness of the GDL sample. The contact resistance between two fibers can be expressed as the summation of constriction and spreading resistances [21].

$$TCR = \frac{1}{2k_s a} = \frac{1}{2k_s r\alpha} \tag{11}$$

where, a is the radius of contact area between fibers and α is a/r. A portion of PTFE in GDLs covers the contacting fibers providing an additional path for the heat flow from one fiber to another. The thermal resistance of this path based on the geometry shown in Fig. 5 can be expressed as:

$$\frac{1}{R_{PTFE}} = \frac{1}{2}\int \frac{1}{dR} = \frac{1}{2}\int_{a}^{b} \frac{k_{PTFE}(2\pi x\, dx)}{(r-y)} \tag{12}$$

$$R_{PTFE} = \frac{1}{\pi k_{PTFE} r}\left(\int_{\alpha}^{\beta} \frac{u\, du}{1-\sqrt{1-u^2}}\right)^{-1} \tag{13}$$

where, $\beta = b/r$ and b is the radius of the area covered by PTFE around the contacting fibers, see Fig. 5. The total thermal resistance at each cell interface R_{junc} can be expressed as a parallel combination of the thermal resistances of *2n* contact regions.

$$R_{junc} = \frac{\left(TCR^{-1} + {R_{PTFE}}^{-1}\right)^{-1}}{2n} \tag{14}$$

Referring to Fig. 6, the total resistance can be written as:

$$R_{tot} = mR_{cell} + (m-1)R_{junc} \tag{15}$$

where, R_{cell} is the cell thermal resistance which can be found using Eq. (8).

$$R_{cell} = \frac{\ell}{\phi_s k_s W t} \tag{16}$$

Finding the total thermal resistance from Eq. (15), one can evaluate the effective thermal conductivity using the following relation.

$$k_{eff,in} = \frac{L}{R_{tot} W t} \tag{17}$$

For the sample with no PTFE coating, Eq. (17) can be simplified to:

$$k_{eff,in,0} = \frac{4\alpha L \phi_s k_s \overline{\cos\theta}}{4\alpha L + \pi(m-1)r} \cong \frac{4\alpha \ell \phi_s k_s \overline{\cos\theta}^{\,2}}{4\alpha \ell \overline{\cos\theta} + \pi r} \tag{18}$$

Based on scanning electron microscopy (SEM) images of Toray carbon papers, Fig. 7, the fiber angle with respect to the heat flow direction, θ, can vary arbitrarily between $-\theta_m$ and θ_m , where $0 \le \theta_m \le 90$. Considering an arbitrary distribution of fiber angle without preferential direction, $\overline{\cos\theta}$ can be estimated through:

$$\overline{\cos\theta} = \frac{\sum_{i=1}^{n}\cos\theta_i}{n} = \frac{\sum_{i=1}^{n}\cos\theta_i\,\Delta\theta}{n\,\Delta\theta} = \frac{\sum_{i=1}^{n}\cos\theta_i\,\Delta\theta}{2\,\theta_m} \tag{19}$$

where, $\Delta\theta = [\theta_m - (-\theta_m)]/n$. The number of fibers in a cell is large enough, $n \cong 35000$, to convert the series in Eq. (19) to an integral.

$$\overline{\cos\theta} = \frac{\sum_{i=1}^{n}\cos\theta_i\,\Delta\theta}{2\,\theta_m} = \frac{\int_{-\theta_m}^{\theta_m}\cos\theta\,d\theta}{2\,\theta_m} = \frac{\sin\theta_m}{\theta_m} \tag{20}$$

We measured the fiber angle in the SEM image, Fig. 7, and our analysis shows that the majority of fiber angles are between *-75* to *75*, i.e. $\theta_m = 75$. Other specifications of the Toray carbon paper required for the present model are listed in Table 2.

Toray carbon papers have the highest through-plane thermal conductivity among different available carbon papers with similar porosity due to the contribution of the binder to heat transfer in the carbon paper GDL [16]. The binder fills the gaps between fibers and provides a better contact. The thermal conductivity of the binder can be assumed to be equal to that of the carbon fibers [16]. The actual amount of binders at contact points and as a result the contact area between contacting fibers are unknown. To determine the in-plane thermal conductivity, the value for the radius ratio of contact area to the fiber, α, was estimated as *0.1* based on SEM observation shown in Fig. 4.

The PTFE conductivity is very low compared to the thermal conductivity of carbon fibers and its effect on the in-plane thermal conductivity is small as shown later. However, to include the effect of PTFE variation in the model, we assume that the radius ratio of PTFE to carbon fiber, β, is *0.25* for *5%* and 1 for *30%* PTFE content; and remains constant at *1* for higher values of PTFE content. The following relationship is developed for the PTFE content at the contact points of fibers.

$$\beta = 0.25 + 3(\lambda - 0.05) \tag{21}$$

where, λ is the weight fraction of PTFE, $0.05 \leq \lambda \leq 0.3$. This is an approximate relationship, which is proposed based on SEM images of carbon papers with different PTFE contents. However, due to the very low thermal conductivity of PTFE, variants of this distribution do not have a significant impact on the model predictions.

4. Results and discussion

Measurements were taken for TGP-H-120 samples with different PTFE contents. A summary of the experimental results is shown in Table 3. The measurements were performed at an average sample temperature of 65-70℃. There is a small difference between the measured values of heat fluxes in the upper and the lower fluxmeters due to heat losses and experimental uncertainties. Due to heat losses to the lower wooden block, the readings from the lower heat flux were used for thermal resistance calculations. As shown in Table 3, the in-plane thermal conductivity appears to increase slightly with PTFE content as a result of reduced contact resistance between fibers. However, this variation is within the uncertainty band of the present experimental measurement. The thermal conductivity values obtained lie between the values predicted by Zamel et al. [16] and those of the manufacturer [28]. Zamel et al. [16] reported an in-plane thermal conductivity value of $10\ Wm^{-1}k^{-1}$ based on numerical simulations at a temperature of *68°C*; the value reported in the manufacturer's data sheet [28] is *21* and *23* $Wm^{-1}k^{-1}$ at the room temperature and 100℃, respectively.

By increasing PTFE content, the number of PTFE coated fibers in contact with the grooves increases. This results in a higher contact resistance between the GDL samples and the groove walls. This resistance R_{end} increases *26%* by increasing PTFE content from *5%* to *30%* as shown in Table 3.

The developed analytical model for the in-plane effective thermal conductivity is compared with the experimental data in Fig. 8. Good agreement is obtained with a maximum deviation of *5%*. We note that the model reproduces the slight increase in effective thermal conductivity with PTFE content observed in the experimental data.

In practice, due to the electrochemical reaction, overall water transport and phase change, water in both vapor and liquid form is present in a fuel cell [2]. This water may impact the thermal conductivity while passing through the GDL. The thermal conductivity of humidified gasses or water is several orders of magnitude lower than the thermal conductivity of carbon fibers, and considering the relatively parallel paths for the heat transfer through them, the effect of water content on the in-plane thermal conductivity of GDLs is expected to be minimal when the GDL is not significantly flooded. In the through-plane direction, the effect of water is likely much more important as it can provide additional pathways for heat transfer in the contact regions between fibers. Burheim et al. [29] compared the through-plane thermal conductivity of dry and humidified GDLs and showed that the conductivity increases by about *70%* for low contact pressures when water was added to the GDL. This issue needs to be further investigated.

5. Summary and Conclusions

A new thermal measurement technique was developed to measure the in-plane thermal conductivity of GDLs for various PTFE contents. Toray carbon papers TGP-H-120 with PTFE content of *5* to *30%* were used in the experiments. The experiments were complemented by a compact model for the in-plane thermal conductivity that accounts for heat conduction through randomly oriented fibers, contact area between fibers, and PTFE covered regions. The model predictions are in good agreement with experimental data over a range of PTFE content.

An important finding is that the in-plane effective thermal conductivity remains almost unchanged, $k \approx 17.5\, Wm^{-1}K^{-1}$, over a wide range of PTFE content; this value is approximately *12* times higher than the through-plane conductivity. However, the thermal contact resistance and the end effects increases with the PTFE content due to increased number of PTFE coated fibers.

In addition to providing for the first time through-plane effective conductivity data, this work clarifies the effect of PTFE content on the effective thermal conductivity and contact resistance of GDLs, and provides input data for fuel cell models.

Acknowledgements

The authors are grateful for the financial support of the Natural Sciences and Engineering Research Council (NSERC) of Canada, and the Canada Research Chairs Program.

References

[1] N. Djilali, D. Lu, Influence of heat transfer on gas and water transport in fuel cells, Int. J. Therm. Sci. 41 (2002) 29-40.

[2] T. Berning, N. Djilali, A 3D, multi-Phase, multicomponent model of the cathode and anode of a PEM fuel cell , J. Electrochem. Soc. 150 (2003) A1589-A1598.

[3] G. Maggio, V. Recupero, C. Mantegazza, Modelling of temperature distribution in a solid polymer electrolyte fuel cell stack, J. Power Sources 62 (1996) 167-174.

[4] S. He, M.M. Mench, S. Tadigadapa, Thin film temperature sensor for real-time measurement of electrolyte temperature in a polymer electrolyte fuel cell, Sensors and Actuators A: Physical 125 (2006) 170-177.

[5] P.J.S. Vie, S. Kjelstrup, Thermal conductivities from temperature profiles in the polymer electrolyte fuel cell, Electrochim. Acta 49 (2004) 1069-1077.

[6] A. Kusoglu, Y. Tang, M.H. Santare, A.M. Karlsson, S. Cleghorn, W.B. Johnson, Stress-strain behavior of perfluorosulfonic acid membranes at various temperatures and humidities: Experiments and phenomenological modeling, J. Fuel Cell Sci. Technol. 6 (2009) 011012-011019.

[7] D.P. Wilkinson. H.H. Voss and K. Prater, Water management and stack design for solid polymer fuel cells, J. Power Sources 49 (1994) 117-127.

[8] P. Rama, R. Chen, J. Andrews, A review of performance degradation and failure modes for hydrogen-fuelled polymer electrolyte fuel cells, J. Power Energy 222 (2008) 421–441.

[9] A. Hakenjos, H. Muenter, U. Wittstadt, C. Hebling, A PEM fuel cell for combined measurement of current and temperature distribution, and flow field flooding, J. Power Sources 131 (2004) 213-216.

[10] H. Ju, H. Meng, C.Y. Wang, A single-phase, non-isothermal model for PEM fuel cells, Int. J. Heat Mass Trans. 48 (2005)1303-1315.

[11] J.J. Baschuk, X. Li, A general formulation for a mathematical PEM fuel cell model, J. Power Sources 142 (2005) 134-153.

[12] J.J. Hwang, Thermal-Electrochemical modeling of a proton exchange membrane fuel cell, J. Electrochem. Soc. 153 (2006) A216-A224.

[13] P.C. Sui, N. Djilali, Analysis of coupled electron and mass transport in the gas diffusion layer of a PEM fuel cell, J. Power Sources 161 (2006) 294-300.

[14] J.G. Pharoah, K. Karan, W. Sun, On effective transport coefficients in PEM fuel cell electrodes: Anisotropy of the porous transport layers, J. Power Sources, 161 (2006) 214-224.

[15] C. J. Bapat, S. T. Thynell, Effect of anisotropic thermal conductivity of the GDL and current collector rib width on two-phase transport in a PEM fuel cell, J. Power Sources 179 (2008) 240-251.

[16] N. Zamel, X. Li, J. Shen, J. Becker, A. Wiegmann, Estimating effective thermal conductivity in carbon paper diffusion media, Chem. Eng. Sci. 65 (2010) 3994-4006.

[17] G.G. Park, Y.J. Sohn, T.H. Yang, Y.G. Yoon, W.Y. Lee, C.S. Kim, Effect of PTFE contents in the gas diffusion media on the performance of PEMFC, J. Power Sources 131 (2004) 182-187.

[18] M. Khandelwal, M.M. Mench, Direct measurement of through-plane thermal conductivity and contact resistance in fuel cell materials, J. Power Sources 161 (2006) 1106-1115.

[19] G. Karimi, X. Li, P. Teertstra, Measurement of through-plane effective thermal conductivity and contact resistance in pem fuel cell diffusion media, Electrochim. Acta 55 (2010) 1619-1625.

[20] M.S. Ismail, T. Damjanovic, D.B. Ingham, M. Pourkashanian, A. Westwood, Effect of polytetrafluoroethylene-treatment and microporous layer-coating on the electrical conductivity of

gas diffusion layers used in proton exchange membrane fuel cells, J. Power Sources 195 (2010) 2700-2708.

[21] E. Sadeghi, N. Djilali, M. Bahrami, Effective thermal conductivity and thermal contact resistance of gas diffusion layers in proton exchange membrane fuel cells. Part 1: Effect of compressive load, J. Power Sources 196 (2011) 246-254.

[22] F.P. Incropera, D.P. DeWitt, Fundamentals of Heat and Mass Transfer, fourth ed., John Willey and Sons, New York, USA, 1996, Ch. 13.

[23] J.R. Taylor, An Introduction to Error Analysis: The Study of Uncertainties in Physical Measurements, second ed., University Science Books, Sausalito, US, 1997, Ch. 3.

[24] H.S. Carslaw, J.C. Jaeger, Conduction of Heat in Solids, second ed., Oxford Press, London, 1959.

[25] N. Parikh, J. Allen, R.S. Yassar, Effect of deformation on electrical properties of carbon fibers used in gas diffusion layer of proton exchange membrane fuel cells, J. Power Sources 193 (2009) 766-768.

[26] J. Ramousse, S. Didierjean, P. Lottin, D. Maillet, Estimation of the effective thermal conductivity of carbon felts used as PEMFC gas diffusion layers, Int. J. Therm. Sci. 47 (2008) 1-6.

[27] Web: http://www.boedeker.com/ptfe_p.htm

[28] Web: http://www.fuelcell.com/techsheets/TORAY-TGP-H.pdf

[29] O. Burheim, P.J.S. Vie, J.G. Pharoah, S. Kjelstrup, Ex situ measurements of through-plane thermal conductivities in a polymer electrolyte fuel cell, J. Power Sources 195 (2010) 249-256.

List of figures

Tables

Table 1- Thickness of examined Toray carbon paper TGP-H-120

$PTFE\ (\%)$	5	10	20	30
$t\ (mm)$	0.374	0.376	0.362	0.354

Table 2- Input data for the in-plane thermal conductivity modeling of Toray carbon papers

$r(\mu m)$	$\ell(\mu m)$	$k_s\ (Wm^{-1}K^{-1})$	$k_{PTFE}\ (Wm^{-1}K^{-1})$
4.25	325 [22]	120 [23]	0.649 [24]

Table 3- Summary of experimental results for Toray carbon paper TGP-H-120 with different PTFE contents

$PTFE\ content\ (\%)$	$L\ (mm)$	$Q_{up}(W)$	$Q_{low}(W)$	$R_{layer}(K/W)$	$R_{end}(K/W)$	$k_{eff,in}(W/mK)$
5	11.02	5.72	5.29	63.21	14.27	17.39
	14.34	5.49	5.17	77.79		
10	11.20	5.61	5.35	65.33	15.42	17.33
	14.29	5.53	5.14	78.88		
20	11.37	5.73	5.41	67.13	17.19	17.58
	14.55	5.46	5.25	81.41		
30	11.28	5.77	5.34	66.95	18.05	17.81
	14.67	5.62	5.20	82.31		

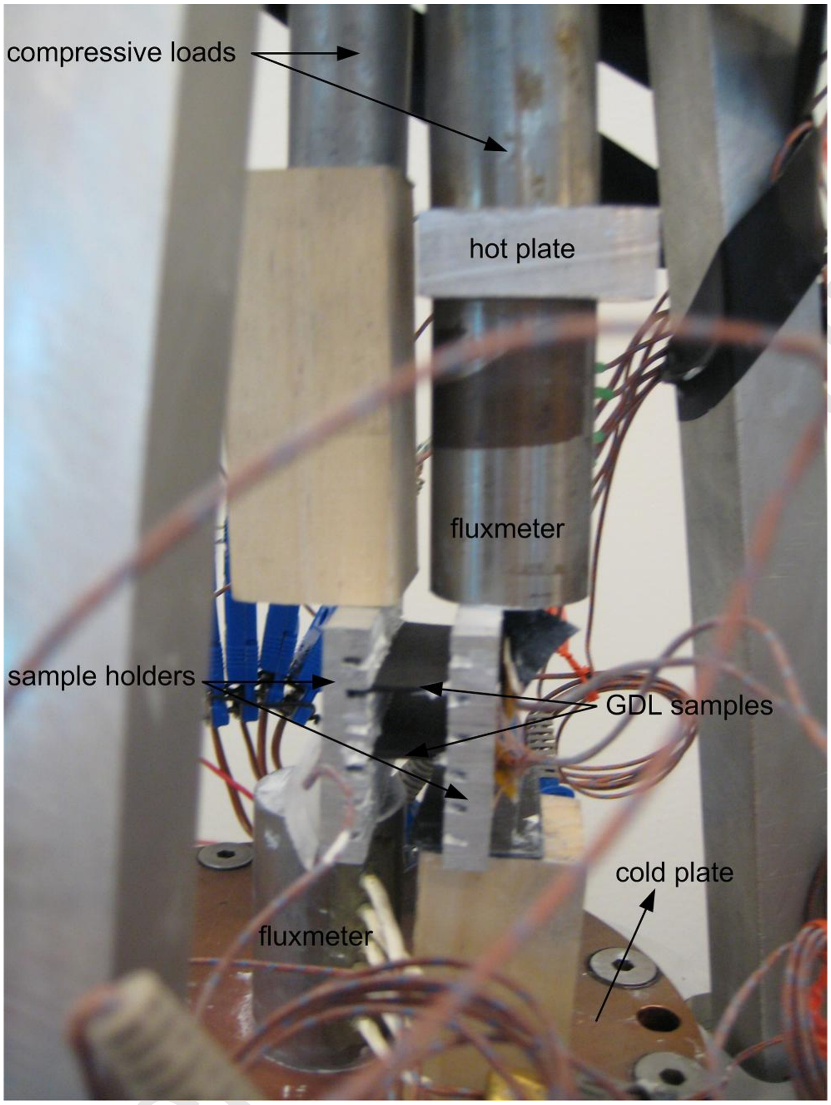
compressive loads
hot plate
fluxmeter
sample holders
GDL samples
cold plate
fluxmeter

Fig. 1(a)

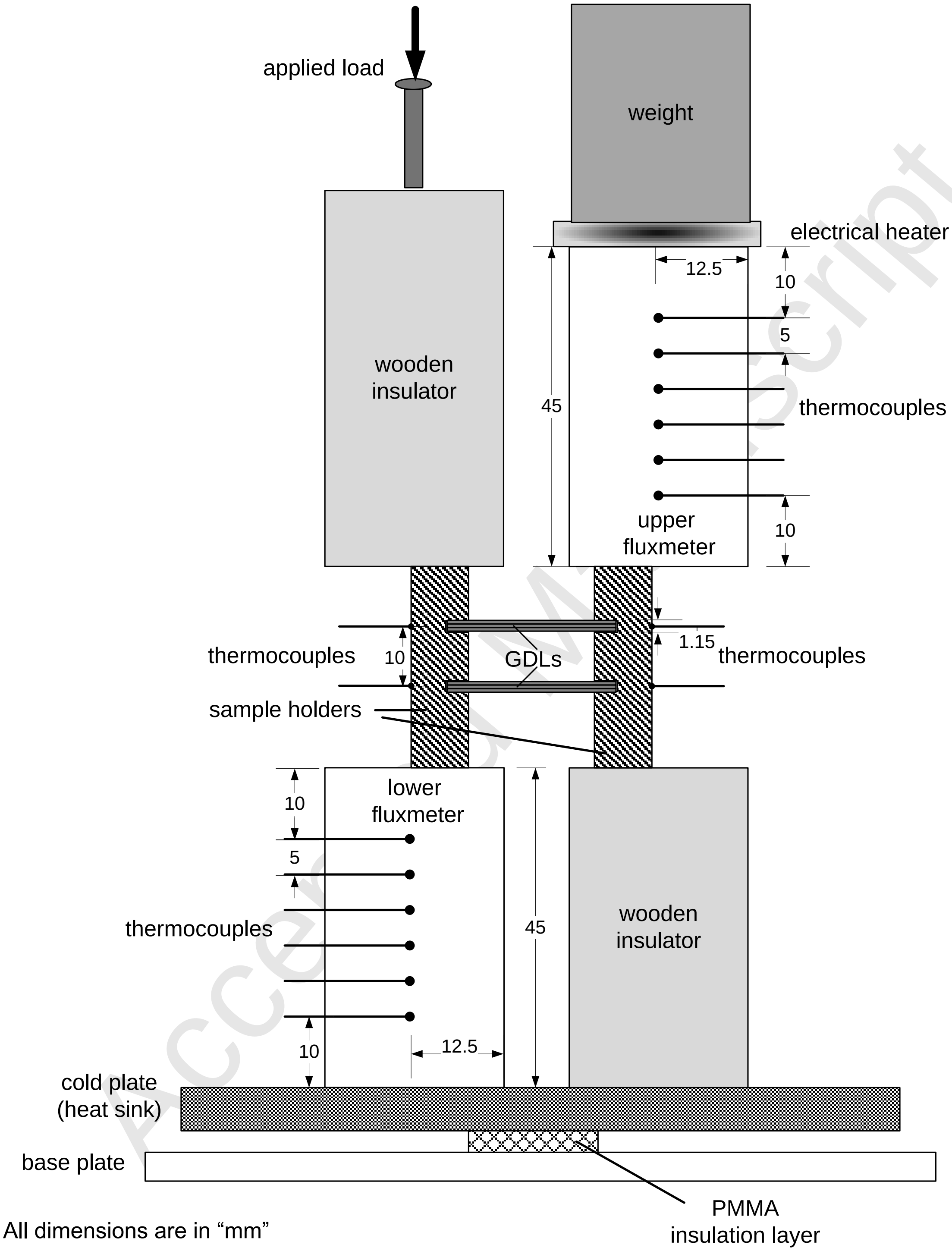
applied load
weight
electrical heater
12.5
10
5
45
wooden insulator
thermocouples
upper fluxmeter
10
thermocouples
10
GDLs
1.15
thermocouples
sample holders
lower fluxmeter
10
5
thermocouples
45
wooden insulator
10
12.5
cold plate (heat sink)
base plate
PMMA insulation layer
All dimensions are in "mm"

Fig. 1(b)

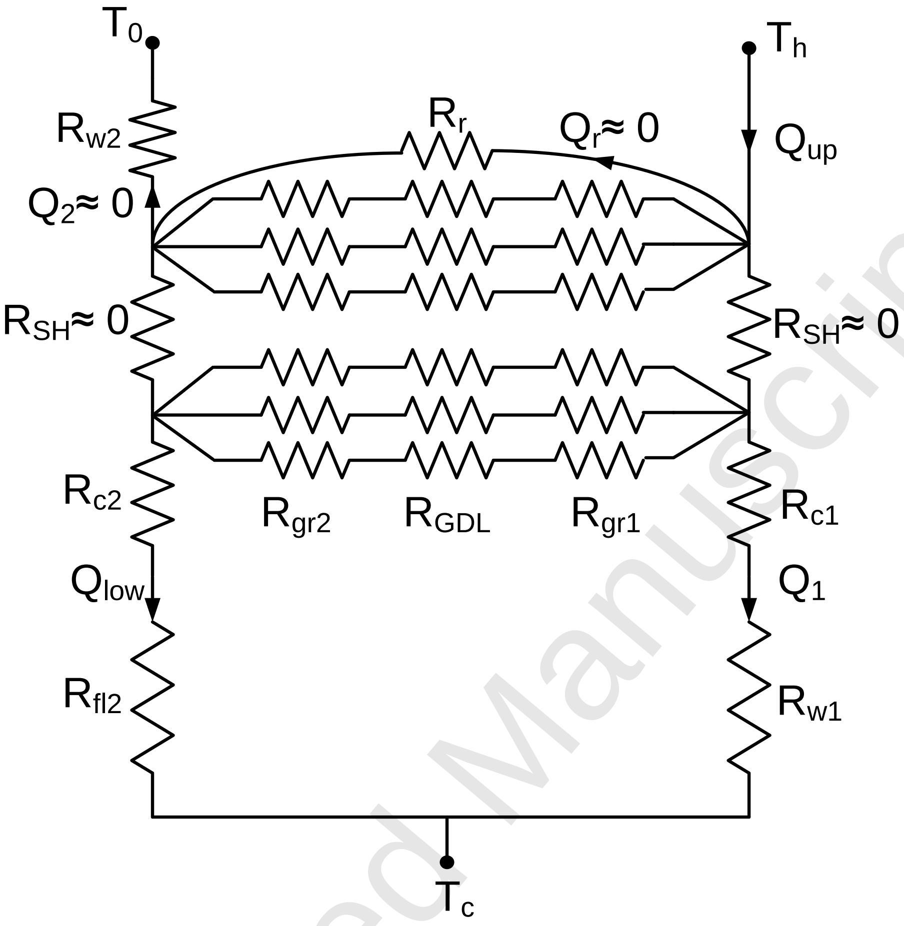
T_0
T_h
R_{w2}
R_r
$Q_r \approx 0$
Q_{up}
$Q_2 \approx 0$
$R_{SH} \approx 0$
$R_{SH} \approx 0$
R_{c2}
R_{gr2}
R_{GDL}
R_{gr1}
R_{c1}
Q_{low}
Q_1
R_{fl2}
R_{w1}
T_c

Fig. 2(a)

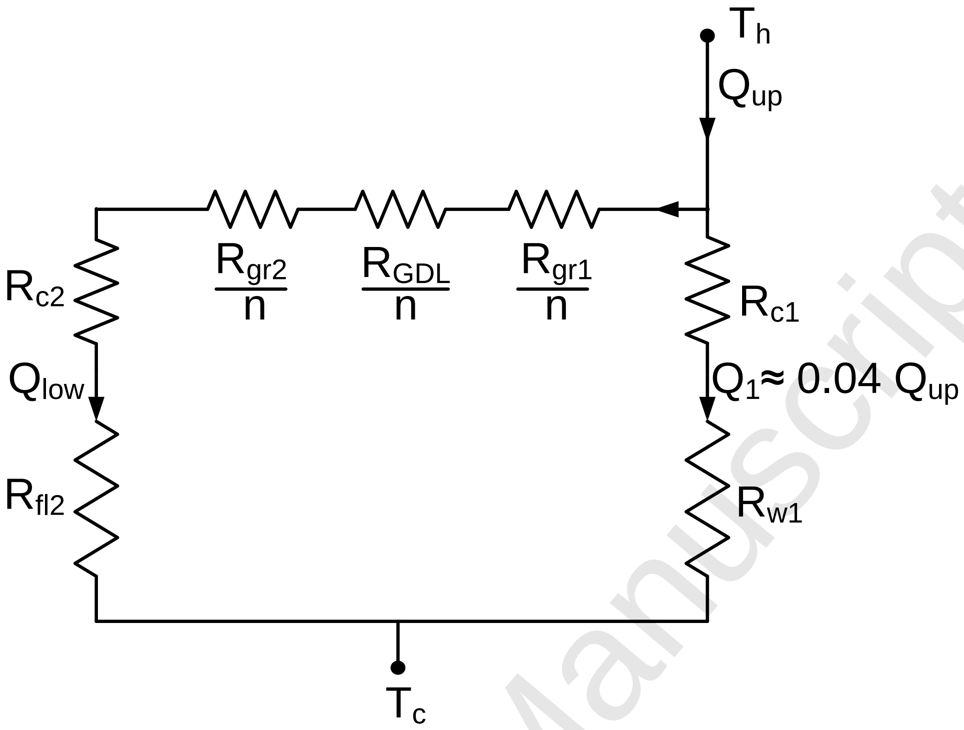
T_h
Q_{up}
$\frac{R_{gr2}}{n}$
$\frac{R_{GDL}}{n}$
$\frac{R_{gr1}}{n}$
R_{c2}
R_{c1}
Q_{low}
$Q_1 \approx 0.04\ Q_{up}$
R_{fl2}
R_{w1}
T_c

Fig. 2(b)

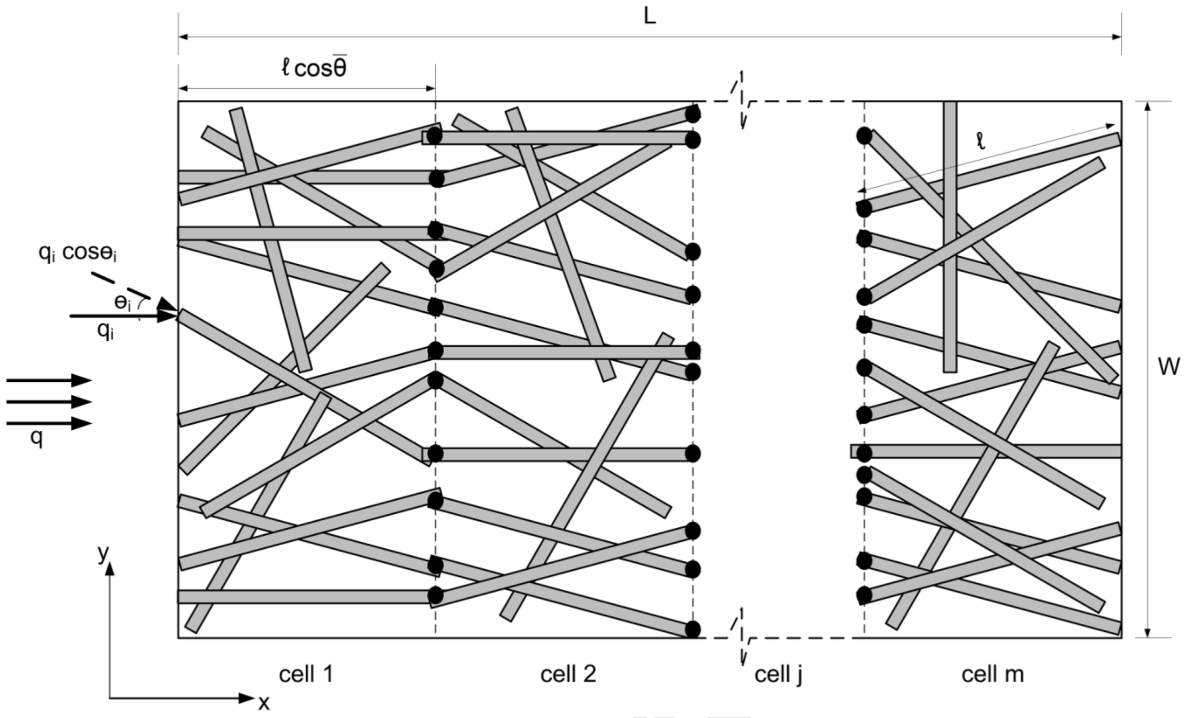
L
ℓ cosθ̄
ℓ
W
$q_i \cos\theta_i$
θ_i
q_i
q
y
x
cell 1
cell 2
cell j
cell m

Fig. 3

Figure 4

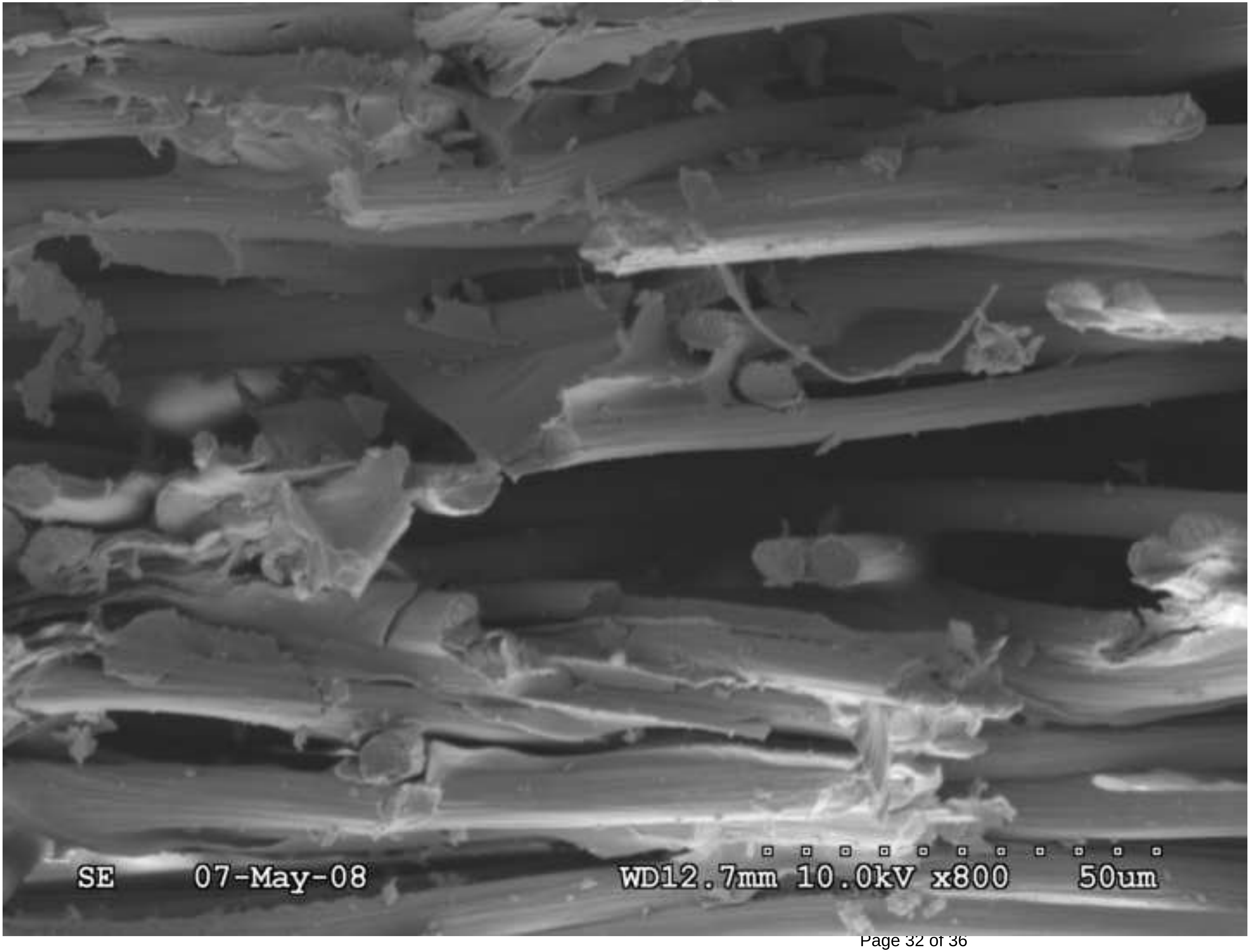

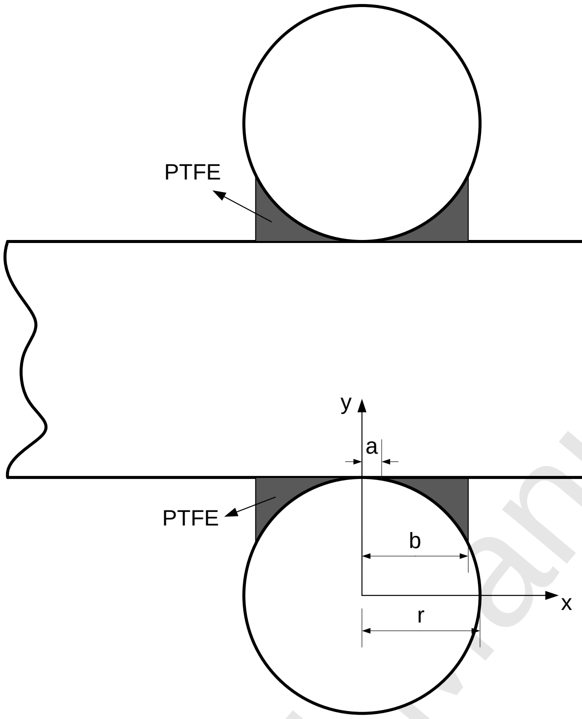

Fig. 5

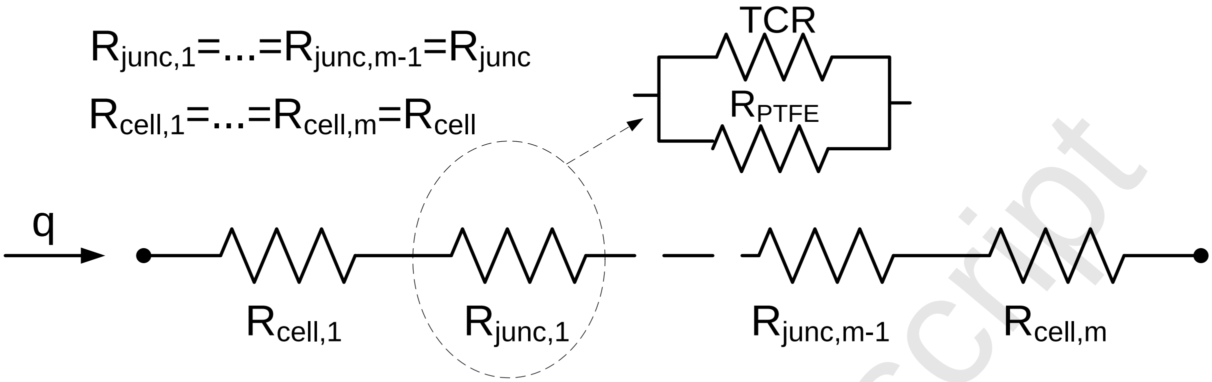
$R_{junc,1}$=...=$R_{junc,m-1}$=R_{junc}
$R_{cell,1}$=...=$R_{cell,m}$=R_{cell}
TCR
R_{PTFE}
q
$R_{cell,1}$
$R_{junc,1}$
$R_{junc,m-1}$
$R_{cell,m}$

Fig. 6

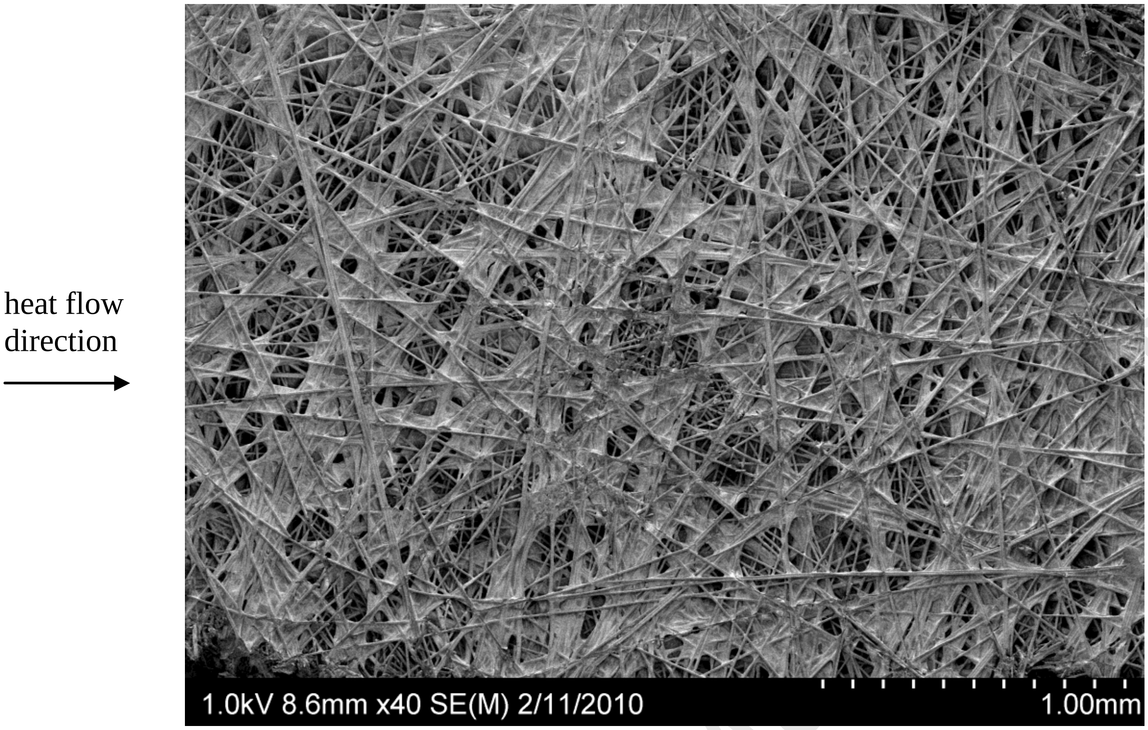

Fig. 7

Figure 8

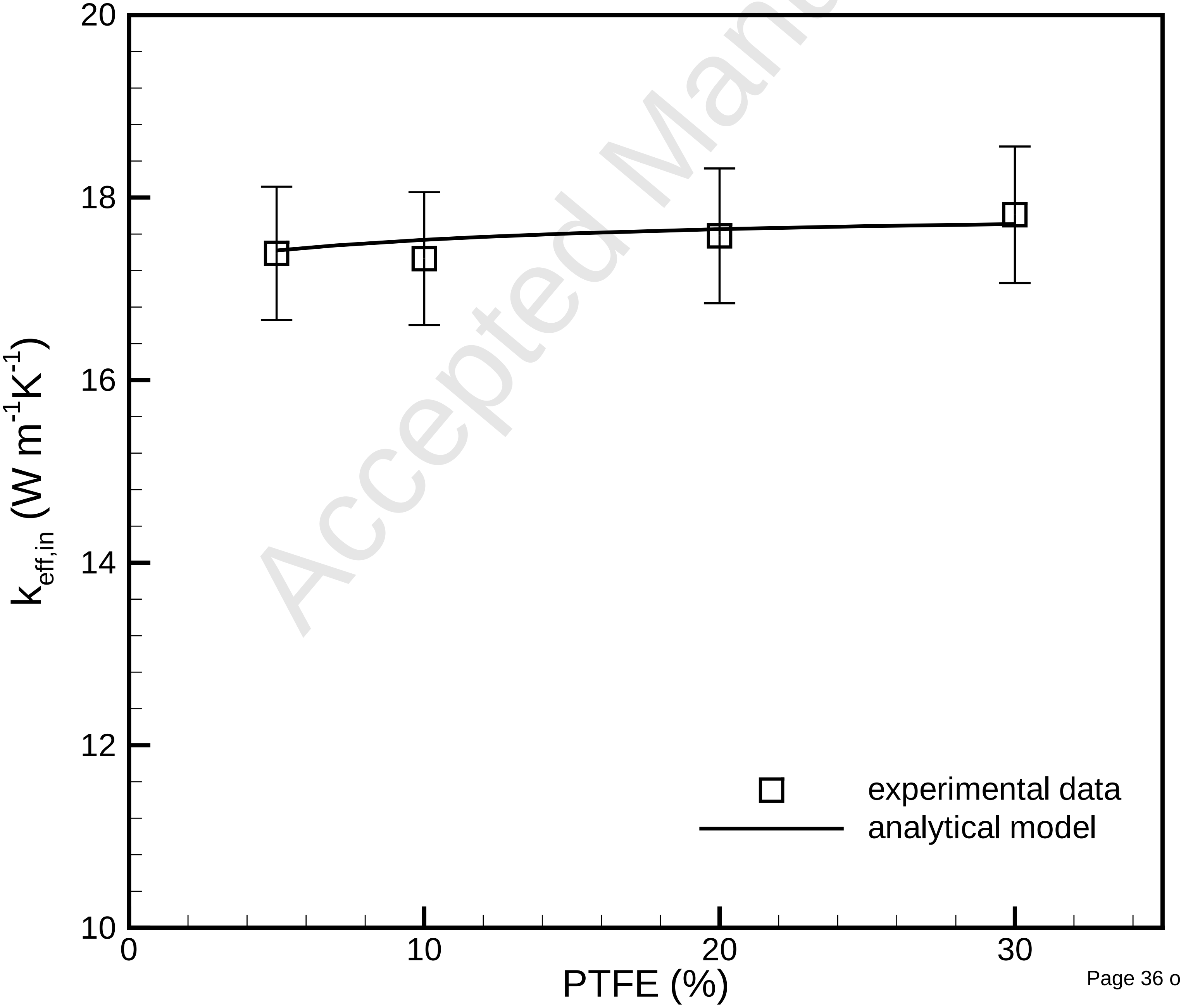
20
18
16
14
12
10
0
10
20
30
PTFE (%)
$k_{eff,in}$ (W m^{-1}K^{-1})
□ experimental data
analytical model

Appendix G

Thermal Conductivity and Contact Resistance of Metal Foams

Submitted to Journal of Physics D: Applied Physics

Thermal conductivity and contact resistance of metal foams

E Sadeghi[1,2,3], S Hsieh[2] and M Bahrami[2]

[1]Deptartment of Mechanical Engineering, University of Victoria, P.O. Box 3055, Victoria, BC, Canada, V8W 3P6

[2]Mechatronic Systems Engineering, School of Engineering Science, Simon Fraser University, Surrey, BC, Canada V3T 0A3

Email: ehsans@uvic.ca

Abstract. Accurate information on heat transfer and temperature distribution in metal foams is necessary for design and modeling of thermal-hydraulic systems incorporating metal foams. The analysis of this process requires determination of the effective thermal conductivity as well as the thermal contact resistance (TCR) associated with the interface between the metal foams and adjacent surfaces/layers. In the present study, a test bed that allows the separation of effective thermal conductivity and thermal contact resistance in metal foams is described. Measurements are performed in a vacuum under varying compressive loads using ERG Duocel aluminum foam samples with different porosities and pore densities. Also, a graphical method associated with a computer code is developed to demonstrate the distribution of contact spots and estimate the real contact area at the interface. Our results show that the porosity and the effective thermal conductivity remain unchanged with the variation of compression in the range of 0 to 2 MPa; but TCR decreases significantly with pressure due to an increase in the real contact area at the interface. Moreover, the ratio of real to nominal contact area varies between 0 to 0.013, depending upon the compressive force, porosity, and pore density.

1. Introduction

Transport phenomena in porous media have been the focus of many industrial and academic investigations [1-4]. The majority of the studies reported in the literature deal with low porosity media such as granular materials and packed beds [1, 2]. Over the last decade, high porosity micro-structures such as open-cell metal foams have received more attention. Interest in these media stems from their

---

[3] Authors to whom any correspondence should be addressed.

relatively low cost, ultra-low density, high surface area to volume ratio, and their ability to mix the passing fluid. These features are highly desirable for a wide variety of applications including microelectronics cooling, aerospace technology, filtration, and compact heat exchangers [3-7]. In majority of these applications, there is an interface between the foam and a solid surface which gives rise to an important phenomenon called thermal contact resistance (TCR) acting against heat transfer in metal foams. Due to high porosity and roughness of the free surface of metal foams, the actual contact area at the interface with a solid surface is very small; this emphasizes the significance of TCR in metal foam-solid surface interface. In some applications, metal foams are brazed to a metallic sheet which may create a perfect contact, but because of high porosity of the medium, TCR still exists due to constriction and spreading of the heat flow passing through the metal plate-foam interface.

A review of the literature indicates that in all previous studies related to heat transfer in metal foams, e.g. [8-15], the TCR was either neglected due to attachment to a metallic sheet to the foam or ‘bundled up’ with the effective thermal conductivity and only effective thermal conductivity values were reported. One fundamental issue with combining the two is that TCR is an *interfacial phenomenon* that is a function of mechanical load and surface characteristics and thermal conductivity of both interfacing surfaces, whereas thermal conductivity is a transport coefficient characterizing the *bulk* medium. Thermal conductivity and TCR should therefore be distinguished. Furthermore, the effect of compression on thermal conductivity and TCR has not been thoroughly investigated.

The objective of this study is to measure the thermal conductivity and contact resistance of metal foams and estimate the size and distribution of contact spots (real contact area) at the interface. The experimental technique developed in this study allows the deconvolution of TCR and thermal conductivity and was used to perform a comprehensive experimental study to determine the effective thermal conductivity and TCR at different compressive loads.

A custom-made test bed was designed and built that enables the measurements of thermal conductivity and TCR of porous media under a vacuum. The test bed was equipped with a loading mechanism that allows the application of various compressive loads on the samples. ERG Duocel aluminum foams with various porosities and pore densities are used in the experiments. The tests are performed under a vacuum, where the test column was surrounded by an aluminum radiation shield to limit the radiation heat losses. The effective thermal conductivity and TCR are deduced from the total thermal resistance measurements by performing a series of experiments with aluminum foam samples of various thickness and similar micro-structure, i.e. porosity and pore density. Effects of compression, porosity, and pore density are studied on the effective thermal conductivity and TCR.

To estimate the actual contact area at the metal foam-solid interface, a pressure sensitive carbon paper is placed between the foam and the solid surface to print the contact spots at different compressive loads. A computer code is then developed using MATLAB to analyze the produced images and calculate the size and distribution of contact spots.

2. Thermal conductivity and TCR measurements

The schematic of the test bed for thermal measurements is shown in figure 1. The test chamber consists of a stainless steel base plate and a bell jar enclosing the test column. The test column consists of, from top to bottom: the loading mechanism, the steel ball, the heater block, the upper heat fluxmeter, the sample, the lower fluxmeter, the heat sink (cold plate), the load cell, and the poly methyl methacrylate (PMMA) layer. The heater block consists of circular flat copper in which cylindrical pencil-type electrical heaters are installed. The designed cold plate consists of a hollow copper cylinder, 1.9 cm high and 15 cm diameter. Cooling is accomplished using a closed loop water-glycol bath in which the coolant temperature can be set. The cold plate is connected to the chiller unit which adjusts the cold water temperature. A 1000 lbs load cell is used to measure the applied load to the sample. The fluxmeters were made of a standard electrolyte iron material. In this study, the cold plate temperature and the power of the electrical heater were set on 0°C and 12 W, respectively.

To measure temperatures, six T-type thermocouples were attached to each fluxmeter at specific locations shown in figure 1. The thermocouples were located 5 mm apart with the first one 10 mm from the contact surface. The thermal conductivity of the iron fluxmeter was known and used to measure the heat flow rate transferred through the contact interface. The samples used in this study were open-cell aluminum foams. These Duocel foams were produced through a proprietary process developed by ERG in which the resulting foam has the identical chemical composition of the base alloy used. The foam was made from aluminum alloys of 6101 and cut in cylindrical shapes with the diameter of 25 mm and then polished. Aluminum foam samples with the porosity range of 90 to 96% and pore density of 10 and 20 PPI were used in this study; see table 1 for more details.

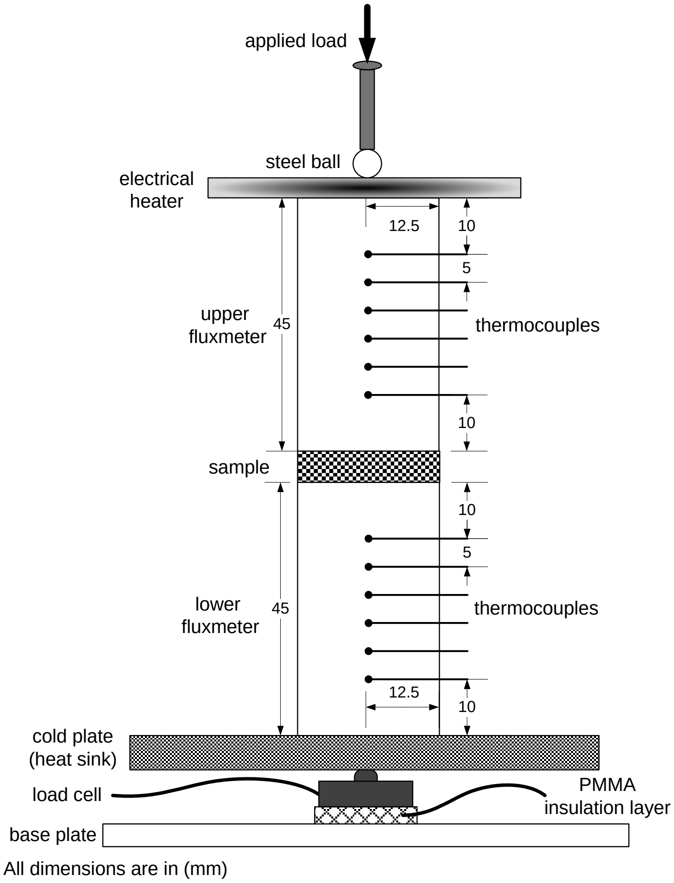

Figure 1. Schematic of the test bed for thermal measurement.

Table 1. Properties of the studied Al foam samples.

sample number	#1	#2	#3	#4
porosity	0.903	0.906	0.945	0.953
pore density (PPI)	10	20	10	20
thickness (mm)	13.93 17.89	13.90 17.91	13.92 17.95	13.93 17.96

2.1. Test procedure

To study heat conduction only through the solid ligaments and contact surfaces, experiments were conducted under a vacuum. A vacuum level of 10^{-5} mbar was achieved under the test chamber using a vacuum machine. Temperatures and pressure were recorded at various compressive loads when steady-state conditions were achieved; to reach thermal equilibrium all the experiment's parameters were kept constant and carefully monitored for approximately 4-5 hours for each data point. The effects of compression were investigated over the range of 0.3 to 2 MPa.

The temperature gradient between the hot and cold plates results in essentially one-dimensional heat conduction from the top to the bottom of the test column. Radiation heat transfer is negligible due to relatively low absolute temperature levels as well as small temperature drop at the interface and insignificant temperature differences between the neighboring ligaments inside the foam. As a result, one can conclude the heat transfer in the present experiment is mostly due to conduction. The heat transfer through the fluxmeters can be determined using the Fourier's equation.

$$Q = -kA\frac{dT}{dz} \tag{1}$$

where, dT/dz is the temperature gradient along the test column, k is the thermal conductivity of the fluxmeters, and A is the cross-sectional area of samples/fluxmeters. The temperatures at the top and bottom contact surfaces can be extrapolated through the measured heat flux. The measured total thermal resistance at each pressure, R_{tot}, includes the sample (bulk) thermal resistance and the thermal contact resistance (at the top and bottom interfaces) and can be expressed as:

$$R_{tot} = R_{MF} + TCR = \frac{\Delta T_{ul}}{Q} \tag{2}$$

where, ΔT_{ul} is the temperature difference between the upper and the lower contact surfaces. R_{MF} and TCR are the metal foam resistance and the total contact resistance (summation of contact resistance at the top and the bottom surfaces), respectively.

To deconvolute thermal conductivity and TCR, two experiments were performed with samples of different thicknesses; but with identical micro-structural parameters. Due to identical micro-structure and solid surface characteristics at the top and the bottom interfaces, contact resistances for both samples can be considered equal at the same pressure. Applying Eq. (2) to both measurements and subtracting them yields the effective thermal conductivity:

$$k_{eff} = \frac{t_1}{R_{MF1}A} = \frac{t_2}{R_{MF2}A} \tag{3}$$

$$k_{eff} = \frac{t_1 - t_2}{(R_{tot1} - R_{tot2})A} \tag{4}$$

where, $t_1$and t_2 are the two different thicknesses of the Al foam sample at a specific applied pressure, and A is the cross-sectional area of the sample. To investigate the effect of compression on the sample thickness, Al foam samples with different porosities $(0.9 < \varepsilon < 0.96)$ and pore densities were compressed step by step using a standard tensile-compression machine. Thickness variation was measured for all of the samples at different pressures from 0 to 2 MPa using a Mitutoyo digital micrometer with the accuracy of 1 μm. The results show that the maximum thickness variation is less than 1.5% that may be neglected. Equation (4) can be used to find the effective thermal conductivity; the TCR can then be calculated by Eq. (2).

2.2. *Uncertainty analysis*

Considering the relationships for evaluating the effective thermal conductivity and the thermal contact resistance, i.e. Eqs.(4), (2), the relevant parameters in the analysis can be expressed as:

$$R_{tot} = f(Q, \Delta T, t, A, P_c, \phi_s) \tag{5}$$

The main uncertainty in these experiments is due to errors in determining the heat flux through the sample which leads to a maximum error of 3.2%. The maximum uncertainties for the thermocouples and the data acquisition readings are $\pm 1°\mathrm{C}$ which introduces a maximum error of 1.7% between the interfaces of the sample and fluxmeters. The relative density of the similar samples with two different thicknesses was measured and the difference was used as a representative of the morphological uncertainty. This uncertainty as well as those associated with the load cell, thickness, and cross-sectional area measurements and are listed in table 2. The maximum uncertainty for the thermal resistance measurements can be calculated from [16]:

$$\frac{\delta R_{tot}}{R_{tot}} = \sqrt{\left(\frac{\delta Q}{Q}\right)^2 + \left(\frac{\delta \Delta T}{\Delta T}\right)^2 + \left(\frac{\delta t}{t}\right)^2 + \left(\frac{\delta A}{A}\right)^2 + \left(\frac{\delta P_c}{P_c}\right)^2 + \left(\frac{\delta \phi_s}{\phi_s}\right)^2} \tag{6}$$

Table 2. Uncertainty of involving parameters in the analysis.

$\delta Q/Q$	$\delta \Delta T/\Delta T$	$\delta t/t$	$\delta A/A$	$\delta P_c/P_c$	$\delta \phi_s/\phi_s$
3.2%	1.7%	0.5%	0.8%	2.5%	2.2%

For the present study, the maximum uncertainty is estimated to be $\pm 5\%$.

3. Morphology of contact spots

To find the size and distribution of contact spots, a sheet of carbon copy paper along with a white paper was placed on top and bottom of the samples. The assembly was compressed in a standard tensile-compression machine and the contact spots were printed on the white paper. The printed images were captured with a high resolution camera. An image processing technique implemented in MATLAB enabled accurate evaluation of the contact area at the metal foam-solid interface. The image was first masked with green color that highlighted the area of interest in a given RGB image shown in figure 2.

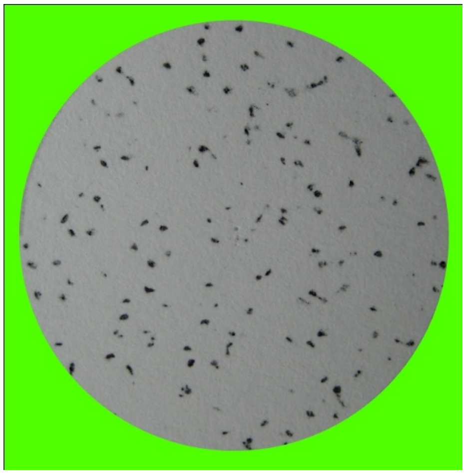

Figure 2. Masked image, Al foam with 95.3% porosity and 20 PPI at P_c=1.53 MPa.

Analyzing the green channel of the RGB image, the total pixel count/area of the sample material can be found. Once the circular area of interest was found, the RGB image was converted into an 8-bit greyscale image where contact point can be extracted through image filtering by contrast. The contact points were seen as dark spots in the image, where lighter shades of grey were shadows or blur caused by the camera. To differentiate contact spots and shadows, each pixel in the image was compared to their neighbouring pixels as seen in figure 3.

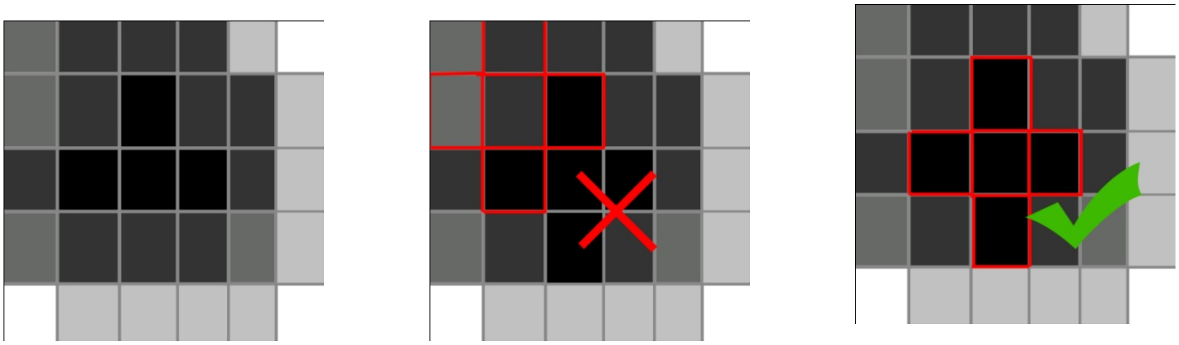

(a) (b) (c)

Figure 3. Contrast filtering.

Each pixel was individually scanned in a cross pattern as seen in figure 3 (b), the pixel in the center of the cross was compared with the pixel directly above, below, left and right. The dark/lightness of the gradient was being monitored while contrast was being analyzed simultaneously. The centering pixel in figure 3 (b) appeared to be dark grey, and there is a change in its contrast with the surrounding pixels, hence, it is almost definite that this particular spot is a shadow and not a contact point. However, in figure 3 (c), the center pixel met both requirements: i) being dark compared to the background color, and ii) negligible variation in contrast with the neighbouring pixels. Therefore, this location can be considered as a contact point. Each contact point was then highlighted with a different color which is shown in figure 4.

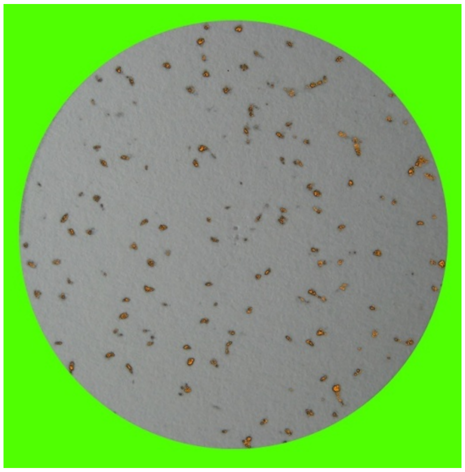

Figure 4. Highlighted contact points, Al foam with 95.3% porosity and 20 PPI at P_c=1.53 MPa.

After scanning through the entire image, the pixel count of the contact spot is compared with the total area of the interface (circle shown in figure 4), and then the real contact area ratio is calculated.

4. Results and discussion

The measurements were taken at different compressive loads in a vacuum to study the effects of compressive load on TCR and effective thermal conductivity. Also, to find the actual contact area at the metal foam-solid surface interface, separate compression tests were performed and the produced images were analyzed using the developed image processing technique described in section 3.

Figure 5 shows the variation of the effective thermal conductivity with compression at different porosities and pore densities. The effective conductivity decreases with an increase in the porosity; however, the effect of pore density seems to be insignificant. Lower porosity values are associated with a higher volume of conductive materials which provides high conductive paths for the heat flow. Also, the effect of compressive load on the thermal conductivity is insignificant over the studies pressure range. Our measurements show that the highest bulk deformation occurred under the compression is 1.5 % which does not have a significant impact on the micro-structure. However, higher compressive loads, which produce larger deformations, may affect the thermal conductivity as reported in [4]. Table 3 summarizes the averaged values of the measured thermal conductivity for the metal foam samples used in the present study.

Table 3. Averaged thermal conductivity of different samples over the compression range of 0-2 MPa.

sample number	#1	#2	#3	#4
k_{eff} (W/mK)	7.37	6.84	4.53	3.78

Present experimental data are compared with existing experimental data in figure 6. Majority of existing data [9-11, 14] were reported for Al foam-air; but since the thermal conductivity of air is very low, its contribution in the effective thermal conductivity may be negligible. The compressive load for the existing experimental data was not reported; therefore, the mean values of the present data at different compressive loads are used for the comparison purposes. As shown, the present experimental data agree with the majority of existing data at different porosities; however, Paek et al. [9] results fall below the other data. It should be noted that the TCR for the data collected from other sources [9-11, 14] is negligible since the foam samples were brazed to Al sheets, and the temperatures of the Al sheets near the contact points were used for evaluating thermal conductivity.

Figure 7 shows the thermal contact resistance of the examined Al foam samples at different compressive loads. It can be seen that the compressive load has a pronounced effect on TCR. In addition, TCR is more sensitive to porosity rather than pore density. The real contact area at the foam-solid interface increases with an increase in the compressive load which results in a considerable reduction of TCR. Also, as expected, samples with higher porosities have lower solid material in contact region which results in a higher TCR. Furthermore, the number of contact spots increases with an increase in the pore density; however, these contact spots have a smaller size and different surface profile. As a result of these competing effects, the effect of pore density on contact resistance is not significant.

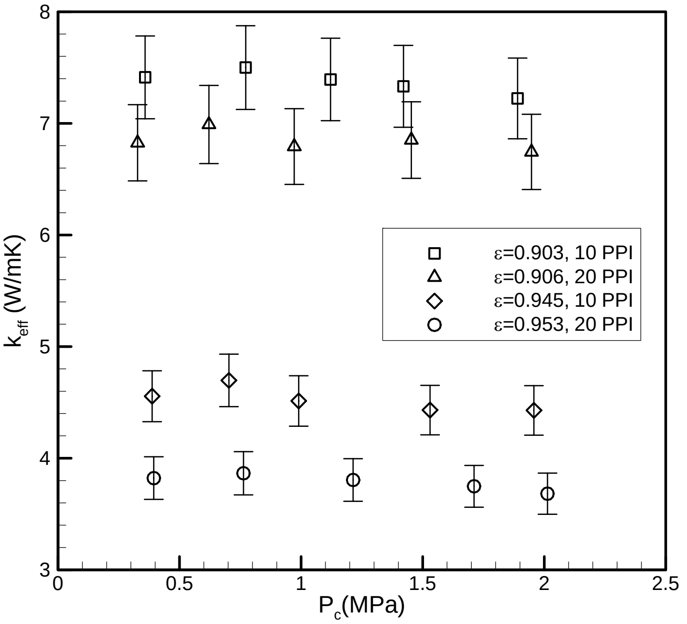

Figure 5. Effective thermal conductivity of different Al foam samples over a range of compression.

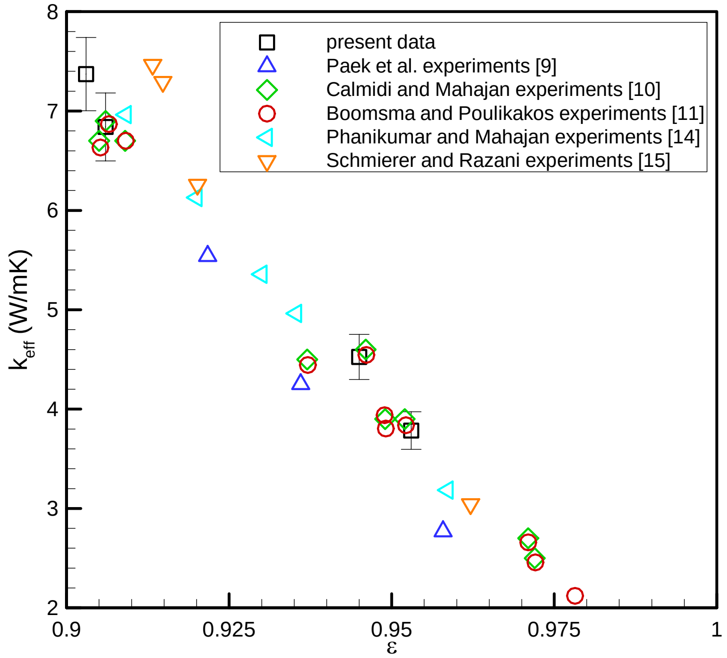

Figure 6. Present experimental data for Al foam-vacuum in comparison with existing experimental data for Al foam-air (Ref. [15] data is for Al foam-vacuum).

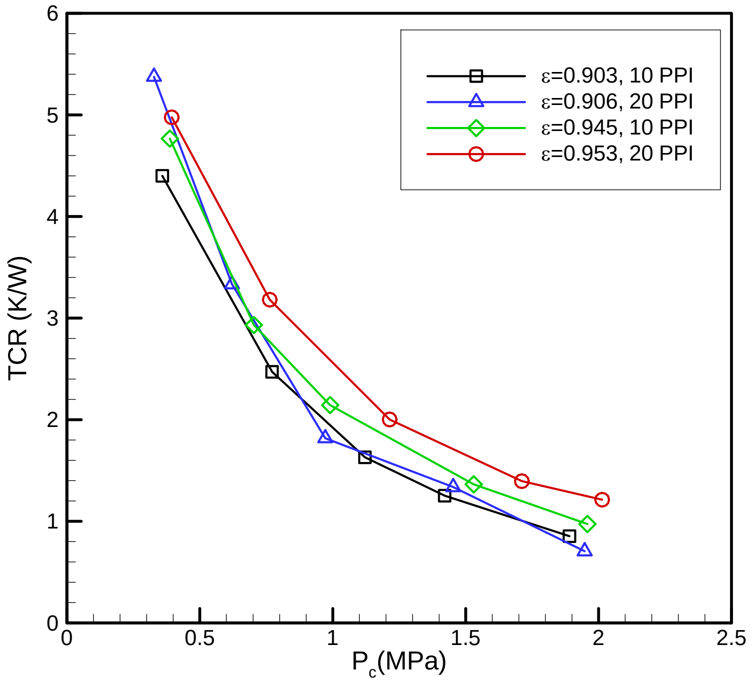

Figure 7. TCR of different Al foam samples over a range of compression.

Distribution of contact spots for different Al foam samples is shown in figure 8 (a)-(d) for a moderate pressure and figure 8 (e)-(h) for a high pressure. As shown, the total contact area increases with an increase in the foam density. Also, higher pore densities provide a larger number of contact points which can reduce the TCR as shown in figure 7. The ratio of real to nominal contact area η, which is found from the analysis of the printed images, is shown in figure 9; the nominal contact area was considered equal as the cross-sectional area. There is a small difference between the contact area ratio of the bottom and top surfaces due to different distribution of ligaments on these surfaces, therefore, in our analysis the average contact area ratio is considered.

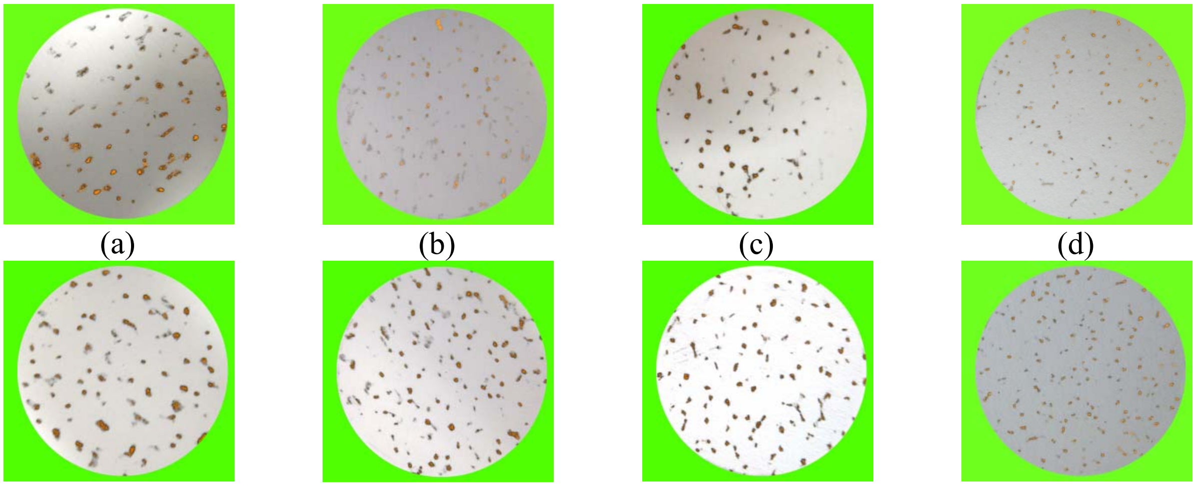

(a) (b) (c) (d)

(e) (f) (g) (h)

Figure 8. Highlighted contact points for various Al foam samples: (a) ε =90.3%, 10 PPI at P_c=1.43 MPa; (b) ε =90.6%, 20 PPI at P_c=1.02 MPa; (c) ε =94.5%, 10 PPI at P_c=1.32 MPa; (d) ε =95.3%, 20 PPI at P_c=1.02 MPa; (e) ε =90.3%, 10 PPI at P_c=2.85 MPa; (f) ε =90.6%, 20 PPI at P_c=2.44 MPa; (g) ε =94.5%, 10 PPI at P_c=3.06 MPa; (h) ε =95.3%, 20 PPI at P_c=3.06 MPa.

Reviewing figures 7-9 shows that for a relatively high pressure, the number and total area of contact spots increase with an increase in the pore density and foam density which results in a reduction of the TCR.

However, in low contact pressures, $P_c < 0.5\ MPa$, the contact surface morphology becomes more important and dominates the effects of pore density and porosity. Therefore, the smaller contact area (higher TCR) of denser foams such as the foam with ε=0.906 can be due to a higher surface roughness.

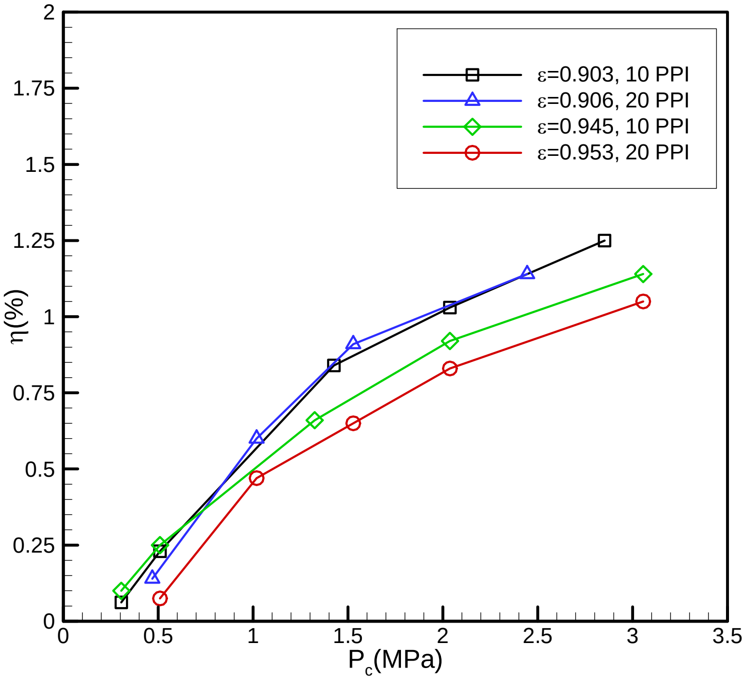

Figure 9. Total contact area to cross-sectional area ratio for various Al foam samples under compression.

Figure 10 shows the TCR to total thermal resistance ratio of examined Al foam samples with the average thickness of 13.92 mm at different compressive loads. As can be seen, TCR is the dominant resistance at low compressive loads, $P_c < 0.3\ MP$, constituting more than 50% of the total resistance. This contribution decreases for all the samples with an increase in the compressive load. It is very interesting to observe that although the absolute value of TCR increases with an increase in porosity, its ratio to the total resistance decreases. This is due to the fact that both foam bulk resistance and TCR increase with an increase in porosity, but this increase is higher for the bulk resistance.

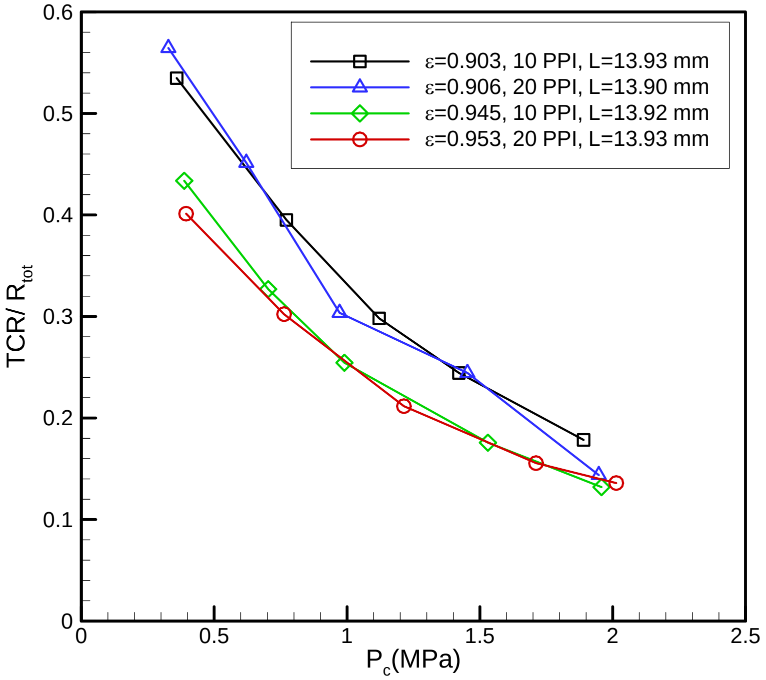

Figure 10. TCR to total thermal resistance ratio for different Al foam samples under compression.

5. Summary and Conclusions

A test bed was designed and built to measure the thermal conductivity and thermal contact resistance of metal foams under various compressive loads. Also, a computer program associated with an experimental set-up was developed to find the distribution and total size of actual contact area at the metal foam-solid surface interface. The analytical modeling of thermal conductivity and thermal contact resistance will be provided a companion paper. The present experimental data for the effective thermal conductivity are in good agreement with existing data over a range of porosities. Our results show that the effective thermal conductivity increases with an increase in the foam density, but it is relatively insensitive to compressive load in the range of 0-2 MPa.

An important finding is the large contribution of thermal contact resistance to the total thermal resistance, more than 50%, for relatively low compressive loads. The high values of TCR are related to very small ratio of contact area to the cross-sectional area; the maximum ratio is 1.3% at the contact pressure of 3

MPa. TCR is more sensitive to the compressive load rather than the porosity and pore density; however, it slightly decreases with an increase in the foam density.

This work provided new insights on the importance of thermal contact resistance and has helped clarify the impact of this key interfacial phenomenon on the thermal analysis of metal foams.

Acknowledgements

The authors are grateful for the financial support of the Natural Sciences and Engineering Research Council (NSERC) of Canada, and the Canada Research Chairs Program. The authors would like to thank Dr. Ned Djilali for his useful suggestions during the work.

References

[1] Kaviany M 1995 *Principles of Heat Transfer in Porous Media* (New York: Springer)

[2] Bahrami M, Yovanovich M M and Culham J R 2006 Effective thermal conductivity of rough spherical packed beds *Int. J. Heat Mass Transfer* **49** 3691-3701

[3] Dukhan N, Picon-Feliciano R and Alvarez-Hernandez A R 2006 Heat transfer analysis in metal foams with low conductivity fluids *J. Heat Transfer* **128** 784-792

[4] Ozmat B, Leyda B and Benson B 2004 Thermal applications of open-cell metal foams *Materials and Manufacturing Processes* **19** 839-862

[5] Bhattacharya A, Calmidi V V and Mahajan R L 2002 Thermophysical properties of high porosity metal foams *Int. J. Heat Mass Transfer* **45** 1017-103

[6] Hunt M L and Tien C L 1988 Effects of thermal dispersion on forced convection in fibrous media *Int. J. Heat Mass Transfer* **31** 301-309

[7] Mahjoob S and Vafai K 2008 A synthesis of fluid and thermal transport models for metal foam heat exchangers *Int. J. Heat Mass Transfer* **51**, 3701-3711

[8] Zhao CY, Lu T J, Hodson H P and Jackson J D 2004 The temperature dependence of effective thermal conductivity of open-celled steel alloy foams *Materials Science and Engineering A* **367** 123-131

[9] Paek J W, Kang B H, Kim S Y and Hyun J M 2000 Effective thermal conductivity and permeability of aluminum foam materials *Int. J. Thermophysics* **21** 453-464

[10] Calmidi V V and Mahajan R L 1999 The effective thermal conductivity of high porosity fibrous metal foams *J. Heat Transfer* **121** 466-471

[11] Boomsma K and Poulikakos D 2001 On the effective thermal conductivity of a three-dimensionally structured fluid-saturated metal foam *Int. J. Heat Mass Transfer* **44** 827-836

[12] Krishnan S, Garimella S and Murthy J Y 2008 Simulation of thermal transport in open-cell metal foams: Effects of periodic unit-cell structure *J. Heat Transfer* **130** 024503-024507

[13] Babcsan N, Meszaros I and Heman N 2003 Thermal and electrical conductivity measurements on aluminum foams *Materialwiss. Werkstofftech* **34** 391-394

[14] Phanikumar M S and Mahajan M L 2002 Non-darcy natural convection in high porosity metal foams *Int. J. Heat Mass Transfer* **45** 3781-3793

[15] Schmierer E N and Razani A 2006 Self-consistent open-celled metal foam model for thermal applications *J. Heat Transfer* **128** 1194-1203

[16] Taylor J R 1997 *An Introduction to Error Analysis: The Study of Uncertainties in Physical Measurements* (Sausalito, US: University Science Books)

Appendix H

Radiation Heat Transfer

The following is an investigation to study the relative importance of the radiation heat transfer inside the porous media as well as at the interface with other solid surfaces such as fluxmeters. The maximum radiation heat transfer between the surface i and the surface j is the blackbody radiation exchange which can be found from [67]:

$$Q_{ij} = A_i F_{ij} \sigma (T_i^4 - T_j^4), \tag{H.1}$$

where $\sigma = 5.67 \times 10^{-8} W^2/m^2K^4$ and F_{ij} are the Stefan-Boltzmann constant and the view factor, respectively. The view factor F_{ij} is defined as the fraction of the radiation that leaves A_i and is intercepted by A_j. Considering the blackbody radiation and the maximum temperature difference at the contact surface and neglecting the effect of view factors, the radiation heat transfer as shown in Table H.1 is less than 1% of the conduction heat transfer. It should be noted that this is the maximum value and in reality, the contribution of radiation is much less. Similar calculations have been done for the metal foam samples and the data are reproted in Table H.2. The temperature value at a quarter thickness of the metal foam sample is considered as a representation of the ligament temperature. This is an exageration and in practice, due to the complex interconected structure of metal foams, the contact surface hardly can see a surface at a quarter thickness. Also, the emissivity of aluminum is very low (0.07-0.09); therefore, the value found for the radiation heat transfer in Table H.2 is reduced in practice by atleast one order of mignutude and becomes negligible.

Figure H.1 shows the neighboring fibers/ligaments that can have radiation exchange with a selected fiber/ligament. This is a simplification made to estimate the contribution of radiation in the heat transfer inside the medium. Considering that

$T_{fl}(°C)$	$T_{GDL}(°C)$	$Q_c(W)$	$Q_r(W)$	Q_r/Q_c
103.3	70.7	26.1	0.17	0.0065

Table H.1: Contribution of conduction and radiation in heat transfer from the upper fluxmeter to the GDL

$T_{fl}(°C)$	$T_{MF}(°C)$	$Q_c(W)$	$Q_r(W)$	Q_r/Q_c
160.2	109.5	10.4	0.385	0.037

Table H.2: Contribution of conduction and radiation in heat transfer from the upper fluxmeter to the metal foam

the fiber/ligament i acts as a blackbody and absorbs all the heat radiation from the neighboring fibers/ligaments, the maximum radiation heat transfer can be estimated. These values are $1.7 \times 10^{-6} W$ and $3 \times 10^{-4} W$ for the GDL and metal foam samples, respectively. Also, the view factor values for metal foam and GDL structures are small. For instance, with a typical pore diameter of $16 - 25 \mu m$ and a fiber diameter of $6 - 9 \mu m$ for GDLs, the maximum view factor between two neighboring fibers found from the following equation [67] is 0.06.

$$F_{ij} = \frac{\left\{ \pi + \sqrt{(2+S)^2 - 4} - (2+S) - 2Cos^{-1}(\frac{2}{2+S}) \right\}}{2\pi}, \tag{H.2}$$

where $S = 2d_p/d_f$; d_p and d_f are the pore diameter and fiber diameter, respectively. It can be concluded from our analysis that the radiation heat transfer is negligible for the temperature range of this study.

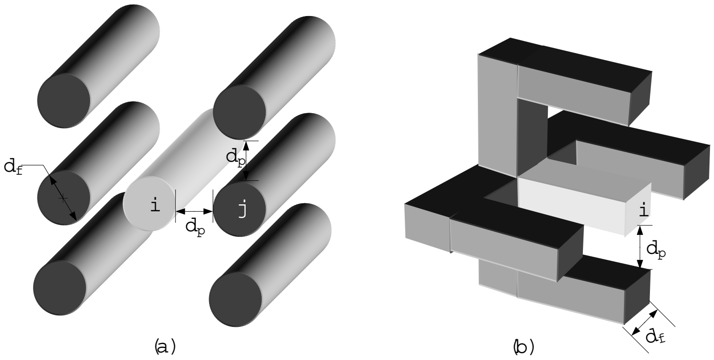

Figure H.1: Radiation cells including neighboring fibers/ligaments considered for: (a)GDL and (b) metal foam

Appendix I

Uncertainty Analysis

Consider F is the measured parameter in the experiment which is a function of independent variables $x_1, x_2, ..., x_n$. The maximum uncertainties in the F can be expressed by the quadratic sum of uncertainties in each variable [**?**].

$$\frac{\delta F}{F} = \sqrt{\frac{\delta x_1}{x_1}^2 + \frac{\delta x_2}{x_2}^2 + ... + \frac{\delta x_n}{x_n}^2}, \tag{I.1}$$

where $\delta F/F$ is the uncertainty in the parameter F and $\delta x_i/x_i (i = 1, ..., n)$ is the uncertainty in the variable i.

I.1 Through-Plane Thermal Conductivity and Thermal Contact Resistance Measurement of GDLs and Metal Foams

The primary measured parameter in the through-plane thermal experiment of GDLs is the total thermal resistance which can be described as a function of the heat flow rate, the temperature drop between the fluxmeters, the sample thickness, the sample cross-sectional area, and the contact pressure.

$$R_{tot} = f(Q, \Delta T, t, A, P_c). \tag{I.2}$$

The main uncertainty in these experiments is due to errors in determining the heat flux through the sample which leads to a maximum error of 4.3%. The maximum uncertainties for the thermocouples and the data acquisition readings are $\pm 1°C$ which introduces a maximum error of 1.3% between the interfaces of the sample and fluxmeters. Other uncertainties including those associated with the load cell, thickness, and cross-sectional area measurements and are listed in Table I.1. The maximum uncertainty for the thermal resistance measurements can be calculated from Eqs. (I.1), (I.2). The maximum uncertainty is estimated to be ±6%. Similar test test bed was used for the thermal conductivity and thermal contact resistance measurements of metal foams. Therefore, a similar error analysis can be applied which results in a maximum uncertainty of ±4.5% for these measurements. The uncertainties related to each individual parameter of the experiment is reported in Table I.2.

$\delta Q/Q$	$\delta \Delta T/\Delta T$	$\delta t/t$	$\delta A/A$	$\delta P_c/P_c$
4.3%	1.3%	2.7%	1.6%	2.5%

Table I.1: Uncertainty of involving parameters in the through-plane thermal resistance measurement

$\delta Q/Q$	$\delta \Delta T/\Delta T$	$\delta t/t$	$\delta A/A$	$\delta P_c/P_c$
3.2%	1.7%	0.5%	0.8%	2.5%

Table I.2: Uncertainty of involving parameters in the thermal resistance measurements of metal foams

I.2 In-Plane Thermal Conductivity Measurement of GDLs

The in-plane thermal resistance can be described as a function of the heat flow rate, the temperature drop between the sample holders, and the thickness, the width, and the length of the sample.

$$R_{tot} = f(Q, \Delta T, t, W, L). \tag{I.3}$$

The main uncertainty in our experiments is due to errors in determining the heat flux through the sample holders which leads to a maximum error of 3.7%. The maximum uncertainties for the thermocouples and the data acquisition readings are $\pm 1°C$ which introduces a maximum error of 1.8% between two sample holders. Other uncertainties including those associated with the width, thickness, and length measurements are 0.3%, 0.3%,and 0.9%, respectively. The maximum uncertainty for this experiment was found to be ±4.2% by substituting Eq. (I.3) into Eq. (I.1).

Appendix J

Experimental Data

This appendix contains the experimental data obtained in the present study. The data are categorized in two groups: gas diffusion layer and metal foam.

J.1 Gas Diffusion Layer

$P_c(MPa)$	$\Delta t_1/t_1$	$\Delta t_2/t_2$	R_{tot1}	R_{tot2}	TCR	k_{eff}
0.344	7.904	13.767	2.140	1.901	1.679	1.506
0.454	9.910	17.200	1.756	1.528	1.325	1.575
0.683	13.450	23.182	1.379	1.173	1.001	1.727
0.893	16.060	27.521	1.167	0.976	0.824	1.844
1.232	19.290	32.784	1.008	0.830	0.697	1.956
1.510	21.239	35.885	0.891	0.723	0.602	2.054

Table J.1: Thermal and geometrical data for Toray carbon papers TGP-H-120 and TGP-H-060 at vacuum condition

$P_c(MPa)$	$\Delta t_1/t_1$	$\Delta t_2/t_2$	R_{tot1}	R_{tot2}	TCR	k_{eff}
0.204	5.002	8.754	1.733	1.480	1.234	1.436
0.478	10.318	17.894	1.370	1.150	0.954	1.624
0.767	14.560	25.036	1.115	0.919	0.758	1.805
1.091	18.078	30.824	0.980	0.800	0.662	1.942
1.382	20.405	34.566	0.869	0.698	0.573	2.029
1.497	21.157	35.756	0.823	0.656	0.537	2.077

Table J.2: Thermal and geometrical data for Toray carbon papers TGP-H-120 and TGP-H-060 at atmospheric pressure

$T_{ave}(^{\circ}C)$	R_{tot1}	TCR	k_{eff}
36.6	1.108	0.775	1.934
42.3	1.111	0.775	1.920
45.9	1.119	0.775	1.873
50.3	1.116	0.775	1.888
54.3	1.123	0.774	1.842
60.2	1.128	0.774	1.819
63.6	1.134	0.774	1.785
67.2	1.138	0.774	1.765
71.7	1.146	0.774	1.728

Table J.3: Thermal experimental data for Toray carbon paper TGP-H-120 at different temperatures, $P_c = 0.75MPa$ and atmospheric air pressure

$P_c(MPa)$	$\Delta t_1/t_1$	$P_c(MPa)$	$\Delta t_1/t_1$	$P_c(MPa)$	$\Delta t_1/t_1$
1st cycle	1st cycle	2nd cycle	2nd cycle	3rd cycle	3rd cycle
0	0	0	0.0451	0	0.0579
0.152	0.0351	0.187	0.0963	0.068	0.0890
0.346	0.0851	0.444	0.1353	0.198	0.1230
0.695	0.1351	0.663	0.1529	0.610	0.1790
0.922	0.1622	1.179	0.1953	0.887	0.1983
1.284	0.1919	1.346	0.2059	1.326	0.2186
1.557	0.2189	1.532	0.2211	1.540	0.2264
1.350	0.2094	1.300	0.2102	1.376	0.2240
1.123	0.1993	1.020	0.1976	1.176	0.2163
0.998	0.1924	0.883	0.1918	0.703	0.1991
0.723	0.1744	0.696	0.1807	0.523	0.1867
0.564	0.1597	0.465	0.1618	0.310	0.1633
0.330	0.1350	0.251	0.1286	0.190	0.1404
0.167	0.0990	0.086	0.0898	0.067	0.1005
0	0.0451	0	0.0579	0	0.0653

Table J.4: Stress-strain data for Toray carbon paper TGP-H-120 under a cyclic compressive load, first to third cycle

$P_c(MPa)$	$\Delta t_1/t_1$	$P_c(MPa)$	$\Delta t_1/t_1$
4th cycle	4th cycle	5th cycle	5th cycle
0	0.0653	0	0.0699
0.102	0.1094	0.112	0.1205
0.255	0.1483	0.256	0.1568
0.398	0.1708	0.500	0.1903
0.540	0.1840	0.657	0.2032
0.773	0.2001	0.895	0.2139
0.950	0.2075	1.035	0.2195
1.108	0.2160	1.235	0.2265
1.378	0.2270	1.541	0.2324
1.551	0.2306	1.398	0.2293
1.330	0.2277	1.260	0.2267
1.103	0.2198	1.078	0.2203
0.820	0.2080	0.935	0.2168
0.678	0.2014	0.789	0.2107
0.534	0.1930	0.589	0.1967
0.277	0.1617	0.361	0.1745
0.140	0.1296	0.140	0.1298
0.060	0.0991	0.082	0.1097
0	0.0699	0	0.0701

Table J.5: Stress-strain data for Toray carbon paper TGP-H-120 under a cyclic compressive load, forth and fifth cycles

$P_c(MPa)$	$R_{tot1}(K/W)$	TCR	k_{eff}
0.344	**2.140**	**1.679**	**1.506**
0.454	1.756	1.325	1.575
0.683	1.379	1.001	1.727
0.893	1.167	0.824	1.844
1.232	1.008	0.697	1.956
1.510	0.891	0.602	2.054
1.267	0.971	0.669	1.984
0.944	1.085	0.763	1.900
0.712	1.218	0.874	1.814
0.485	1.475	1.087	1.647
0.249	**1.896**	**1.448**	**1.486**
0.433	1.621	1.210	1.592
0.654	1.328	0.957	1.727
0.990	1.089	0.764	1.896
1.200	1.003	0.696	1.971
1.570	0.870	0.589	2.082
1.310	0.941	0.646	2.017
1.015	1.026	0.714	1.942
0.686	1.207	0.862	1.788
0.470	1.404	1.023	1.655
0.254	**1.767**	**1.332**	**1.509**
0.453	1.490	1.103	1.627
0.700	1.223	0.882	1.801
0.941	1.068	0.743	1.851
1.252	0.947	0.652	2.007
1.527	0.869	0.578	2.005
1.151	0.961	0.669	2.026
0.964	1.018	0.737	2.129
0.656	1.206	0.850	1.705
0.488	1.349	0.984	1.688
0.258	1.652	1.274	1.687

Table J.6: Thermal experimental data of Toray carbon paper TGP-H-120 at vacuum condition under a cyclic compressive load, 1st to 3rd cycle

$P_c(MPa)$	$R_{tot1}(K/W)$	TCR	k_{eff}
0.486	**1.367**	**0.995**	**1.664**
0.642	1.212	0.873	1.802
0.894	1.056	0.750	1.962
1.207	0.933	0.643	2.029
1.525	0.850	0.572	2.091
1.175	0.928	0.637	2.015
0.861	1.050	0.743	1.943
0.689	1.146	0.826	1.882
0.448	1.364	0.987	1.636
0.249	**1.603**	**1.192**	**1.552**
0.442	1.360	0.991	1.670
0.682	1.145	0.820	1.848
0.904	1.007	0.700	1.930
1.219	0.909	0.619	2.009
1.534	0.847	0.573	2.106
1.227	0.898	0.610	2.023
0.912	1.013	0.709	1.943
0.707	1.115	0.790	1.843
0.502	1.285	0.930	1.725
0.269	1.593	1.181	1.546

Table J.7: Thermal experimental data of Toray carbon paper TGP-H-120 at vacuum condition under a cyclic compressive load, 4th and 5th cycles

cycle	$\Delta t_1/t_1$	$R_{tot1}(K/W)$	TCR	k_{eff}	TCR/R_{tot1}	$\varepsilon/\varepsilon_0$
loading, 1	0.1072	1.681	1.260	1.600	0.750	0.966
loading, 2	0.1398	1.532	1.134	1.629	0.740	0.954
loading, 3	0.1688	1.439	1.061	1.656	0.737	0.943
loading, 4	0.1803	1.353	0.984	1.675	0.727	0.938
loading, 5	0.1903	1.309	0.950	1.703	0.726	0.934
unloading, 1	0.1530	1.458	1.073	1.657	0.736	0.949
unloading, 2	0.1647	1.377	1.000	1.672	0.727	0.944
unloading, 3	0.1842	1.339	0.975	1.689	0.728	0.936
unloading, 4	0.1888	1.316	0.952	1.679	0.723	0.934
unloading, 5	0.1880	1.287	0.925	1.686	0.718	0.935

Table J.8: Experimental data of Toray carbon paper TGP-H-120 at different loading-unloading cycle, vacuum condition and $P_c = 0.5MPa$

J.2 Metal Foam

$P_c(MPa)$	$L_1(mm)$	$L_2(mm)$	R_{tot1}	R_{tot2}	TCR	k_{eff}
0.359	17.89	13.93	9.317	8.228	4.400	7.412
0.772	17.89	13.93	7.330	6.255	2.471	7.500
1.121	17.89	13.93	6.560	5.469	1.631	7.393
1.421	17.89	13.93	6.222	5.122	1.252	7.332
1.890	17.89	13.93	5.899	4.782	0.853	7.223

Table J.9: Experimental data of ERG Duocel Al foam with the porosity of 90.3% and pore density of 10 PPI

$P_c(MPa)$	$L_1(mm)$	$L_2(mm)$	R_{tot1}	R_{tot2}	TCR	k_{eff}
0.328	17.91	13.9	10.720	9.523	5.375	6.826
0.621	17.91	13.9	8.553	7.384	3.333	6.990
0.972	17.91	13.9	7.189	5.987	1.817	6.792
1.453	17.91	13.9	6.663	5.470	1.337	6.851
1.948	17.91	13.9	6.116	4.904	0.705	6.744

Table J.10: Experimental data of ERG Duocel Al foam with the porosity of 90.6% and pore density of 20 PPI

$P_c(MPa)$	$L_1(mm)$	$L_2(mm)$	R_{tot1}	R_{tot2}	TCR	k_{eff}
0.387	17.95	13.92	12.793	10.991	4.766	4.555
0.703	17.95	13.92	10.717	8.969	2.932	4.697
0.990	17.95	13.92	10.246	8.427	2.144	4.513
1.530	17.95	13.92	9.616	7.763	1.364	4.431
1.958	17.95	13.92	9.230	7.376	0.973	4.429

Table J.11: Experimental data of ERG Duocel Al foam with the porosity of 94.5% and pore density of 10 PPI

$P_c(MPa)$	$L_1(mm)$	$L_2(mm)$	R_{tot1}	R_{tot2}	TCR	k_{eff}
0.394	17.96	13.93	14.550	12.402	4.976	3.822
0.763	17.96	13.93	12.646	10.522	3.181	3.866
1.214	17.96	13.93	11.618	9.460	2.002	3.805
1.711	17.96	13.93	11.156	8.966	1.395	3.748
2.014	17.96	13.93	11.149	8.920	1.213	3.682

Table J.12: Experimental data of ERG Duocel Al foam with the porosity of 95.3% and pore density of 20 PPI

$P_c(MPa)$	$\lambda_{bot}(\%)$	$\lambda_{top}(\%)$	$\lambda_{ave}(\%)$
0.306	0.08	0.04	0.06
0.509	0.24	0.21	0.23
1.426	0.86	0.82	0.84
2.037	1.05	1.01	1.03
2.852	1.22	1.28	1.25

Table J.13: Ratio of total contact area to cross-sectional area for ERG Duocel Al foam with the porosity of 90.3% and pore density of 10 PPI

$P_c(MPa)$	$\lambda_{bot}(\%)$	$\lambda_{top}(\%)$	$\lambda_{ave}(\%)$
0.469	0.17	0.11	0.14
1.019	0.62	0.58	0.60
1.528	0.92	0.90	0.91
2.445	1.16	1.12	1.14

Table J.14: Ratio of total contact area to cross-sectional area for ERG Duocel Al foam with the porosity of 90.6% and pore density of 20 PPI

$P_c(MPa)$	$\lambda_{bot}(\%)$	$\lambda_{top}(\%)$	$\lambda_{ave}(\%)$
0.306	0.10	0.10	0.10
0.509	0.27	0.23	0.25
1.324	0.67	0.65	0.66
2.037	0.93	0.91	0.92
3.056	1.10	1.18	1.14

Table J.15: Ratio of total contact area to cross-sectional area for ERG Duocel Al foam with the porosity of 94.5% and pore density of 10 PPI

$P_c(MPa)$	$\lambda_{bot}(\%)$	$\lambda_{top}(\%)$	$\lambda_{ave}(\%)$
0.509	0.09	0.07	0.08
1.019	0.49	0.45	0.47
1.528	0.68	0.62	0.65
2.037	0.86	0.80	0.83
3.056	1.07	1.03	1.05

Table J.16: Ratio of total contact area to cross-sectional area for ERG Duocel Al foam with the porosity of 95.3% and pore density of 20 PPI